Feasibility Study of Anisotropic Flow (Elliptic Flow) Using Simulation of Muon Chamber Detector

Dissertation

submitted for the award of the degree of

Master of Philosophy

in

Physics

by

Firdous Ahmad Khan

Under the Supervision of

Dr. M. Farooq Mir

Department of Physics, University of Kashmir,

Hazratbal, Srinagar, 190 006

September, 2012

Contents

List of Figures

List of Tables

Acknowledgments

I would like to take this opportunity to thank all those people who contributed to the completion of this work. First, I would like to gratefully acknowledge and extend my heartfelt gratitude to my Research Supervisor, **Dr.M.Farooq Mir** for introducing me into the field of High Energy Physics and providing me various opportunities to work in other collaborating centres. His constant guidance helped me a lot to finish this research work in time.

My regardful thanks are due to **Prof. Sheikh Javid Ahmad**, Head of Physics Department, University of Kashmir for providing me with necessary infrastructure, help, support and other facilities during my tenure of research. I also extend my thanks to the whole teaching faculty of the department for their generous help whenever needed.

My sincere thanks to **Dr. Subhasis Chattopadhayay**, an eminent experimental particle physicist, VECC, Kolkata for his valuable suggestions and timely help in the completion of my analysis work in appropriate time. My special thanks are also to our CBM Collaborators especially **Dr. Y.P. Viyogi**,and **Dr. Zubyer** from VECC, for their guidance and academic suggestions throughout my research period.

My sincere thanks to my labmates Mr. Shabir Ahmad, Mr. Waseem Raja and Ms. Suraya Bashir for their timely suggestions. My special thanks to other senior scholars and my friends Mr. Raja Nisar, Mr. Waheed Ahmad, Mr.

Gowhar Hussain, Mr. Mubashir Hamid, Mr. Asloob Ahmad, Mr. Naveel Ahmad, Mr. Feroz Ahmad, Mr. Sheikh Ansar, Mr. Nisar Ahmad, Mr. Bilal Ahmad, Mr. Fayaz Ahmad, Mr. Sajad Ahmad,Mr. Zahoor Ahmad and Mr. Bari Maqbool for their help during the completion of my course work. Thanks are also due to research scholars Mr. Mukesh Sharma (JU), Mr. Kalyan Dey (GU), Miss Hushnud and Mr. Tariq (AMU) for their help, support, and good wishes.

I sincerely thank all the members of technical and non-technical/non-teaching staff of the department for their affection and kind co-operation. I have no words to express my gratitude to my parents and brother for bearing with me throughout my M.Phil programme. I shall always remain indebted to them for their unstinted support, be it financially, morally or inspirationally.

Firdous Ahmad Khan

Post Graduate Department of Physics,

University of Kashmir, Srinagar.

Certificate

This is to certify that the dissertation entitled "***Feasibility Study of Anisotropic Flow (Elliptic Flow) Using Simulation of Muon Chamber Detector***" submitted by ***Firdous Ahmad Khan***, in partial fulfillment for the award of the degree of ***Master of Philosophy*** in ***Physics***, is the original research work carried out by him under our supervision and guidance. It is further certified that the dissertation has not been submitted for the award of M. Phil or any other degree to this University or any other University. The scholar has attended the department for statutory period as required under rules.

Dr. M. Farooq Mir

(*Supervisor*) (*Head of the Department*)

Dedicated

to

My Parents

Whose Memories had

Always been an Inspiration

Chapter 1

Introduction

1.1 Introduction

Particle Physics is the branch of physics that studies subatomic particles and their interactions. This statement begs two questions: what are subatomic particles, and how do they interact? Most of what is commonly accepted falls within the realm of the Standard Model [1].

What are subatomic particles? Matter is composed of very small constituents called atoms, thought to be indivisible at the time of first discovery. An atom of a given element (hydrogen, helium, etc...) is the smallest unit that maintains all the chemical properties of the whole. Atoms are known to be made from a dense core of protons and neutrons, surrounded by a cloud of electrons. Particles with physical size smaller than that of an atom 10^{-10}m are considered subatomic particles. Protons, neutrons, and electrons are all considered subatomic. Furthermore, protons and neutrons are believed to be composite particles [2], composed of more elementary constituents. There is no evidence that electrons possess any internal structure.

The Standard Model is a quantum field theory. According to the Standard

Model, matter is composed from twelve basic building blocks called fundamental particles. This model has only three interactions: electromagnetic, weak, strong, each of which has an associated type of charge and mediator boson. The most familiar charge is the electric charge. The charge of the strong nuclear force is called color [3]. All particles possess weak charge, and there is no special name for this quantity. Participants in the strong interaction are called hadrons. Particles that do not participate are called leptons. Particles may possess more than one type of charge. Protons, for example, possess all three. Interactions can be enormously more complicated and the participants can exchange more than one mediator simultaneously.

The Standard Model does not encompass gravity, perhaps the best recognized interaction. Particles in the Standard Model are generally separated in fermions and bosons. The fundamental difference is that fermions must obey the Pauli Exclusion Principle and bosons do not. This distinction has a profound impact on the behavior of these particles.

Fermions are elementary particles of spin-1/2 and consist the building blocks of matter. Fermions are classified, according to how they interact, into quarks (up, down, strange, charm, top, bottom) and leptons (e, μ, τ and the corresponding 3 neutrinos). The interaction among the particles is mediated by bosons (mediators). In order to interact, a particle must possess "charge".

The range of these forces can be estimated by Heisenberg's Uncertainty Principle, which allows for violations of energy conservation of magnitude ΔE over time intervals up to about $2\frac{\Delta E}{\hbar}$. There are also numerous types of mediators of each force; eight gluons, three weak mediators, but only one photon. In Table 1.1, the forces are arranged in order of decreasing strength, the strong nuclear force is the strongest and the weak nuclear force

Mediator	Electric Charge	Force
gluon	0	Strong Nuclear
photon	0	Electromagnetic
$W^{\pm}$	$\pm$	Weak Nuclear (charged)
Z^0	0	Weak Nuclear (neutral)

Table 1.1: *Relationship between Fundamental Forces (Interactions) and their associated mediators. Entries are arranged by relative strength.*

the weakest. The strength of the force is characterized by its coupling α.

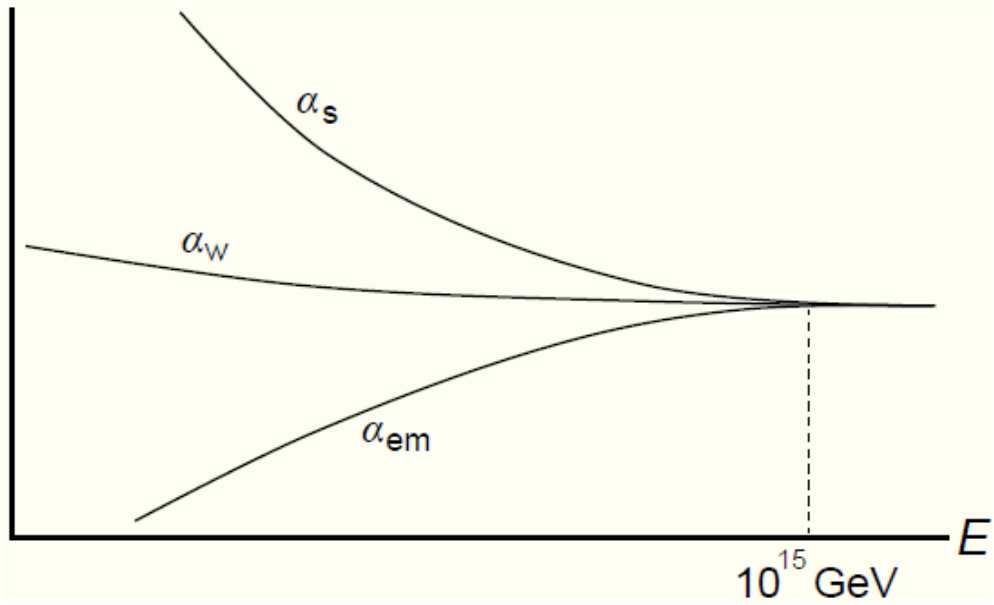

Figure 1.1: *The running of the coupling constants with the energy involved in the interaction.*

This coupling depends on the energy involved in the interaction. At energies which can be observed in daily life the coupling of all forces is very different. The coupling α_s for the strong interactions is of order 1, while for the weak interactions $\alpha_w = 1/29$, for the electro-magnetic interactions $\alpha_{em} = 1/137$ and gravity is much weaker still. However, as the energy goes up the coupling

Flavor	Electric Charge	Quantum Number
u	+2/3	(Isospin) $I_3 = \frac{1}{2}$
d	-1/3	Isospin) $I_3 = \frac{-1}{2}$
s	-1/3	Isospin) $I_3 = \frac{1}{2}$
c	+2/3	Isospin) $I_3 = \frac{1}{2}$
b	-1/3	Isospin) $I_3 = \frac{1}{2}$
t	+2/3	Isospin) $I_3 = \frac{1}{2}$

Table 1.2: *Some basic quark properties. Electric charge is expressed in units of the electron charge.*

constants approach each other and may at some high energy be equal. This might make it possible to describe all forces in a single formalism: a grand unified theory. The energy scale at which this could happen, 10^{15} GeV, is however not accessible in current experiments.

From the Fig. 1.1, one can see that α_s decreases strongly with energy. Also α_w decreases but at a much lower rate. α_{em} is smallest and increases with energy. While α_w is larger the weak force is relatively weaker than the electrodynamic force because of the large mass of its mediators. The decrease with energy of the strong interaction gives very different behaviour of the quarks which are bound by this force compared to other particles. Charged mediators (color, electric or weak) are also potentially subject to additional interactions. The W^+, for example, can emit or absorb photons while being exchanged during a weak interaction.

1.1.1 Quarks and Gluons

Protons and neutrons are common examples of hadrons, but they are composite structures containing more elementary particles, quarks. Quarks have

spin 1/2, and possess both color charge and fractional electric charge. Quarks come in six varieties called flavors: up, down, strange, charm, top, and bottom. Each flavor has an associated unique quantum number which must be conserved in strong reactions (Table 1.2). A quark also possesses one unit of color charge; but unlike the electric charge, color comes in three varieties: red, green or blue. The quarks making the hadron are called valence quarks (3 for baryons, 2 for mesons). Besides these valence quarks hadrons also consist of gluons and a sea of quark-anti-quark pairs. These sea quarks exist only virtually, which means they do not need to have their proper mass. Only half of the momentum of a hadron is carried by its valence quarks. The other half is carried by the gluons. The sea quarks carry little momentum.

The eight types of gluons carry one unit of color and one unit of anticolor (antired, antigreen, or antiblue). Because gluons contain color charge, they are also participants in the strong force, not just mediators. Gluons interact among themselves in addition to interactions with quarks. This behavior is quite unlike the photons involved in an electromagnetic interaction, which do not carry electric charge and consequently do not interact directly with other photons. The study of quarks, gluons, and the color force is known as Quantum Chromodynamics (QCD) [4, 5].

Quarks always manifest themselves in pairs or triplets. Only quark combinations which obey this rule are possible. Every naturally occuring hadron is a color singlet and essentially, this means that the quantum color wave function is color invariant, possessing no net color, or all colors are present in equal proportions. This can be arranged with three quarks each possessing a different color. The resulting singlet wave function is:

$$\psi_{Color} = \frac{1}{\sqrt{6}}(rgb - rbg + gbr - grb + brg - bgr) \tag{1.1}$$

Particles of this type are called baryons. Protons and neutrons fall into this

category.

Other combinations are also possible, but they require anti - quarks. Antiparticles have the same mass as their corresponding particle, but all the quantum numbers are reversed [6]. An antistrange quark $\overline{s}$, for example, has the same mass as a strange quark but a charge of $+1/3$, strangeness of $+1$, and one unit of anticolor. Three antiquarks can combine in the same way three quarks do, producing antibaryons. A single quark and an antiquark can also combine, forming a meson. This exhausts all known combinations.

The strong interaction between partons (quarks and gluons) is described by the QCD Lagrangian:

$$L_{QCD} = \sum_{j=0}^{n_f} \overline{\psi_j} i\gamma^\mu (\partial_\mu - igA_\mu)\psi_j - m_j^0 \overline{\psi_j}\psi_j - \frac{1}{2} TrG_{m\nu}G^{m\nu} \qquad (1.2)$$

The sum is on the quark flavours, n_f. The first term of the Lagrangian corresponds to the kinetic energy of a quark field ψ. The second term expresses the interaction between a quark field ψ and the gluon field A_μ. The third term is the term of quark mass. The last term demonstrates that gluons also interact with themselves and not only with quarks.

The way it is constructed, QCD possesses a lot of symmetries which may be translated in a conservation of a corresponding quantity, as stated by Noether's theorem. These symmetries and their breaking is dictating the structure of the vacuum and the properties of strongly interacting matter.

1.1.2 Confinement, Asymptotic Freedom and QGP

For quarks interacting at large distances, the square of the momentum transfer q^2 between the quarks is small, resulting in a large coupling constant between the quarks. Hence, the coupling between two quarks increases with

distance in such a way that if a quark and anti-quark pair is separated, it is more energetically favorable to create a new quark and anti-quark pair out of the vacuum such that two pairs result. This is the reason that no single quarks exist in nature. This phenomenon is known as confinement.

Alternately, if the distance between a quark and anti-quark pair is decreased (equivalent to large q^2), the coupling weakens logarithmically, leading to a weak coupling of quarks and gluons called *asymptotic freedom*. A consequence of asymptotic freedom is that normal nuclear matter (protons and neutrons) will deconfine into a sea of free quarks and gluons if the energy density or temperature of the system is increased sufficiently. This sea of free quarks and gluons is known as the Quark-Gluon Plasma (QGP). Observing and characterizing this new phase of matter would constitute a testing ground for QCD and possibly shed light on the evolution of the universe since it is believed that the early universe existed in a QGP phase for a short time.

When two nuclei collide at ultra-relativistic energies, they appear in the center-of-mass frame as extremely flat discs due to Lorentz contraction. The nuclei largely pass through each other, and about 75% of the total energy [7] is deposited into the vacuum where the collision occurs. This highly energized vacuum is where partons are first created. The partons interact with themselves, potentially in the QGP phase,until the system expands and cools, and hadronization occurs at the critical temperature. At this point the partons become bound inside hadrons, and inelastic collisions occur between particles. After a brief time ($\sim$ 5fm/c), the matter cools enough that inelastic collisions cease, and the yield of each particle type is fixed. This is known as *chemical freezeout*. After further cooling, the particles cease elastic collisions at a point known as thermal freezeout and stream away from the collision point. The energy density at which a phase transition

occurs between strongly and weakly coupled nuclear matter is not known analytically. However, QCD calculations performed numerically with a lattice gauge theory have been done [8]. Assuming that the state of matter is near thermodynamic equillibrium, lattice QCD can be used to calculate thermodynamical variables such as temperature, pressure and energy density, and help in determining the equation of state. Fig. 1.2 shows how the energy density varies with temperature for current Lattice QCD calculations using two quark flavors, three quark flavors, and two light and one heavy quark flavors. The energy density rises quickly at the critical temperature which is calculated to be around 175 MeV for the results shown. This is indicative of a phase transition. The curve appears to follow the Stefan-Boltzmann law, meaning that the QGP state should behave like an ideal gas.

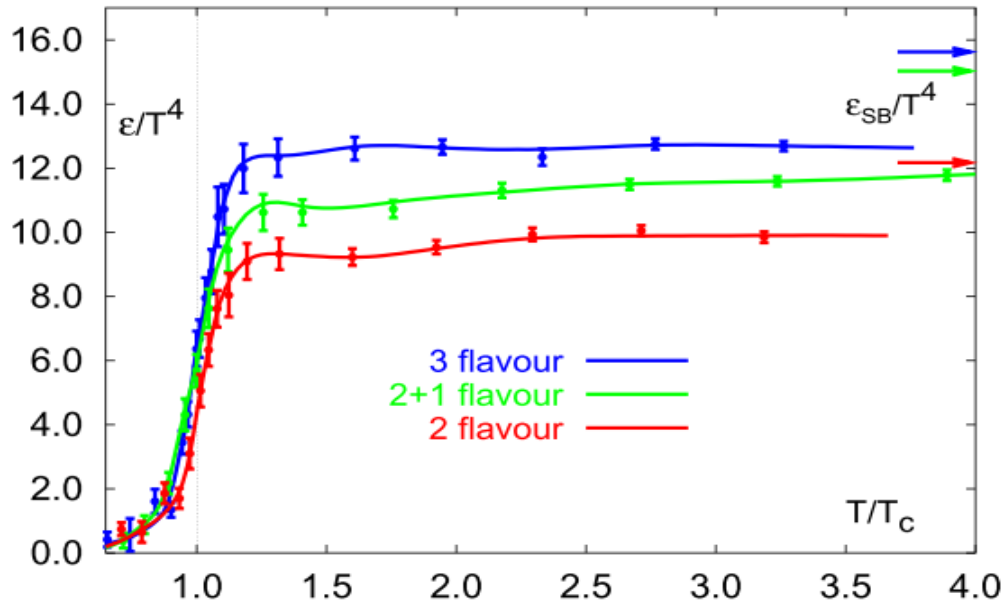

Figure 1.2: *Energy density as a function of temperature for several Lattice QCD calculations with differing quark flavor configurations.*

The phase diagram of nuclear matter as a function of temperature and

baryon chemical potential, which varies with baryon density, shows its various phases. The baryochemical potential, μ_B, is the energy needed in order to add a particle to the system and is related to the net baryon density, ρ_B:

$$\rho_B \simeq 4 \times (\frac{m \times T}{2\pi})^{3/2} \times (e^{\frac{(\mu_B - m)}{T}} - e^{\frac{(-\mu_B - m)}{T}}) \tag{1.3}$$

where m is the particle mass.

At low temperatures and densities, quarks and gluons exist in bound states of hadrons. However, at high temperatures and densities, the hadronic matter undergoes the phase transition into partonic matter in the QGP state. This happens above some critical temperature, T_c, calculated to be about 175 MeV according to lattice QCD.

For high temperatures, and low net baryonic densities, it is generally accepted that the transition to QGP is smooth, without discontinuity, also known as *crossover*. In the region of high net baryon densities, model calculations predict a first order phase transition from hadronic matter to the QGP with a phase coexistence region in between. The existence of a critical point in this region, where the transition changes its nature from continuous to discontinuous, is also predicted.

At the high density, low temperature extreme of the phase diagram, matter is thought to be in a color superconducting state [9]. The quarks form Cooper pairs due to their color charges much like electron pairs in a metallic superconductor. Due to the extreme densities necessary for its formation, this part of the phase space is out of reach of current collider experiments. However, this cold and ultra-dense state of matter may be present in the cores of neutron stars. Figure 1.3 illustrates the space-time evolution of a high energy heavy ion collision.

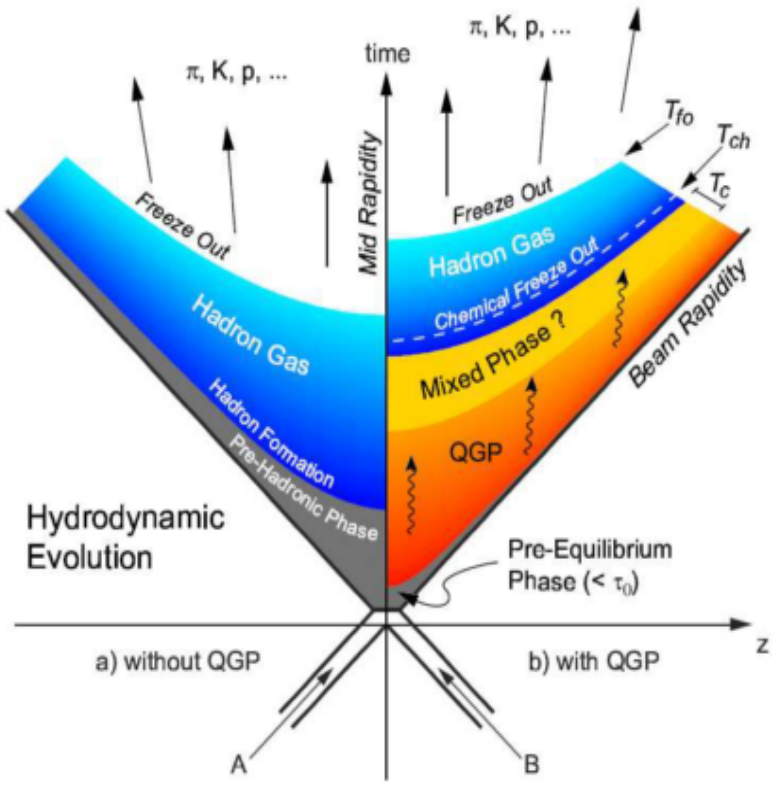

Figure 1.3: *Illustration of the space-time evolution of the fireball [10]. The left-hand side shows the evolution in the case of a purely hadronic scenario (i.e., no QGP formation) while the right-hand side illustrates the expected evolution of the system including QGP formation.*

1.1.3 Chiral Symmetry

The QGP phase of matter may also provide insights into the role of chiral symmetry, providing mass to quarks. Under normal conditions, chiral symmetry is spontaneously broken through the presence of quark-antiquark condensates in the QCD vacuum. A hadron traversing the vacuum gains much of its mass through intersections with these quark condensates. It is believed that in the QGP phase chiral symmetry is restored, meaning that the quarks interacting in the QGP phase are massless.

The long range and short range behavior of the strong force can be decoupled with within the framework of an effective potential [11]. As the temperature increases, the linear potential vanishes, leading to deconfinement

$$V_{color} \approx -\frac{4}{3}\frac{\alpha_s}{r} + kr \tag{1.4}$$

Chiral symmetry is closely related to conservation of helicity, the projection of a particle's spin onto the direction of motion. Particles with positive helicity are said to be right-handed, and negative helicity corresponds to a left-handed particle. Only massless particles have definite helicity, because helicity is not Lorentz invariant. The helicity of a massive particle will be determined by the choice of reference frame.

The chiral symmetry of quarks is said to be explicitly broken by the bare quark masses, $m_u \approx 4MeV/c^2$, $m_d \approx 7MeV/c^2$, $m_s \approx 150MeV/c^2$. If the quark masses were zero, chiral symmetry would be exact. Since m_u and m_d are relatively small, chiral symmetry is still approximate. Mass breaks chiral symmetry [12].

Chiral symmetry can also be dynamically broken [13]. To illustrate this, the nature of the QCD vacuum must be explored. Consider a quark-antiquark pair in a vacuum with a separation r. The momentum and kinetic energy are given by Heisenberg's Uncertainty relation as $\sim \hbar/r$. The potential energy is estimated by eqn. 1.4. Because α_s varies, at very small separation, the kinetic energy term dominates and the total energy is very large. At large separation, the linear term in the potential dominates and the energy is also large. At some point between these extremes, $r_0 \sim$ 1fm, the total energy is minimized, and through careful calculation it can be shown to be negative. The stable QCD vacuum is therefore not empty, but preferentially filled with

$q\overline{q}$ pairs at a relative distance of r_o. This distribution of quark pairs is usually called the quark condensate.

A quark placed in this environment can interact with it. A right-handed quark could annihilate with a right-handed antiquark from the vacuum, leaving a left-handed quark. It appears as if the quark spontaneously changed helicity; chiral symmetry is dynamically broken. This breaking is evidence of the underlying particle interactions which drives up the particle's mass. Quarks thus have a dynamic or constituent mass, $m_{u,d} \approx 360 MeV/c^2$ and $m_s \approx 500 MeV/c^2$.

This argument is only valid at low temperatures. As temperature increases, the kinetic energy of the vacuum quark pairs also increases. There is a critical point where the pair energy is always positive, and it is no longer energetically favorable to fill the vacuum with these pairs. The quark condensate is said to melt, quarks in this hot vacuum no longer generate dynamic mass, and chiral symmetry is restored.

An important consequence of the spontaneous chiral symmetry breaking is the existence of a massless mode, the Goldstone Boson. Chiral symmetry predicts for every particle the existence of a mirror particle with the same mass. Fig. 1.4 shows that most of the observed mass of light quarks is generated by the spontaneous breaking of the chiral symmetry. In the figure, the mass of quarks is shown in the QCD vacuum and the Higgs vacuum. A substantial part of the mass of the light quarks, (u, d, s) is generated by the spontaneous chiral symmetry breaking. The mass of the heavier quarks, (c, b, τ) is practically not affected by the effect of spontaneous chiral symmetry breaking.

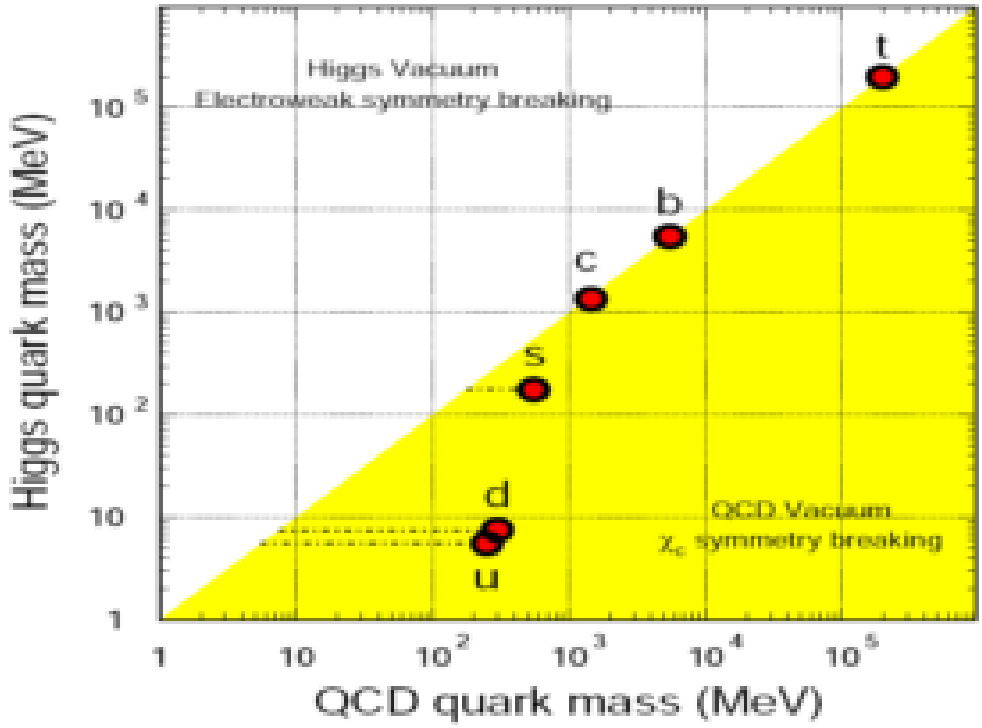

Figure 1.4: *Quark masses in the QCD vacuum and the Higgs vacuum [14]. A large fraction of the light quark masses is due to the chiral symmetry breaking in the QCD vacuum.*

1.2 Possible QGP Probes

The physical properties measured during a heavy ion collision are not expected to be radically altered by a phase transition. The processes which occur in a plasma usually have hadronic analogs which mimic production mechanisms, particle spectra, etc. As a result, most signatures are simply an enhancement of some observable or a suppression of some other variable.

1.2.1 Strangeness Enhancement

It is energetically easier to create strange quarks in QGP than to produce strange hadrons in the case of hadron gas. Thus the ratio of the total number of strange particles to the total number of non-strange particles is increased when QGP is created in the early stage of the collision. Such effects have been observed by experiments at top SPS energies.

The production of strange matter is normally suppressed in favor of particles containing only u and d quarks. The constituent mass of a strange quark ($m_s \approx 500 MeV/c^2$) requires more energy to create than light quarks ($m_{u,d} \approx 360 MeV/c^2$). However,strange particles can be created through associated production, such as $\pi^0 + p \longrightarrow K^+ + \lambda$, or through pair production, where $K^\pm$ or other strange particle-antiparticle pairs are produced together. Neither of these mechanisms requires the formation of a quark gluon plasma. In a quark gluon plasma, there only needs to be enough energy to produce an $s\bar{s}$ pair mainly through a quark-gluon interaction. With the accompanied chiral symmetry restoration, the effective mass drops to the bare mass, $m_s \approx 150 MeV/c^2$, making strange quark pair production even more favorable. Contrast this with an associated production mechanism, $\pi^0 + p \longrightarrow K^+ + \lambda$ for example, in which additional energy is required from energy-momentum conservation. Strange pair creation increases with temperature and baryon density. The higher the temperature, the more energy is available. In a system with high baryon density, many low energy u and d quantum states are already filled, so the formation of low energy strange pairs is favored over high energy u or d pairs. These conditions, high baryon density and available energy, tend to be mutually exclusive in a collider experiment; lower energy colliders have less available energy and more baryon stopping, and higher energy beams have decreasing baryon stopping.

Strangeness enhancement [15] can be estimated quickly by using this suppression factor:

$$\beta_s = \frac{\exp[-(M_s^2 + T^2)^{1/2}/T]}{\exp[-(M_{u,d}^2 + T^2)^{1/2}/T]} \tag{1.5}$$

Using the effective quark masses, the bare quark masses, and a typical temperature of 150 MeV gives an enhancement factor of ~ 2. Multistrange particles should see more enhancement, increasing by an additional factor of ~ 2 for each (anti-) strange quark.

1.2.2 Jet Quenching

Jets are formed when there is a large momentum transfer between a quark in one hadron and a quark in another hadron during a high energy collision. The recoiling quarks, confronted with the confining potential of the parent hadron will eventually make a $q\overline{q}$ pair when conditions are favorable in terms of energy. The recoiling quark is now confined again, and will continue creating $q\overline{q}$ pairs until it lacks the needed energy. These jets are characterized by a shower of particles emitted in the same direction. Jets usually manifest in nearly back-to-back pairs, but can also occur as a three-jet event, when a gluon carries away a substantial fraction of the energy of the initial collision.

In the QGP environment, jets are thought to be quenched simply by the presence of other quarks and gluons. The energetic quark, depending on its production point and direction, often must pass through a dense region of strongly interacting matter. Two effects are possible. One or both quarks could lose most of their available energy through multiple collision. Such quarks will be absorbed, creating no jets that can be detected above the background of soft particles. The quarks could also be deflected by collisions, destroying the back-to-back direction usually associated with a jet event.

1.2.3 J/ψ Suppression

The J/ψ is the lowest energy bound state of a charm-anticharm ($c\bar{c}$) quark pair. In a quark gluon plasma, the linear, long range interaction vanishes. The remaining Coulomb potential, $\sim \frac{1}{r}$, is subject to Debye screening which modifies the potential to a short range Yukawa-like form, $\sim \frac{e^{-r/\lambda_D}}{r}$. λ_D is called the Debye screening length. The screening length is inversely proportional to temperature. Above a certain temperature, the potential becomes so weak that $c\bar{c}$ pairs will no longer be bound.

Since the charm quark is so massive, this system can be approximated in the non-relativistic region. The Hamiltonian is:

$$H = \frac{p^2}{2\mu} - \frac{\alpha_{eff} e^{-r/\lambda_D}}{r} \tag{1.6}$$

The momentum can be estimated from the uncertainty relation. A bound state exists only if the Hamiltonian has a minimum with respect to r. The minimum is determined with the usual method, setting the derivative equal to zero. The result is a relationship between r and the Debye screening length, and therefore temperature. At typical QGP temperatures, this relationship cannot hold, the minimum does not exist, and no bound states are possible [16]. The $c\bar{c}$ pairs dissolve and are more likely to combine with lighter, more numerous quarks prior to chemical freeze-out.

1.2.4 Event-by-Event Fluctuations

It is one of the most important signatures of the QGP [17]. These are sensitive to the dynamics of the colliding system. It is predicted, by various theoretical considerations, that significant event-by-event fluctuations in temperature, transverse momentum, multiplicity and conserved quantities such as net charge may be a signature of the phase transition (QGP formation).

There are two types of fluctuations in a system - statistical and dynamical ones. Dynamical fluctuations are considered to be one of the important tools to study the dynamics of heavy ion collision. Dynamical fluctuations, which can appear both in kinematic characteristics and particle yields, are expected to be modified for systems approaching the phase boundary from hadron gas to QGP. Statistical fluctuations are related to the fact that the number of particles in the system is not infinite.

1.2.5 Elliptic Flow

It is one of the most important signatures of the formation of QGP as it is sensitive to the very early stage of the collision. It has its origin in the initial spatial assymetry of the system, which is then transformed into the momentum anisotropy of the particles.

The relationship between quark gluon plasma and elliptic flow is not one of simple cause-effect. Flow phenomena are observed in purely hadronic collisions [18, 19, 20]. This connection manifests in more subtle ways. The formation of a QGP state should alter the elliptic flow pattern from what would be predicted in a purely hadronic event. There are two main effects: *quark scaling* and *mass ordering*. In the QGP realm, elliptic flow is expected to scale with the number of constituent (anti-) quarks. This is known as quark scaling. Mass ordering is closely related to relativistic hydrodynamics. The nature of elliptic flow in a QGP environment will be examined in greater detail later.

Chapter 2

The CBM Experiment

2.1 Introduction

The Compressed Baryonic Matter Experiment (CBM) is a future fixed target heavy-ion experiment at Facility for Antiproton and Ion Research (FAIR) in Darmstadt, Germany [21, 22, 23]. Highest baryon densities will be created in A+A collisions at 10 - 45A GeV beam energy range. The goal of the experiment is to explore the properties of superdense nuclear matter, looking for in-medium modifications of hadrons, phase transition from dense hadronic matter to quark gluon plasma and for the critical point on the phase diagram of strongly interacting matter which is shown in Fig. 2.1.

Fundamental aspects of Quantum Chromodynamics and Astrophysics will be covered in the program of the CBM experiment: the equation of state of strongly interacting matter at high baryon densities, the restoration of chiral symmetry, the origin of hadron masses, the confinement of quarks in hadrons, the structure of neutron stars, the dynamics of core-collapse of supernovae.

At high temperatures and zero baryon chemical potential there is a region of crossover. The LHC experiments will investigate the phase diagram in

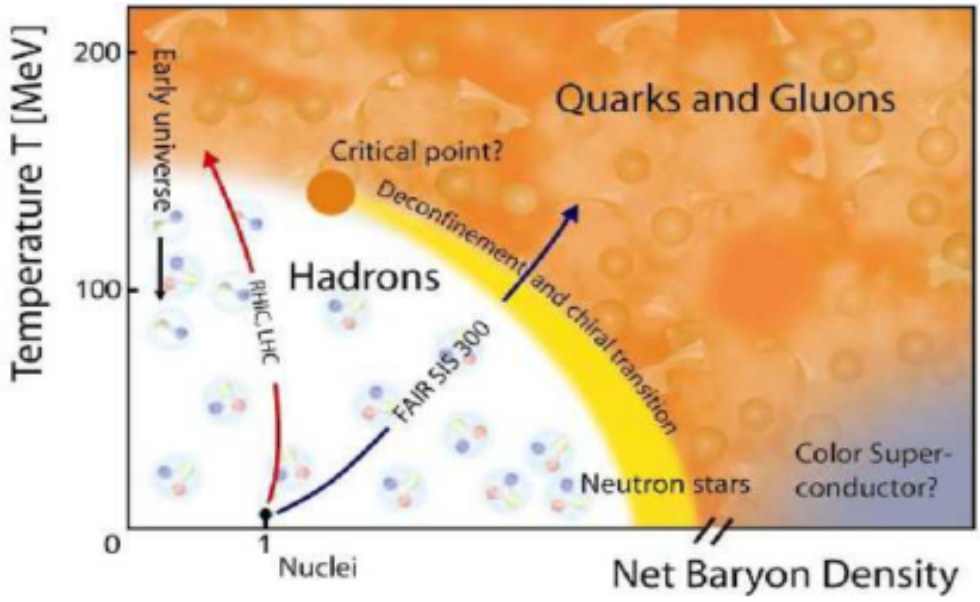

Figure 2.1: *Sketch of the phase diagram of strongly interacting matter plotted as a function of the temperature and the net baryon density [24].*

this region. While the FAIR will explore the region of high baryon chemical potentials and moderate temperatures, where the first order phase order transition occurs. This first order phase transition line ends with the critical point, existence and exact location of which is one of the subjects for the CBM experiment.

CBM will measure rare and penetrating probes such as dilepton pairs from light vector mesons and charmonium, open charm (i.e., particles containing one charm quark and one light quark), multistrange hyperons together with collective hadron flow and fluctuations in heavy-ion collisions.

At large net baryon densities, the mass of open charm particles is expected to be modified in the nuclear medium. In consequence, their production cross section is expected to be modified. This effect should be particularly enhanced close to their kinematical threshold which is located at FAIR ener-

gies. On the other hand, the relative yield of D-mesons and charmonium has been suggested recently as a signature of the deconfinement phase transition. This might appear as a sudden drop in the excitation function of the $J/\psi/D$ ratio at a beam energy corresponding to the onset of QGP formation which is expected to take place in the FAIR energy range.

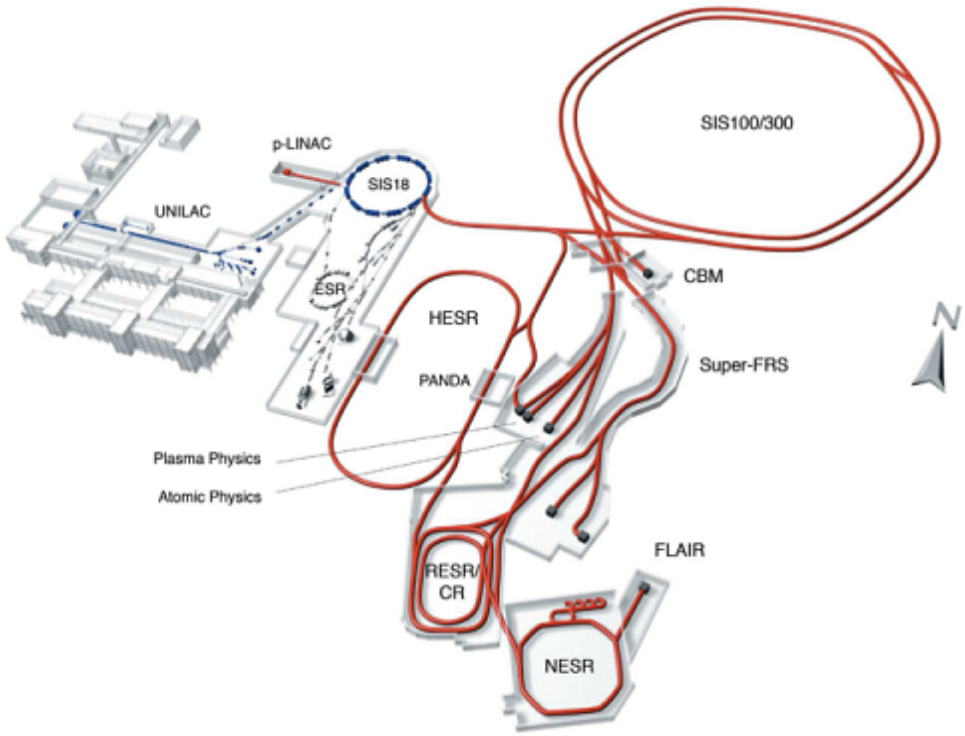

Figure 2.2: *Layout of FAIR [25].*

The CBM experiment will measure open charm particles in heavy ion collisions for the first time in the energy range below 45A GeV. The measurement of open charm particles close to their production threshold calls for high intensity beams. FAIR will offer a large variety of beams, from antiprotons to heavy nuclei, of excellent quality. It will be able to deliver high intensity beams, upto 10^9 particles/second for Au beams and 10^{13} particles/second for protons. FAIR will be composed of two superconducting synchrotrons,

SIS-100 and SIS-300, each with a circumference of 1084 meters. The main motivation for the double synchrotron is the possibility for parallel operation of up to four research programs. This will ensure high beam availability for the experiments, and in particular for CBM, for which this feature is extremely important. The goal of the SIS-100 synchrotron, with a magnetic rigidity of 100 Tm, is to achieve an intensity of up to 5×10^{11} ions per second for uranium beams (U^{28+}) at 2.7 GeV per nucleon. For protons, the goal is to have the intensity of $4{\times}10^{13}$ particles per second for beam energy of 29 GeV. The high-intensity proton beams, which are required for antiproton production, will be supplied by a separate proton linac as injector to the SIS-18 synchrotron. The SIS-300 synchrotron, with a magnetic rigidity of 300 Tm, will provide U^{92+} (fully stripped) beams up to 34 GeV per nucleon with an intensity of 3 $\times 10^{11}$ ions/s. Eqn. 2.1 allows to calculate the energy per nucleon (E/A) which can be reached for each ion with atomic mass A and atomic number Z:

$$E/A = \sqrt{(0.3 \times B \times r \times Z/A)^2 + m^2} - m \tag{2.1}$$

where B $\times r$ is the beam rigidity and m is the mass of a nucleon. For example, a Au^{197} ion (Z/A = 79/197) at SIS-300 ($B \times r = 300\ Tm$) will have a maximum energy of 35 GeV per nucleon while at SIS-100 it could not reach an energy higher than 11 GeV per nucleon.

The existing GSI accelerators UNILAC and SIS-18 will be upgraded in order to serve as an injector. The high-intensity beams will be extracted over periods of 10-100 seconds in quasi-continuous mode, as the complex detector systems used for nucleus-nucleus collisions experiments can accept up to $10^8 - 10^9$ particles per second. Slow extraction from the SIS-100 is an option for extending the flexibility of parallel operation for experiments.

2.2 The CBM Detection System

The major experimental challenge for CBM is posed by the extremely high interaction rates of up to 10^7 events/second. These conditions require unprecedented detector performances concerning speed and radiation hardness. On the other hand, the high particle track multiplicity environment in nucleus-nucleus collisions at FAIR energies (about 1000 charged particles in central Au+Au collisions at 25A GeV) requires high granular detectors. The de-

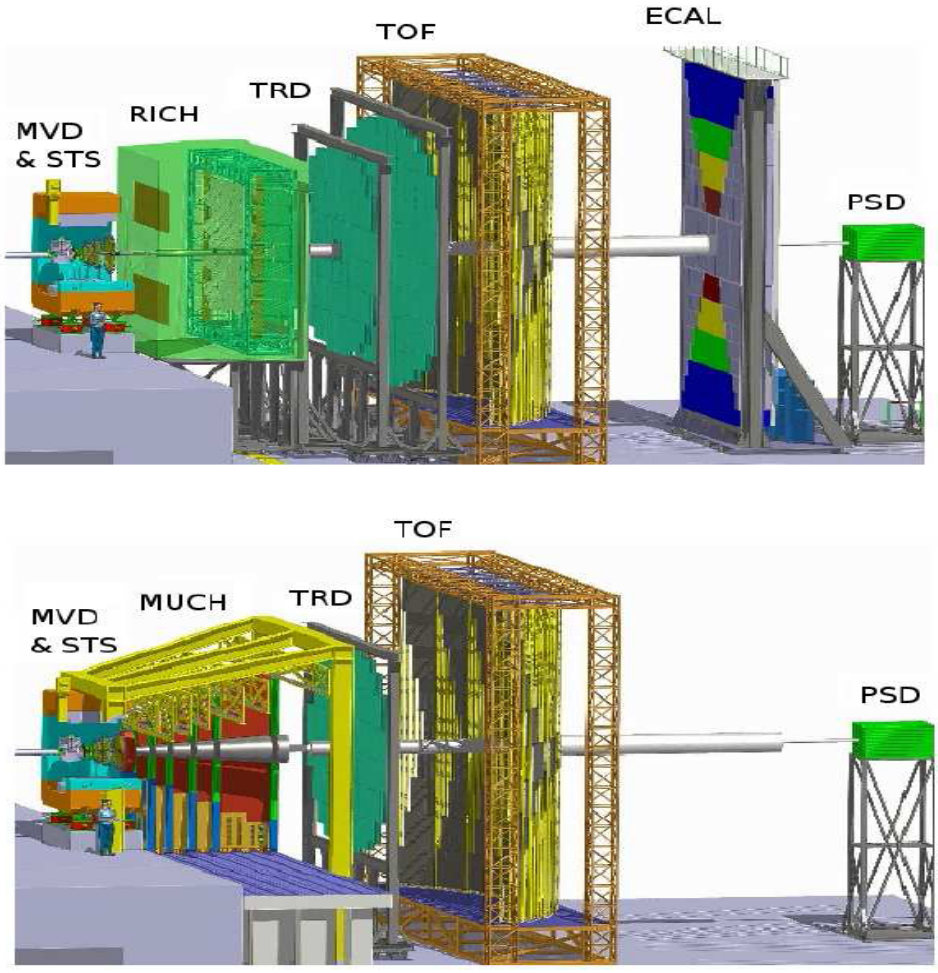

Figure 2.3: *Schematic view of the CBM experiment. The electron setup is shown in the top panel and the muon setup in the bottom panel.*

tector signals are processed by a high-speed data acquisition and an online event selection system. The detectors and their readout electronics should be fast, radiation hard and should cover a large acceptance with full azimuthal coverage. The track reconstruction algorithms should provide high precision and fast online tracking, with high efficiency and excellent momentum resolution. A very good particle identification capability both for hadrons and leptons is required. All these requirements should be fulfilled in a wide range of energies (10-45A GeV) and for various system sizes (p+p, p+A, A+A) in order to achieve the physics goals of CBM.

A schematic view of the proposed detector concept is shown in Fig. 2.3. In the present design, CBM has two detector configurations: one is specialised for electron identification (electron configuration) and the second is specialised for muon identification (muon configuration). Both setups are not compatible as the muon measurements require efficient particle absorbers which would not allow for electron measurements.

The two detector configurations have in common a high resolution Micro Vertex Detector (MVD), a Silicon Tracking System (STS), a Transition Radiation Detector (TRD), a Time-of-Flight (ToF) system made of Resistive Plate Chambers (RPC) and a Projectile Spectator Detector (PSD). In the electron configuration, a Ring Imaging CHerenkov detector (RICH), and an Electromagnetic Calorimeter (ECAL) are foreseen for electron identification, while for the muon configuration they are replaced by a Muon Chamber (MUCH).

2.2.1 The Silicon Tracking System

The Silicon Tracking System (STS) [26, 27, 28] is the second detector after the target (first station is placed at 30 cm after the target). It is the central

component of the CBM experiment and serves for track and momentum measurement of charged particles produced in the collision. A particular challenge for the STS is to achieve high track reconstruction efficiency in a high track and hit density and the non-homogeneous magnetic field.

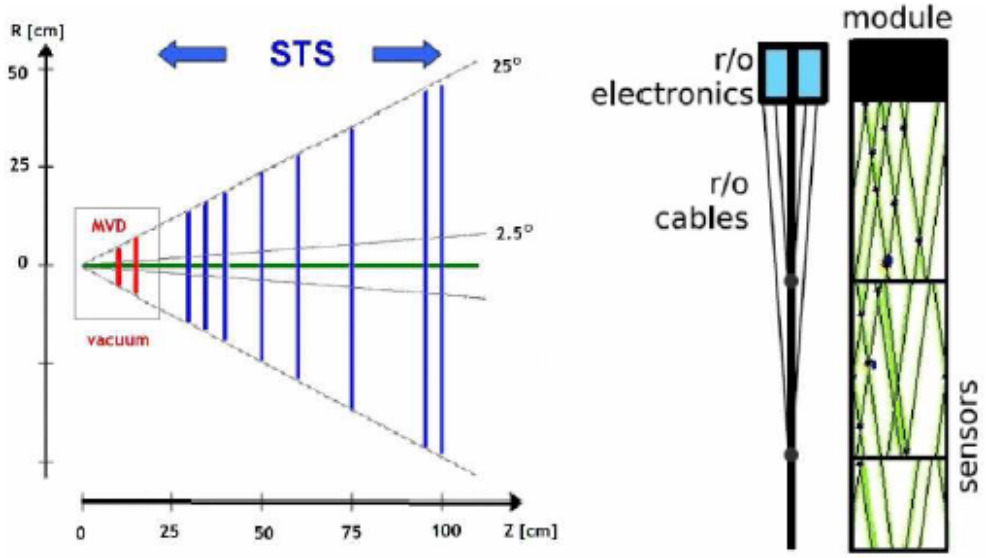

Figure 2.4: *Left: Layout of the STS and MVD stations. The locations of the stations and their polar angle coverage are indicated. Right: One STS module with the read-out electronics: side view and front view.*

The STS comprises 8 detector stations placed at 30, 35, 40, 50, 60, 75, 95, 100 cm distance from the target, and is fully based on low-mass Silicon micro-strip detectors with a pitch of $60\mu m$ as shown in Fig. 2.4. The stations are placed inside a magnetic dipole field which provides the bending power required for momentum determination with an accuracy of $\Delta p/\mathrm{p} = 1\%$. The required time resolution of the STS is of the order of 10 ns, corresponding to a collision rate of 10 MHz. Each station is made of double-sided micro-strip sensors. The strips on the front side are tilted by 7.5° and on the back side by $-7.5°$ creating a stereo angle of 15°. The read-out electronics is placed at

the perimeter of the STS.

In central Au+Au collision at 25A GeV about 600-700 tracks are accepted in the STS. A dedicated tracking algorithm, named Cellular Automaton (CA) [29], was developed for this. The CA method creates short track segments in neighbouring detector planes and links them into tracks. Being essentially local and parallel the CA algorithm avoids exhaustive combinatorial searches. It internally uses a Kalman Filter for the track parameter propagation [30]. Note, that this algorithm requires four consecutive hits in order that a track can be reconstructed. Here, the STS setup with double-sided micro strip detectors only was studied. Eight stations of the STS were considered. No charge sharing between the strips but simple Gaussian smearing of the hit position in the STS detector was implemented. The cbmroot trunc version (revision number 6025) is used as a simulation tool.

After finding a track, its parameters are determined using the Kalman Filter. The STS has to fulfill the following requirements: material budget below 0.3% radiation length per layer to reduce multiple scattering, hit resolution of about $10\mu m$ to achieve a vertex resolution of about 50 microm along the beam axis, radiation hardness up to a dose of 50 MRad corresponding to the dose accumulated in ten years of running and read-out times of less than 25ns to accommodate reaction rates of 10MHz. One possible technology is Silicon microstrip detectors technology. The current layout foresees a pitch of 50 μm and three different strip lengths of 20, 40 and 60mm. The strips are arranged such that the occupancy is below 2% for a central Au+Au collision at 25A GeV. The detectors will be double sided with a stereo angle of 15% between the strips which has to be optimized by simulations.

2.2.2 Micro Vertex Detector

The major task of the CBM Micro Vertex Detector (MVD) is the reconstruction of D-mesons in heavy-ion collisions at FAIR energies. The strategy of the D-meson reconstruction in CBM is based on the separation of the displaced decay vertex from the primary collision vertex as illustrated in Fig. 2.5, which shows a D^0 particle flying out of the primary collision point (PV) and decaying into a pion and a kaon pair. The particles produced in the collision (primary particles) are drawn with the dashed black lines; the products of the D^0 decay (secondary particles) are drawn in full red lines. The tracks reach the micro-vertex detector which has to reconstruct the vertices with sufficient precision to distinguish the primary vertex from the secondary one. This task is very challenging as the decay length of charmed mesons is very small. An excellent vertex resolution is therefore required.

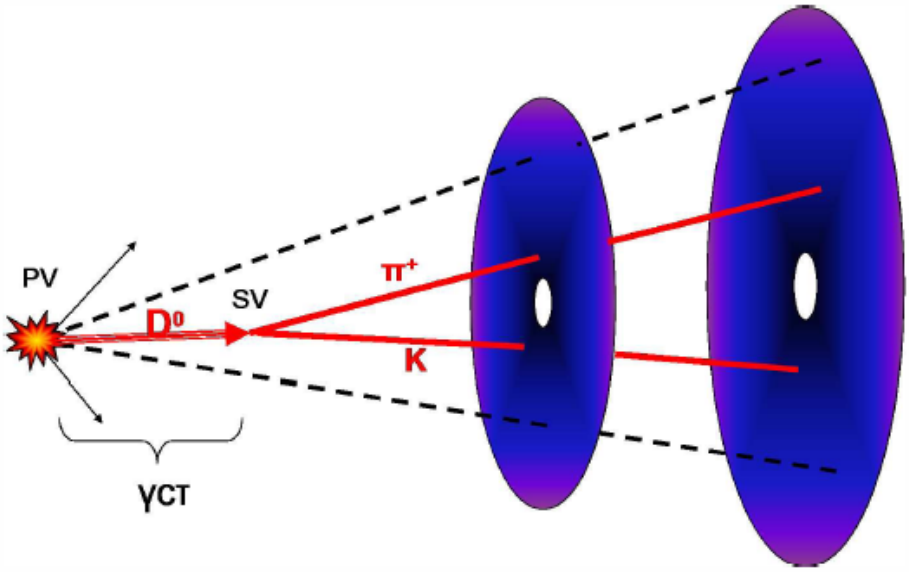

Figure 2.5: *Detection strategy for open charm mesons in CBM*

Among the D-mesons, the D^0 particle is considered as the most difficult

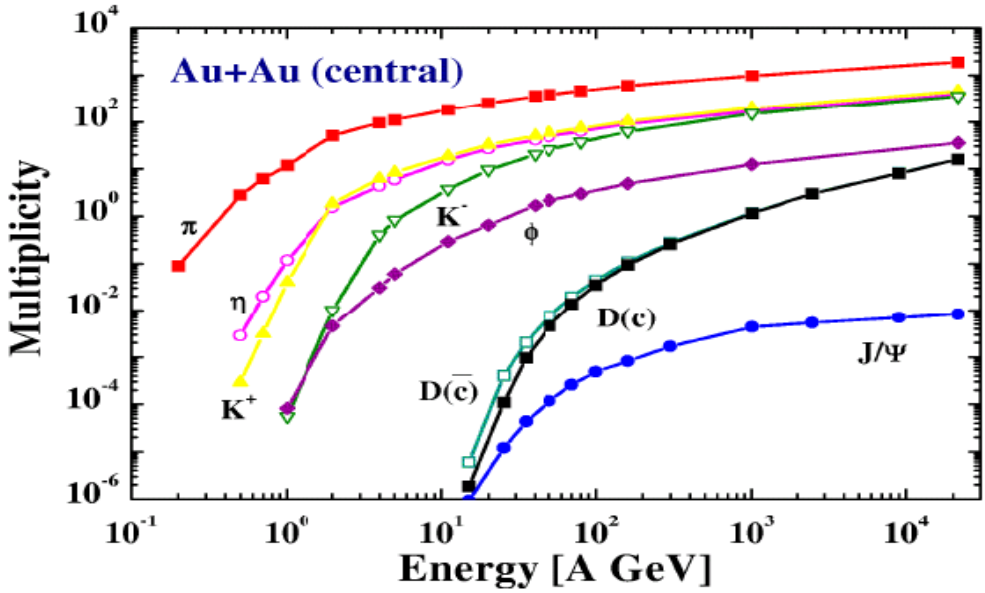

Figure 2.6: *HSD transport model predictions [31] for the multiplicity of mesons produced in central Au+Au collisions as function of the incident beam energy.*

to detect because of its very short lifetime. The task is further complicated by the fact that the measurements will be performed at beam energies close to the kinematical production threshold. According to the HSD model predictions shown in Fig. 2.6, the D-mesons are presumably produced with very low multiplicities (below 10^{-3}) at FAIR energies, while pions and kaons will be abundantly produced (multiplicity of charged hadron is of the order of 10^2). Consequently, D-mesons have to be separated from an important combinatorial background. Therefore, open charm measurements in nucleus-nucleus collisions at FAIR energies are very challenging, in particular in the case of heavy systems such as Au+Au.

The MVD must be located as close as possible to the interaction point and will be therefore exposed to high particle rates, upto 10^{10} pps. Silicon

pixel detectors are foreseen in order to keep the occupancy at an acceptable level (below 1%). The MVD stations should be highly granular (pixel size of $\sim 20 \times 20 \mu m^2$) and very thin (a thickness of few 100μm). Both requirements can be fulfilled by the technology of Monolithic Active Pixel Sensors (MAPS) [32]. The MVD consists of two detector planes, based on this MAPS technology, which are mounted in vacuum. With a small-size prototype a position resolution of $3\mu m$ was achieved. Current task of R&D is an improvement in read-out time and radiation hardness because the MVD detector layers will be also exposed to high radiation doses: up to $10^{15} n_{eq}/cm^2$ per run year (1 CBM run year = $5 \times 10^5 s \approx 2$ months), for a beam intensity of 10^9 ions per second and assuming a 1% interaction target [33].

2.2.3 Transition Radiation Detector

The Transition Radiation Detector (TRD) [34] serves for tracking of charged particles and for the identification of high energy electrons and positrons ($\gamma > 2000$) which are used to reconstruct J/ψ mesons. For discriminating electrons from pions in the momentum region of a few GeV/c, a TRD exploits, one hand, their different energy loss through ionisation. On the other hand, electrons produce additional transition radiation which is then used by the TRD for their identification. Transition radiation is produced when a relativistic particle traverses an inhomogeneous medium, in particular the boundary between materials with different dielectric constants. Currently, the TRD is envisaged to be a system composed of three stations with three to four layers each, located at distances of 5 m, 7.25 m, and 9.5 m from the target. The total active area covered is about 600 m^2. Each layer consists of a radiator where the transition radiation is produced by electrons, and of a gaseous detector in which the deposited energy of charged particles and the

transition radiation can be measured.

According to simulations which are based on the experience obtained with the development of the TRD for ALICE and of the TRT for ATLAS, pion suppression factors of up to 200 (for momenta above 2GeV/c) at an electron efficiency of better than 90% can be achieved [35].

The major technical challenge is to develop highly granular and fast gaseous detectors which can stand the high rate environment of CBM in particular for the inner part of the detector planes covering forward emission angles. For example, at small forward angles and at a distance of $4m$ from the target, we expect particle rates of more than 100 kHz/cm^2 for 10 MHz minimum bias Au+Au collisions at 25 AGeV. In a central collision, particle densities of about $0.05/cm^2$ are reached. In order to keep the occupancy below 5% the size of the smallest types cell should be about 1 cm^2.

There are two approaches for the track reconstruction in the TRD: a standalone method which creates tracklets in different stations and connects them. Second, a 3D track following algorithm based on seeds from the STS. Tracks, reconstructed in the STS, are extrapolated to the first TRD station. Hits, which satisfy a searching criterium, are attached to the track. Afterwards track parameters are updated using the Kalman Filter and the track is propagated to the next station. Both methods show comparable efficiency, but the second is faster, because it does not need a combinatorial search. The efficiency drops down at lower momentum due to multiple scattering in the TRD material. The advantage of the second method is that one does not need to merge STS and TRD tracks, this is directly included in the tracking itself. In the standalone method tracks need to be merged.

After the track is reconstructed in STS and TRD (for the standalone algorithm track segments also have to be merged) it is refitted using the Kalman

Filter. Then track parameters at the last TRD station are propagated to the ToF wall and the closest ToF hit is attached to the track. Only one ToF hit can be attached to one global track. After merging with ToF is done, the track is refitted and the length of the trajectory is calculated starting from the primary vertex to the ToF hit.

The segmented pad like setup of the CBM ToF wall was implemented in the current simulation (with pad size $2\times2cm^2$). The wall has eight gaps and produces a hit with realistic time response out of eight Monte Carlo points created by a charged track during the simulation. For tracks with $p > 1GeV/c$, an efficiency of 86.4% is achieved.

2.2.4 The Superconducting Dipole Magnet

Inside the dipole magnet, the charged particle trajectories are bended and their charge and momenta can be determined. It must host the target (typically a gold foil of 250 μm thickness corresponding to 1% nuclear interaction length), the MVD, and the STS. Therefore, its gap has to be large enough to permit the installation and maintenance of the STS and the MVD (not less than $1.3 \times 1.3m^2$). For a good momentum resolution, a field of about 1.0 Tm is required in the region of the target. The angular acceptance of the magnet should cover 50° in vertical direction and 60° in horizontal direction. The conceptual design of the magnet is shown in Fig. 2.7. The magnet is supplied with a yoke of magnetically soft steel with low carbon content. The upper and bottom beams form the poles of the magnet. Magnetic shields, reducing the field in the area of the RICH (to be discussed), are installed on the yoke. The superconducting coils have the "Cossack saddle" form, which allows to create a magnet with a minimal size along the beam.

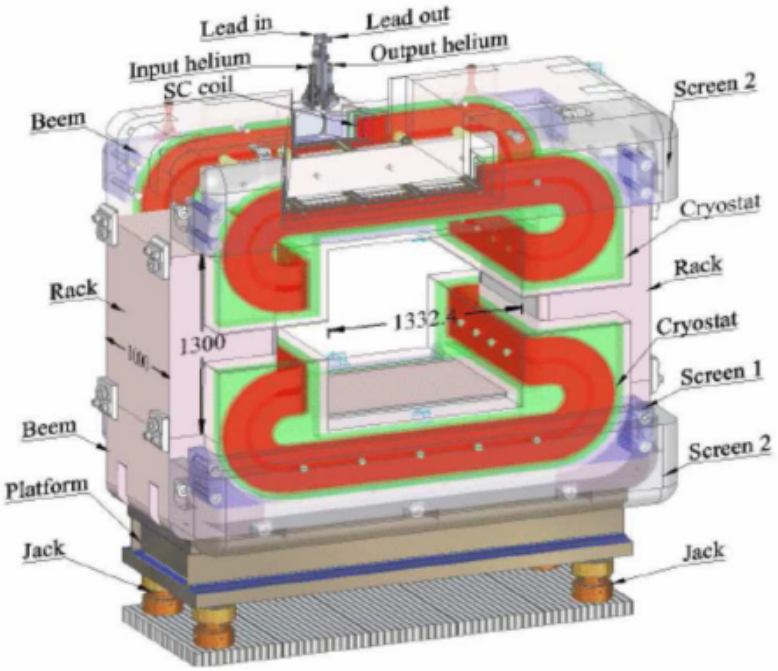

Figure 2.7: *The magnet and the coils (red)*

2.2.5 RING Imaging CHerenkov Detector

In CBM, the RING Imaging CHerenkov detector (RICH) is designed to provide electron identification with momenta up to 10 - 12 GeV/c and for π identification for higher momentum in order to improve the K/π separation which quickly deteriorates for $p > 4GeV/c$ if only ToF information is used. The RICH detector has to provide a pion suppression of $10^2 - 10^3$. The actual layout of the RICH detector consists of a radiator, a mirror and a photon detector. The glass window of the photomultipliers is covered with wave-length shifter (WLS) films in order to increase the absorption of Cherenkov photons [36]. When a charged particle traverses the radiator with a velocity greater than the speed of light in that medium, Cherenkov radiation, in the form of a cone, is produced. In the RICH detector, this light cone is reflected by the

mirror to the position sensitive photon detector, which allows to reconstruct the produced rings. The light is emitted under a constant Cherenkov angle δ with the particle trajectory, given by:

$$\cos\delta = \frac{1}{\beta n} \tag{2.2}$$

where n is the refractive index of the medium and β is the velocity of the particle in the medium.

A crucial task, here, is to match the rings to the charged particle tracks. If the track position at the mirror can be determined with an accuracy of 200 μm, and assuming a momentum resolution of 1%, the mismatch of pions to electron rings is less than 10^{-3} per event. This number will be considerably improved when taking into account particle identification by ToF measurement and by the TRD.

In the current CBM detector layout, the RICH would be placed behind the magnet (roughly $1.5m$ downstream the target) and infront of the first TRD. It consists of a $\sim 3m$ long gas radiator, two arrays of spherical hexagonal mirrors, two photodetector planes and the corresponding support structure. High detection efficiency of electrons is required which calls for 10-15 hits per electron ring at minimum. As global tracking has to connect tracks in the STS and TRD, the RICH detector should not exceed 3 m and a material budget of $3-4\%$ radiation length in order to reduce multiple scattering. A large acceptance of 25° in polar laboratory angles has to be covered to identify the vector mesons in a wide range of rapidity and transverse momentum.

2.2.6 Resistive Plate Chamber

In CBM experiment, an array of Resistive Plate Chambers (RPCs) will be used for hadron identification via ToF measurements. The ToF wall is located about 10m downstream of the target and covers an active area of about $120m^2$. The required time resolution is about 80ps. For 10 MHz minimum bias Au+Au collisions at 25 AGeV the innermost part of the detector has to work at rates up to 20 kHz/cm^2. At small deflection angles the pad size is about $5cm^2$ corresponding to an occupancy of below 5% for central Au+Au collisions at 25 AGeV. With a small-size prototype a time resolution of about $90ps$ has been achieved at a rate of $25kHz/cm^2$. Future R & D concentrates on the rate capability, low resistivity material, long term stability and realization of large arrays with overall excellent timing performance [37].

2.2.7 The Time of Flight Detector

The determination of the particle mass is done by measuring its momentum, p, and its time of flight (ToF):

$$m = \frac{p}{\gamma\beta c} = \frac{p\sqrt{1-\beta^2}}{\beta c} \tag{2.3}$$

where $\beta = \frac{L}{c\Delta t}$. L is the flight path length of the particle and Δt is the time difference between the start and stop signal of the ToF detector. A micro-strip (or diamond pixel) detector provides the start signal for the ToF measurement and can directly count beam particles at intensities of up to 10^9 ions/s. The ToF wall consists of about 60,000 independent cells providing a time resolution of about $80ps$. It will be composed of a large area ($150m^2$) of RPCs. The distance between the start detector and the ToF wall, of about $10m$, results in a time difference of 400 ps for pions and kaons of 3 GeV/c momentum. The RPCs must withstand the rates of up to 20 kHz/cm^2 in

order to handle the high beam intensity. By the ToF method, a separation of kaons and pions can be achieved up to laboratory momenta of about 3.5 GeV/c, while protons can be identified up to 7 GeV/c.

2.2.8 Electromagnetic CALorimeter

The Electromagnetic Calorimeter (ECAL) will be used to measure direct photons, neutral mesons decaying into photons, electrons and muons. Simulations and R & D have been started based on shashlik type detector modules as used in HERA-B, PHENIX and LHCb. The calorimeter will be composed of modules which consist of about 140 layers of lead and scintillator material, with cell sizes of 3 $\times 3cm^2$, 6 $\times 6cm^2$, and 12 $\times 12cm^2$. Particular emphasis is put on a good energy resolution and a high pion suppression factor.

2.2.9 MUon CHamber

The MUon CHamber detector (MUCH) of the CBM Experiment is used for the detection of muons. It will be discussed in detail in the next chapter.

2.2.10 Projectile Spectator Detector

The Projectile Spectator Detector (PSD) will measure the forward energy near the beam axis carried by projectile spectator nucleons and fragments. This measurement will allow to determine the number of nucleons participating in the nucleus-nucleus collision, and thus the collision centrality, on an event-by-event base. The currently planned setup of the PSD consists of 12×9 modules, each with 60 lead scintillator layers with a surface of $10 \times 10cm^2$. The scintillation light is read out via wavelength shifting (WLS) fibers by Multi-Avalanche Photo-Diodes (MAPD) with an active area

of $3 \times 3mm^2$ and a pixel density of $10^4/mm^2$.

2.2.11 Hadron Identification

In the CBM experiment hadrons will be identified using a ToF wall, which is placed $10m$ after the target. A simultaneous measurements of track the length l (assuming that the particle comes from the main vertex) and the time-of-flight t provides the velocity of a particle $\beta = \frac{l}{ct}$. Knowing the momentum p from the track fit in the STS one can calculate the squared mass as

$$m^2 = p^2(1/\beta^2 - 1) \tag{2.4}$$

Chapter 3

The MUCH Detector

3.1 Introduction

As an alternative approach to the dielectron measurement in the CBM experiment the possibility of detecting vector mesons, like $\rho, \omega, \phi, J/\psi$, via their decay into dimuons is currently under investigation. It is aimed for muon identification down to momenta of 1.5 GeV/c. Here hadrons would be suppressed with several absorber layers located behind the STS. A possible setup for the MUCH is presented in Fig. 3.1. Like in the "electron setup" (see Fig. 2.3), the momentum of these tracks is determined with the STS. Subsequently, all charged particles are tracked through the absorber in order to match the muons, which pass the absorber, to the STS tracks. This can be achieved by highly granulated and fast detectors which are located in each gap between the absorber layers. The current design of the muon detection system foresees 18 detector stations and 6 segmented iron absorbers. In this case, the total material budget would correspond to 13.5 times the nuclear interaction length. Promising candidates for the fast and highly granulated detectors, located in the five gaps between the absorber layers, are gaseous

detectors based on GEM technology [38], straw tubes, and one of the TRD stations. The total area of the muon chambers would cover an area of about $70m^2$.

Currently, it is not yet decided if the "electron" or the alternative "muon setup" will be built. The solution offering the most comprehensive research program would be to build both setups which can be used alternately. In that case, the RICH has to be temporary removed and the last 3 detectors of the MUCH can correspond to tracking detectors which will anyway be in place in order to cover the gap between STS and ToF. The TRD, for example, could be used for this purpose, too. Of course, the ECAL cannot be used in conjunction with the muon detection system.

3.1.1 The CBM muon identification system

Simulations for CBM and development and tests of the reconstruction algorithms are done within the software framework FAIRROOT [39, 40]. This C++ based framework uses the Virtual Monte Carlo concept, enabling to switch between different transport engines like GEANT3 or GEANT4, ROOT I/O, the ROOT geometry package for navigation and the ROOT task concept for both reconstruction and analysis. The simulations include detailed detector geometries with passive materials, supports and front-end electronics, advanced detector response models comprising charge propagation and discretisation on the read-out planes, and full reconstruction of space points, tracks and vertices [41, 42, 43].

The CBM muon detector will be used for the detection of vector mesons via their decay into $\mu^+\mu^-$ pairs. For the measurement of muons from low-mass vector mesons (ρ, ω, ϕ), the total iron absorber thickness is 125 cm (7.5 λ_I), whereas for muons from charmonia, $1m$ of iron is added (total thickness

of 13.4 λ_I).

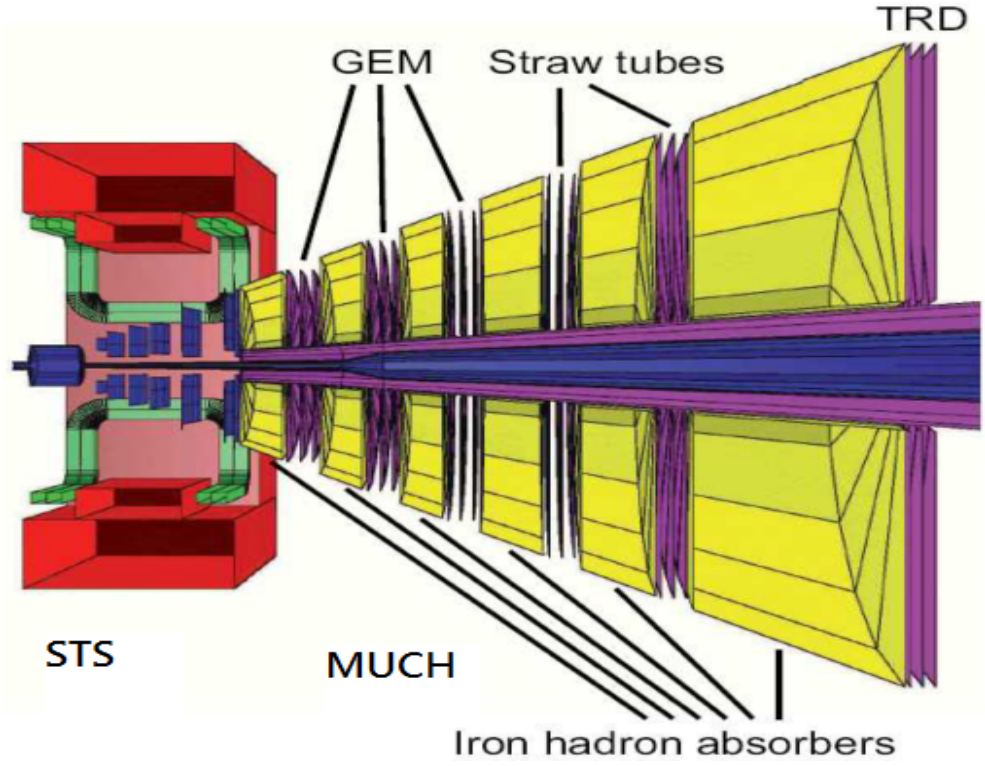

Figure 3.1: *A schematic view of the STS and MUCH.*

3.1.2 Track and vertex reconstruction

The main track reconstruction blocks are track propagation, finder, fitter and selection. The standard Kalman filter technique [44] is being used for the estimation of track parameters.

The track propagation algorithm calculates the average trajectory and corresponding errors. During the propagation three physics processes are taken into account:b (1) energy loss; (2) multiple Coulomb scattering; (3) magnetic field. The main components of the track propagator are the track extrapolator, the material effects calculator and the geometry navigator. The

track propagator manages these three blocks and performs the transport of the track.

The extrapolation part relates to the geometrical extrapolation, governed by the equations of motion. In case of the absence of a magnetic field, a straight line model is used for the average trajectory and transport matrix calculation. In a magnetic field the equation of motion for a charged particle is solved with the 4^{th} order Runge-Kutta method with a parallel integration of the derivatives.

Material effects are taken into account by regularly updating the momentum due to energy loss and by adding process noise due to multiple scattering and energy loss to the track covariance matrix. Energy loss of particles traversing detector material occurs due to electromagnetic effects-ionization (Bethe-Bloch formula), bremsstrahlung (Bethe-Heitler formula) and direct pair production. Multiple scattering is a random process, therefore it influences only the covariant matrix. A Gaussian approximation (Highland formula) [45] has been used to estimate the projected scattering angle.

The geometry navigator searches for intersection points with the detector elements in a certain segment along a straight line. The implementation of the navigation is based on the ROOT geometry package.

Assume that we want to propagate a track from Z_0 to Z (see Fig. 3.2). First, the segment $[Z_0, Z]$ is divided into several steps. In each of these steps the geometry navigator searches for intersections with the material along a straight line (marked with dots). The precise extrapolation is then done in a second step between the intersection points inside each step. Material effects are added at each intersection point. The straight line parameters as used in the navigation are updated after each step.

The track finding algorithm is based on track following and the Kalman

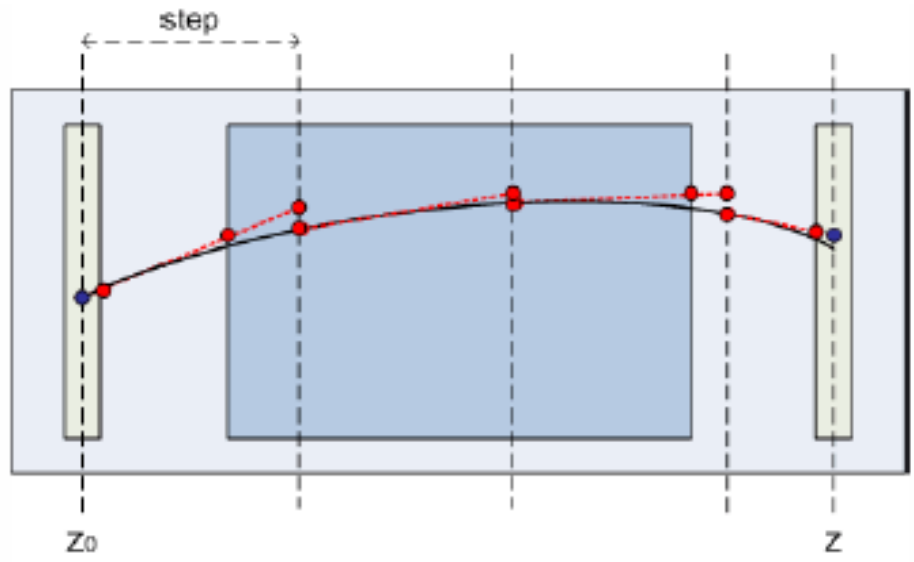

Figure 3.2: *Sketch of the track propagation algorithm.*

filter. The algorithm tracks the particles and includes new hits one by one. It uses branching, where a branch is created for each hit that passed a test to be assigned to the track-segment. The algorithm accounts for missing hits in order to deal with detector inefficiencies. A flowchart of the algorithm is shown in Fig. 3.3. The algorithm consists of two main parts, i.e., track following and track selection. A sketch of the track following and creation of branches is also shown in Fig. 3.3 for the example of two input tracks. The algorithm starts by extrapolating input tracks taken from the STS to the first station. The searching region is calculated as 3σ around the predicted position assuming a Gaussian distribution of errors. Hits which are in this searching region are assigned to the track. For each of the hits and a possibly missing hit a separate branch is created. The parameters of each track-branch are updated with the Kalman filter. This procedure is repeated until the last station is reached. In the example shown, there is one hit in the searching region of track 1 on the 1^{st} station. As a result two branches are created -

the first one for the hit, the second one for a possibly missing hit. Finally, for track 1 five branches have been created, two of them will be used for the further track selection; for the track 2 two branches have been created, one of them is good. Currently one missing hit is allowed for at maximum, branches with more are rejected from the sample.

The aim of the track selection algorithm is to remove clone and ghost tracks and to keep good ones. Clone tracks are tracks that consist of a similar set of hits, ghost tracks are tracks that consist of some random set of hits. The algorithm works in two stages. First, tracks are sorted by their quality, which is defined by the track length and χ^2 (Fig. 3.4). Then a procedure which checks all shared hits of the tracks is executed. It loops over all tracks starting with the highest quality track and collects used hits, for each new track the number of shared hits is checked. If there are too many shared hits the track is rejected. Track reconstruction for high multiplicity

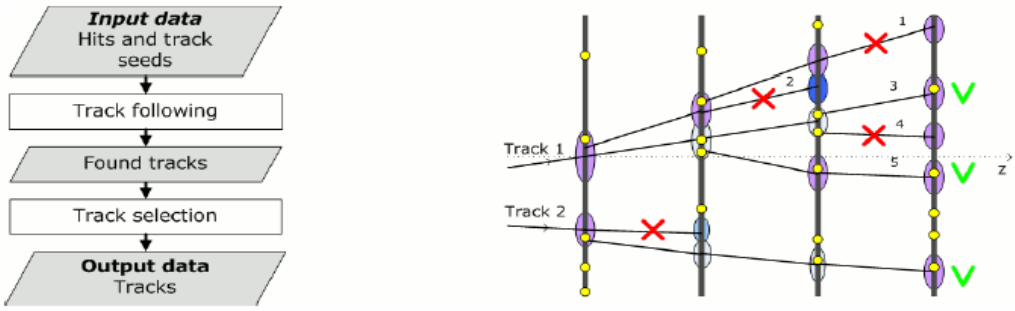

Figure 3.3: *Flowchart [left] and sketch [right] of the track finding algorithm.*

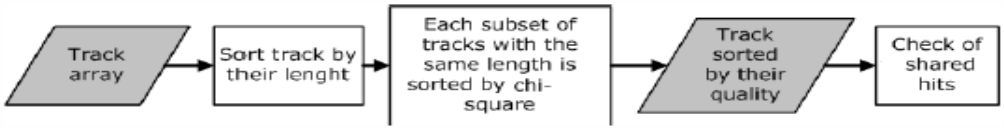

Figure 3.4: *Track selection flowchart.*

events in a fixed target geometry poses severe challenges to the tracking detectors and to the reconstruction algorithms. The central tracking detector in the CBM experiment is the STS. In order to optimize the STS layout we perform simulations of central Au+Au collisions which produce the highest track densities envisaged for the experiment. The events are generated with the UrQMD code [46], transported through the STS with GEANT3 [47, 48]. The simulated tracks of a central Au+Au collision at 25 AGeV are shown in Fig. 3.5. The simulated tracks are reconstructed with a Cellular Automaton

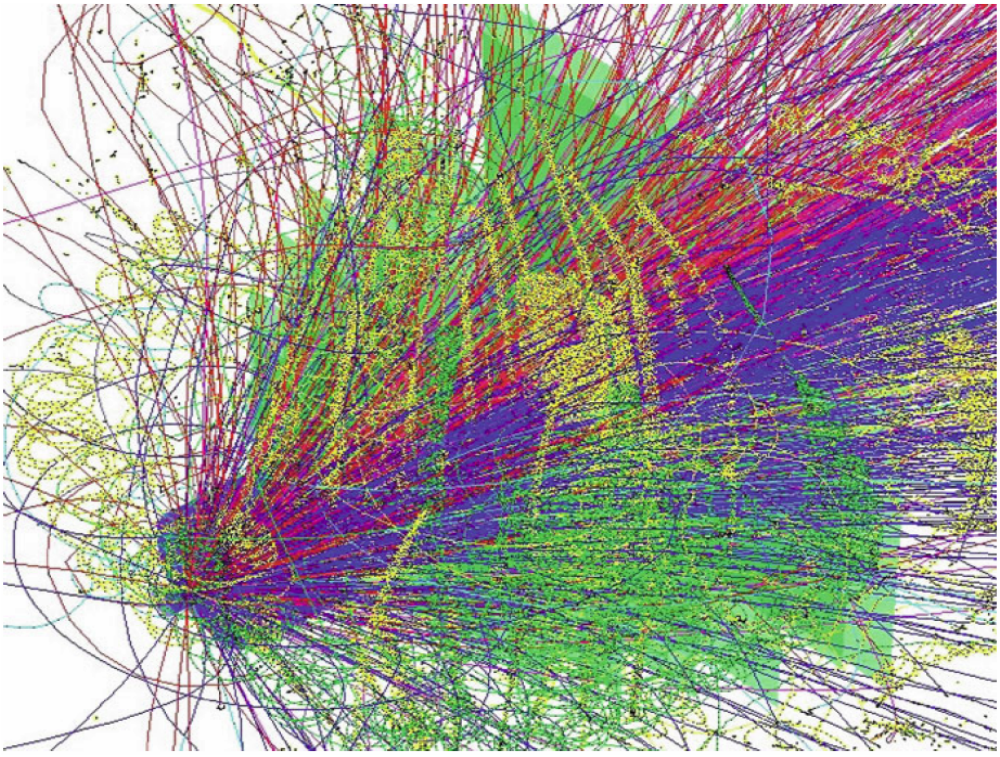

Figure 3.5: *Particle tracks in the STS simulated for a central Au+Au collision at a beam energy of 25 AGeV. The particles are produced with the UrQMD event generator, and transported through the STS with the GEANT3 code which calculated the hits in the detector layers.*

algorithm and a Kalman filter. The resulting track reconstruction efficiencies

and the momentum resolution are shown in Fig. 3.6. In the next step, STS tracks are extrapolated through the TRD stations and matched to hits of the TOF-RPC detector [49, 50, 51, 52, 53, 54]. A global track reconstruction efficiency for charged particles of 86% is reached including matching to TOF hits. In case the STS is followed by the muon absorber system, STS tracks are extrapolated through the iron absorbers with its intermediate tracking stations. For the plots of Fig. 3.6, all meson sources are generated simultaneously with proper weights using the PLUTO code (version 4.08) [55, 56].

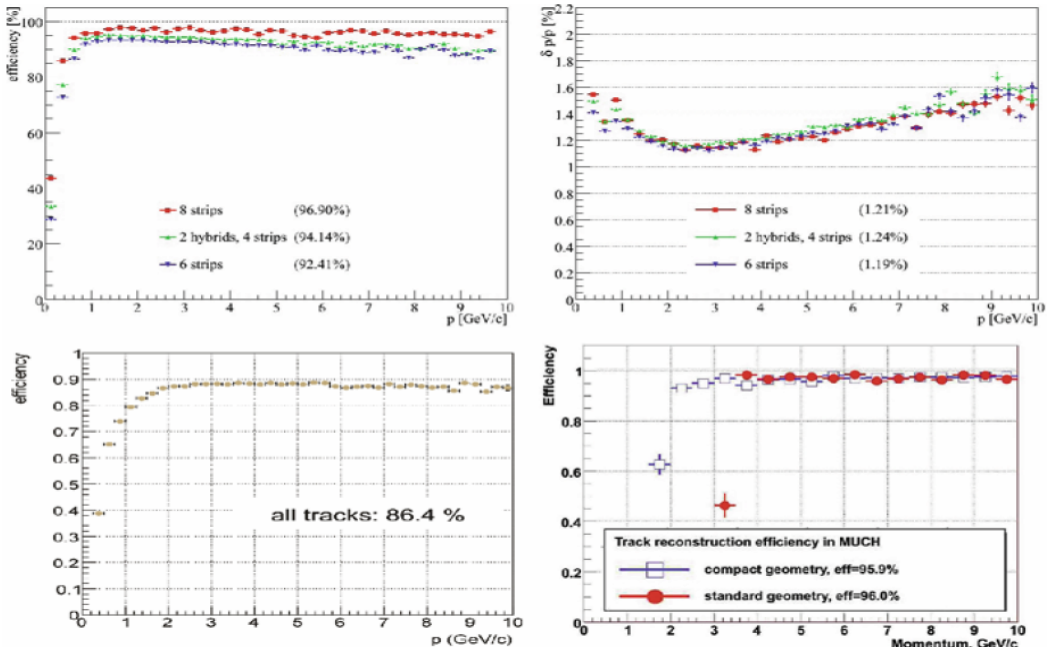

Figure 3.6: *Track reconstruction efficiency for primary vertex tracks in the STS (top left); momentum resolution in the STS (top right); global track reconstruction efficiency for STS-TRD-TOF system (bottom left); global track reconstruction efficiency for muons embedded into UrQMD events for STS-MUCH system for 1.25 and 2.25 m absorber length (bottom right).*

The CBM detector accepts charged particles emitted at polar angles between 2.5° to 25° in the laboratory and this geometrical acceptance corre-

sponds to a pseudorapidity window of $\Delta\eta = 2.31$ (η between 3.82 and 1.51).. The resulting phase-space coverage for reconstructed pions, kaons and protons produced in Au+Au collisions at 25 AGeV is shown in Fig. 3.7 as function of transverse momentum and rapidity. For pions and protons a mo-

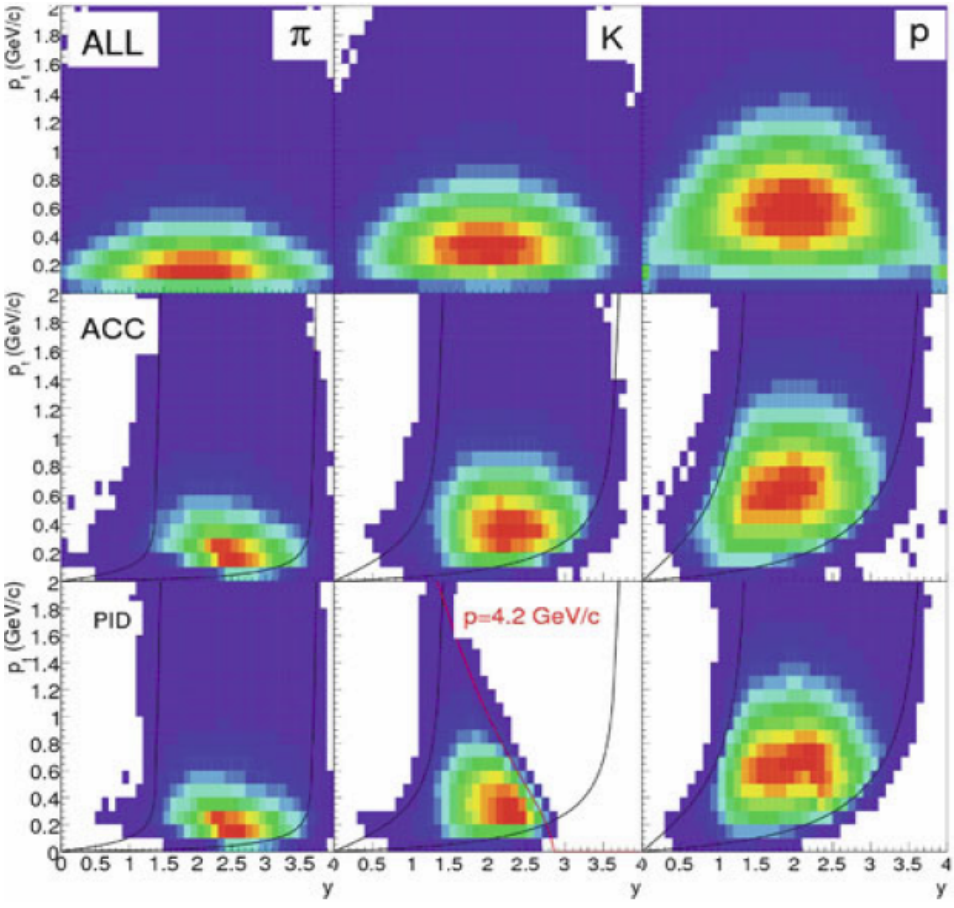

Figure 3.7: *Phase-space distributions of generated (top), geometrically accepted (middle), and identified pions, kaons and protons (bottom) for Au+Au collisions at 25A GeV*

mentum cutoff of 10 GeV/c is used. Midrapidity for 25A GeV beam energy lies at 2, for 15 and 35A GeV at 1.75 and 2.16, respectively. The CBM phase space coverage allows the extrapolation to 4π with good precision for beam

energies from 15 to 35A GeV. For a beam energy of 25A GeV, for example, 38% of the generated kaons are geometrically accepted, and 18.4% of the emitted kaons can be reconstructed and identified with a purity of 90%.

3.2 Muon simulation

The CBM muon detection system is designed to measure muon pairs from the decay of vector mesons ($\rho, \omega, \phi, J/\psi$) produced in heavy-ion collisions. At FAIR energies the muon momenta can be rather low, and, therefore, we develop a muon detection concept with a dynamical definition of absorber thickness according to the muon momentum. The actual design of the muon detector system consists of 6 hadron absorber layers (iron plates of thickness 20, 20, 20, 30, 35, 100 cm) and 18 gaseous tracking chambers located in triplets behind each iron slab; but the simulation regarding the number, position and dimensions of layers is still continuing [57]. The absorber/detector system is placed downstream of the STS which determines the particle momentum. The definition of a muon depends on its momentum which varies with the mass of the vector mesons and with beam energy. For example, muons from the decay of J/ψ mesons have to pass all 6 absorber layers with a total iron thickness of 225 cm corresponding to 13.4 interaction length λ_I. The muons from the decay of low-mass vector mesons (ρ, ω, ϕ) only have to penetrate through 5 iron absorber layers with a total thickness of 125 cm (corresponding to 7.5 λ_I).

The experimental challenge here is to reconstruct the tracks of charged particles which penetrate the segmented hadron absorber. With increasing first absorber thickness the particle multiplicity decreases, but the multiple scattering increases. The multiplicity at thickness zero corresponds to the

number of particles in front of the absorber. The yield behind the absorber is dominated by secondary electrons. In order to reduce the hit density in the first muon tracking detector to a tolerable level the absorber should have a thickness of at least $20cm$.

The feasibility studies discussed below are performed for central Au+Au collisions. The background is generated using UrQMD events. The multiplicities of vector mesons are taken from the HSD code. The momentum distributions of the vector mesons and of their decay products are calculated using the thermal source generator PLUTO. Finally the muon pairs are embedded into UrQMD events and are transported through the detector setup using the GEANT3 transport code. The analysis of the simulated data is based on full track reconstruction in the STS and in the muon chambers. The pad size in the muon detectors varies between 0.14 $\times 0.28cm^2$ and 2.22 $\times 4.44cm^2$.

In order to study the performance of the CBM muon detection system, the reconstructed particle tracks which pass the absorbers have been analyzed. The simulations were performed for a total iron absorber thickness of $1.25m$ of iron which is used for the measurement of muons from low-mass vector mesons, and for a thickness of $2.25m$ of iron used for charmonium measurements. The results are presented in Fig. 3.8 which depicts the composition of reconstructed particles per central Au+Au collision. For the thin absorber in total about 0.2 tracks are reconstructed per event, the dominating contribution (about 50%) are muons from weak decays which are wrongly matched to the tracks of their mother particles. For an absorber thickness of 2.25m only 0.02 tracks are reconstructed per event, 90% of them being muons.

The background contribution from muons from weak decays is surpris-

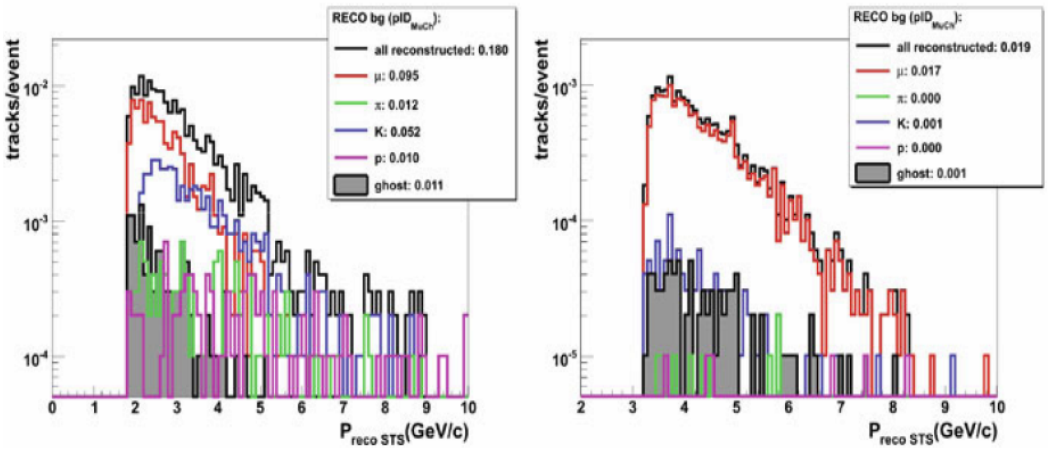

Figure 3.8: *Reconstructed background tracks per event simulated for central Au+Au collision at a beam energy of 25A GeV. The integrated yields of the different background contributions are given in the insert. The calculations are performed for a total iron absorber thickness of 1.25m (left) and for a thickness of 2.25m (right).*

ingly small as compared to the 800 charged pions produced in the collision. The reason is that most of the weak pion and kaon decays are recognized (and rejected) by the track reconstruction routines of the STS. This is illustrated in Fig. 3.9 where the number of muons from weak decays is shown as function of the z-position of the decay vertex. It turns out that in average 2.4 muons from weak decays are reconstructed per event in the STS, and only 0.4 muons survive the cut on the primary vertex. These muons stem from decays which happen shortly downstream of the target, and, hence, their tracks are perfectly reconstructible in the STS. The first STS station is located $30cm$ downstream of the target. The kaons and protons with punch through the absorber can by further rejected by a condition on their time of flight. This information can be obtained from the ToF wall for the J/ψ analysis where the full absorber ($2.25m$ iron) is required. For the detection

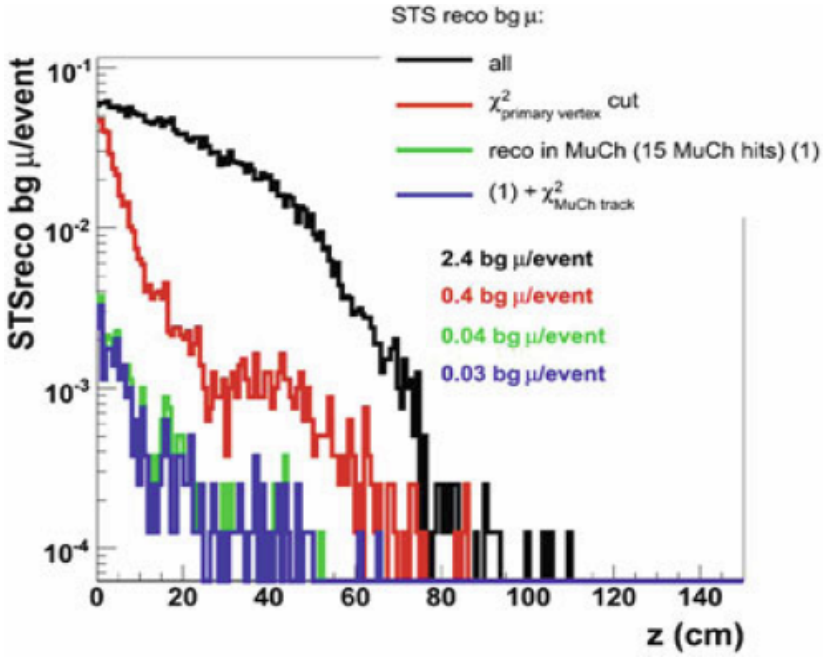

Figure 3.9: *Production vertex in z-direction of secondary muons reconstructed in the STS (central Au+Au collision, 25A GeV); from top to bottom: all (black), muons surviving the χ^2 cut for selecting those from the target (red), muons reconstructed in the muon detector (green) and surviving a χ^2 cut on the track quality in the MUCH detector (blue).*

of muons from low-mass vector mesons an additional RPC-TOF detector can be installed in front of the last iron block of $1m$ thickness. The additional condition on time-of-flight reduces the efficiency for the signal, but increases the signal-to-background ratio.

3.2.1 Invariant mass spectra and phase-space coverage

The combined performance of the STS and the muon detection system as described above is illustrated in Fig. 3.10 which displays the invariant mass spectra of muon pairs in the region of low-mass vector mesons (left panel)

and for charmonium (right panel) simulated for central Au+Au collisions at a beam energy of 25A GeV. In the analysis of low-mass vector mesons not only

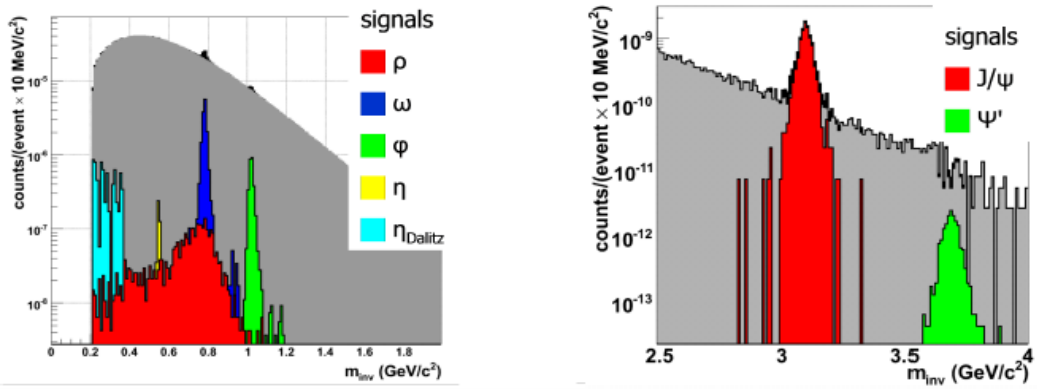

Figure 3.10: *Invariant dimuon mass spectra calculated for* 4×10^8 *(left) and* 3.8×10^{10} *(right) central Au+Au collisions at 25A GeV beam energy. Leftpanel: low-mass range including as dimuon signals* η*-Dalitz decays. The data include "hard-hard" as well as "hardsoft" pairs without any cuts on momentum. "Hard" muons traverse 1.25m of iron, "soft" muons pass only 0.9m of iron. Rightpanel: charmonium mass range. A minimal transverse momentum of* $p_t > 1$ *GeV/c is required for single muons. No ToF information is used for these spectra.*

pairs of "hard" muons are included, i.e., muons which pass $1.25m$ of iron, but also pairs of "hard" and "soft" muons where the latter only pass $0.9m$ of iron. In this way the reconstruction efficiency for low-mass vector mesons is increased, with only little effect on the signal-to-background ratio. For the analysis of charmonium only pairs of "hard" muons (penetrating $2.25m$ of iron) are considered, no cut on transverse momentum is applied. The signal-to- background ratio is on the order of 10 for J/ψ mesons, and about 0.1 for ψ' mesons. The latter value is based on a background extrapolation using a Gaussian distribution fitted to the spectrum.

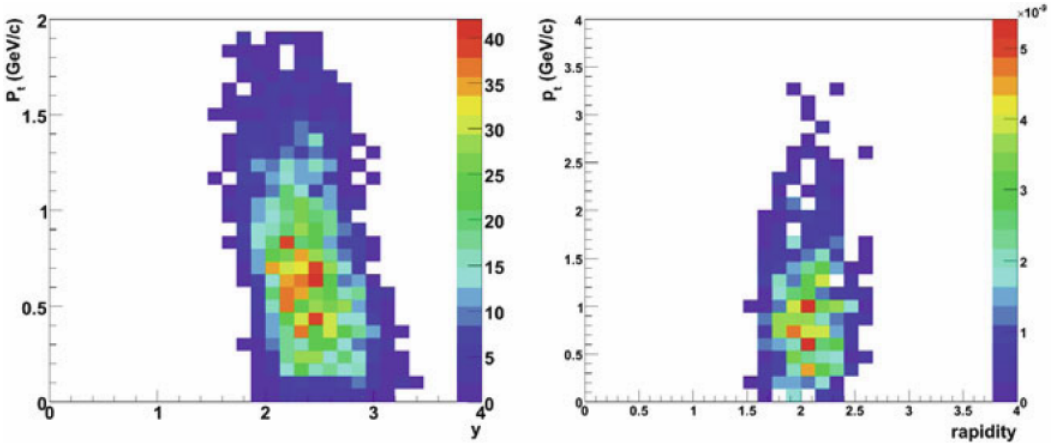

Figure 3.11: *Phase space coverage for dimuon pairs as a function of transverse momentum and rapidity calculated for central Au+Au collisions at 25A GeV beam energy (midrapidity is at y = 2). Left: ρ mesons, both "hard-hard" and "hard-soft" muon pairs were included in the analysis. Right: J/ψ meson.*

The phase-space coverage of the CBM muon detection system is shown in Fig. 3.11 for ρ mesons (left panel) and for J/ψ mesons (right panel) in the plane transverse momentum versus rapidity. In the case of the ρ mesons both "hard" + "hard" and "soft + hard" muon pairs are taken into account.

Note, that "hard" muons which traverse $1.25m$ of iron have laboratory momenta of more than $p_{lab} = 1.5GeV/c$. This intrinsic momentum cutoff is reduced to $p_{lab} = 1.2GeV/c$ for "soft" muons which have to pass only $0.9m$ of iron. Due to the absorption of muons with laboratory momenta below 1.2 GeV/c the acceptance for ρ mesons is slightly shifted to forward rapidities (midrapidity is at y=2 for 25 AGeV). In contrast, the acceptance for charmonium does not suffer from the momentum cutoff which is at $p_{lab} = 2.8GeV/c$ for an iron absorber of $2.25m$ thickness.

The acceptance for low-mass vector mesons as a function of their trans-

verse momentum and the invariant mass of the muon pairs is shown in the left panel of Fig. 3.12. The analysis includes "hard + hard" as well as "hard + soft" muon pairs. The right panel of Fig. 3.12 depicts the efficiency for muon pairs from ρ meson decays as a function of invariant mass for different thresholds in transverse momentum.

The performance of the CBM muon detection system for low-mass vector mesons can be considerably improved when installing a time-of-flight detector between the second last and the last absorber of $1m$ thickness. Fig. 3.12 presents the invariant mass spectra of muon pairs calculated for central Au+Au collisions at 25A GeV. In the analysis only "hard+hard" muon pairs are taken into account. The figure presents results obtained without (left panel) and with an additional condition on the time-of-flight information (right panel) assuming a time resolution of $80ps$. In the latter case the reconstruction efficiencies are 1% for ρ and ω mesons, and 2.8% for ϕ mesons.

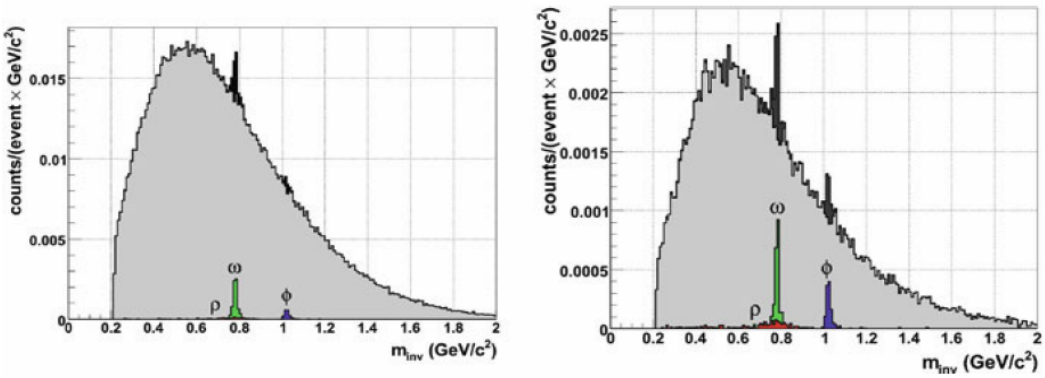

Figure 3.12: *Invariant dimuon mass spectra calculated for central Au+Au collisions at 25A GeV beam energy. The analysis includes pairs of "hard" muons only. Left: no ToF information used. Right: with a condition on ToF given by a ToF wall installed in front of the last iron absorber of 1m thickness.*

3.2.2 Dimuon Trigger studies

High statistics measurements of lepton pairs from the decay of vector mesons ($\rho, \omega, \phi, J/\psi$) produced in heavy-ion collisions require high reaction rates, and, hence, a selective trigger. The low particle multiplicities behind the hadron absorber of the CBM muon detection system enable the implementation of a fast trigger on muon pairs. The CBM trigger concept is flexible with respect to the muon momentum which depends on the mass of the vector meson and on the beam energy. Only the last 3 muon chambers located behind the full absorber of 225 cm iron will be used for the generation of a charmonium trigger. The trigger on low-mass vector mesons will be derived from hits in the 3 muon tracking chambers in front of the last absorber (after $125cm$ of iron). In this case, the tracks stop in the last absorber, and no hits are measured behind. The trigger generation proceeds via the following steps: (i) selection of events with at least 6 hits in the last (or second last) detector triplet, (ii) calculation of a track segment by a linear fit of the hit positions, (iii) extrapolation of the track segment to the vertex, and selection of tracks according to the fit parameters (χ^2 and vertex). Optionally, the ToF information is included in the trigger on charmonia. The event selection will be performed online by the CBM computer farm based on many-core processors.

The quality of the track extrapolation depends on the position resolution of the muon trigger chambers. Therefore, the trigger performance has been investigated for different granularities of the muon chambers. The results shown below were obtained with a pad size of $2.23 \times 4.48 cm^2$. The track selection criteria are the χ^2 of the fit, the X- and Y -distributions at Z = 0. The trigger performance is quantified by the background suppression factor (which is the fraction of minimum bias events which survive the trigger cuts)

and by the efficiency for J/ψ mesons which pass the trigger conditions. The background suppression factor and the J/ψ trigger efficiency for minimum bias Au+Au collisions at 25A GeV are listed in Table 3.1. The background suppression factor decreases by about a factor of 2 if the pad size of the muon detectors is increased by a factor of 2. The trigger performance is increased by more than a factor of three if the ToF information is included (see last column of Table 3.1).

The CBM data acquisition system is able to process minimum bias Au+Au collisions up to a reaction rate of 25 kHz without trigger reduction. Hence, the CBM experiment can be operated at the full design luminosity of 10 MHz if the event rate is reduced by a factor of 400. This factor is easily achieved by the dimuon trigger even without time-of-flight selection (Table 3.7). In order to test the robustness of the trigger concept with respect to additional detector noise we added 10 hits in each muon chamber of the trigger triplet. It turns out that the background reduction factor is reduced by about 15% only. For low-mass vector mesons only the selection criteria based on the track quality is applied. Due to the high hit density in detector triplet in front of the last absorber layer a background suppression factor of about 20 can be achieved without appreciable loss of signals. This factor would permit to run the CBM experiment with about 0.5 MHz. Studies are in progress to improve the trigger concept for low-mass vector mesons by taking into account the track and momentum information from the STS.

3.3 Expected particle yields

Now in the following the rates and yields of various particles, to be measured with CBM under typical running conditions, are estimated. The estimates

Trigger cuts	No cuts	MuCh	MuCh+ToF
BSF	1	606	2222
J/ψ eff.(%)	20.3	15.2	13.7

Table 3.1: *Background suppression factor (BSF) for minimum bias Au+Au collisions at 25A GeV and detection efficiency for J/ψ mesons after different trigger conditions*

are based on particle multiplicities predicted by the HSD transport code version V2.4 for Au+Au collisions at different beam energies. The multiplicities are calculated for central collisions and scaled down by a factor of 5 corresponding to minimum bias collisions. This factor was derived from the pion multiplicities which were calculated for both central and minimum bias collisions. Acceptances and efficiencies were determined by full detector simulations including event reconstruction and particle.

The yields are based on a data archiving rate of 1 Gb/s. If no online event selection can be performed, this rate corresponds to about 25 kHz minimum bias Au+Au collisions at FAIR energies. This is the case for the measurement of hadrons (including multi-strange hyperons) and of low-mass dielectrons. Online event selection is possible for the measurement of low-mass dimuons, D mesons, and of charmonia (both in the electron and muon channel). For low-mass dimuons an event-suppression factor of 20 can be achieved for minimum bias collisions allowing for a primary reaction rate of 500 kHz. For open charm, the online track reconstruction algorithms select events with displaced vertices, and are able to reject about 99% of the reactions. This would allow to run with a primary reaction rate of about 2.5 MHz. However, the read-out speed of the CMOS sensors in the Micro-Vertex Detector limits the reaction rate to 100 kHz. In this case the event-pile up in

the MAPS detectors is well below 10, a number which can be handled by the track reconstruction algorithms. Once faster and radiation harder ultra-thin pixel detectors are available, the performance of the online trigger system will be fully exploited. For the measurement of charmonia via the dimuon decay the online event selection is based only on the information provided by the last muon chamber triplet where the hit rate is very low. In case of charmonium measurements via the di-electron channel the generation of a trigger signal requires information from the TRD and the STS. Both for the electron and muon channel an online event suppression factor of 400-1000 is achievable, thus permitting to increase the primary reaction rate up to 10 MHz.

Chapter 4

Anisotropic Flow

4.1 Introduction

The result of a relativistic heavy ion collision is highly compressed, hot dense matter. The resultant collision can create quark gluon plasma if the required conditions are satisfied. Its formation can be probed indirectly by different signatures as its formation time is very small ($\approx 10^{-22}s$) and the volume in which it is formed is also very small. The signatures may be strangeness enhancement, dileptons, direct photons, event-by-event fluctuations [58], J/ψ suppression [59], elliptic flow. In this chapter elliptic flow will be discussed in detail.

The geometry of the collision can be described using the impact parameter, b, or the distance between the centers of the nuclei. The impact parameter gives an indication of the centrality of the collision. A small impact parameter is deemed a central collision, while a collision with a large impact parameter is known as a peripheral collision. Since the impact parameter cannot be determined experimentally, the centrality of the collision is inferred through other methods. The nucleons that overlap and participate

in the collision are called participants and the nucleons that fall outside the overlap regions are dubbed spectators. The plane defined generated by the direction of the impact parameter vector connecting the centers of the two nuclei and the collision axis is known as the reaction plane.

The produced particles are studied in a variety of ways. One of the most important variables describing a particle is its rapidity, defined as

$$y = \frac{1}{2} ln(\frac{E + P_z}{E - p_z}) \tag{4.1}$$

where E is the total energy and p_z is the momentum component in the direction of the beam. Rapidity is useful because Lorentz transformations from one frame to another are simply additive in rapidity for particles that differ by velocity along the beam. For example, a variable plotted as a function of rapidity can be shifted to the frame of reference of one of the colliding nuclei by subtracting the beam rapidity from the variable under study. Beam rapidity is given as

$$y_{beam} = \frac{1}{2} ln(\frac{E + p}{E - p}) \tag{4.2}$$

where E and p are the energy and momentum of the beam. The shape of the distribution does not change since it is merely shifted along the rapidity axis. In addition the mid-rapidity corresponds to the rapidity of the colliding system between projectile and target rapidity; here highest nuclear densities are reached and nucleons are excited to hadronic resonances. Consequently, one expects secondary particles to be produced mainly at mid-rapidity.

It is difficult to find experimentally the rapidity of a detected particle since it involves identifying the particle and finding its momentum. It is easier to determine the pseudorapidity, η, instead of rapidity:

$$\eta = -ln \tan(\frac{\theta}{2}) \tag{4.3}$$

where θ is the polar angle with respect to the beam axis.

$$\eta = \frac{1}{2} ln(\frac{|p| + p_z}{|p| - p_z}) \tag{4.4}$$

Besides there is a relation between x- and y- momentum components of the transverse plane and the azimuthal angle ϕ of the emitted particle (with respect to the x-axis) in a heavy-ion collision as

$$\phi = \tan^{-1} \frac{p_y}{p_x} \tag{4.5}$$

Pseudorapidity is a close approximation to rapidity for particles whose velocity is close to the speed of light, where their total momentum is large compared to their mass. For particle detectors, it is the geometrical measure of the coverage of a detector. In RHIC collisions, the produced particles are mostly pions whose momenta are around a few hundred MeV/c, so pseudorapidity is a reasonable approximation to rapidity in most instances.

In a collision between two heavy nuclei, the energy source comes from the kinetical energy of the incident nucleons. This energy will be partially deposited in the system via multiple inelastic collisions among nucleons and will be split in a compressional part and a thermal part. The latter is used to produce new particles. Because the energy lost by the colliding nuclear matter is deposited in the vicinity of the centre of mass with the production of hadrons, high energy heavy ion collisions provide an excellent tool to produce regions of very high energy densities.

The nuclear stopping power, which is the degree of stopping of the incident nucleus when it impinges on the nuclear matter or another nucleus, plays an important role in heavy-ion collisions. It determines basic parameters, such as the energy density, which governs the collision dynamics, and the extent to which conditions are favourable for the formation of a deconfined

partonic phase. Experimentally, it can be evaluated from the measurement of the net rapidity distribution of the baryons.

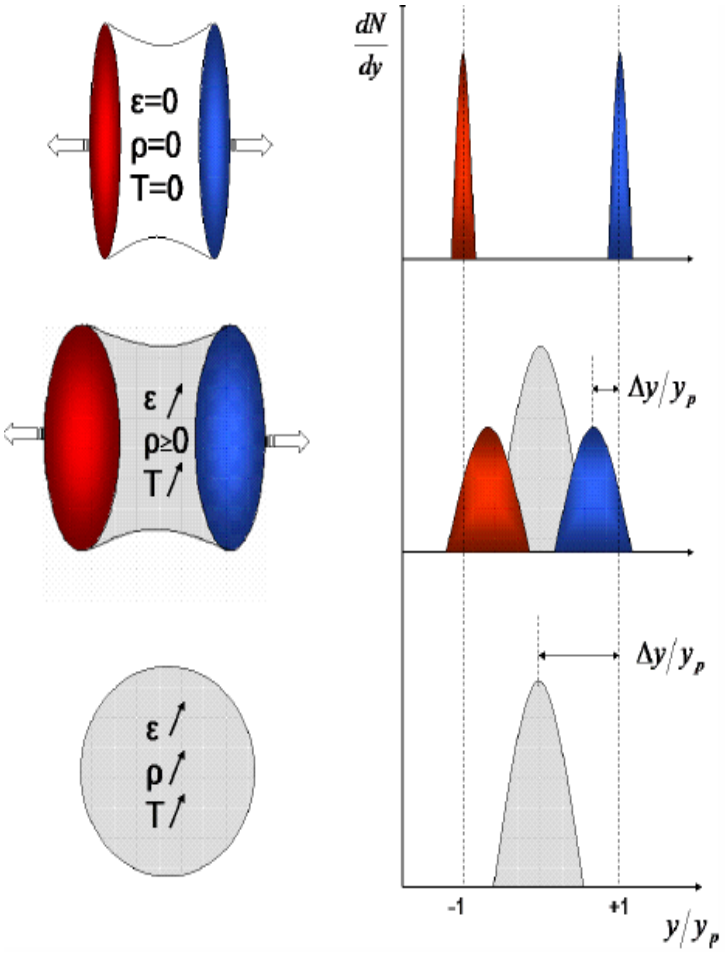

Figure 4.1: *Illustration of the nuclear stopping power as reflected by the shape of the net baryon rapidity distribution in central nucleus-nucleus collisions.*

Fig. 4.1 illustrates schematically the degree of stopping for three different collision scenarios. The upper panel shows a fictive scenario, where the nuclei are completely transparent to each other: they traverse each other without interacting. In this case the rapidity does not change. In the second scenario (mid-panel), the nuclei are partially decelerated. The rapidity dis-

tribution is only slightly different than the initial one. The energy density and temperature increase leading to the creation of quark-antiquark pairs and consequently to the production of mesons (essentially) and baryons in the mid-rapidity region (gray area in the Fig. 4.1). As the nucleons are not completely stopped, the net baryonic density is low in the mid-rapidity region (and high at $y/y_p \approx 1$). The last scenario (lower panel) corresponds to a full stopping situation of the incoming nuclei, leading to an accumulation of the initial baryons at the point of impact and, therefore, to a high net baryon density in the mid-rapidity region. In the figure, the rapidity of baryons is normalised to the rapidity of the projectile in the centre-of-mass system (y_p).

4.1.1 Collective Motion

In order to establish and describe the quasimacroscopic properties of nuclear matter, it is necessary to investigate collective observables. Collectivity in this context means that a number of ejectiles exhibit a common property e.g., the emission of many particles of the same kind or the emission of many ejectiles with a common velocity field or into a common direction. Restricting this very general definition of collective behavior to kinematic observables leads to the definition of collective flow: Any common feature of all the ejectiles emitted in a heavy-ion collision can be taken as an indicator for the underlying nuclear-matter phase space distribution. The flow signals the presence of multiple interactions between the constituents of the medium created in the collision. More interactions usually lead to a larger magnitude of the flow and brings the system closer to thermalization.

Fig. 4.2 shows the time immediately following the typical nuclear collision with the spectators. The hot, dense interaction region begins to expand. The compression and resulting expansion in the interaction region produces

a collective flow of particles. There are four types of particle flow terms: longitudinal, radial, directed and elliptical. Longitudinal flow is the flow of particles along the beam direction (z direction). Radial flow characterizes particles that are emitted from a source with a common velocity field independent of the direction, i.e., for a velocity field with spherical symmetry. Directed and elliptic flows measure the azimuthal asymmetry of the particle distribution (which are together known as transverse flow). Directed flow is an enhanced emission of particles into the direction, defined by the orientation of the impact parameter vector in nucleus-nucleus collisions. Elliptic flow [60, 61] describes an emission pattern in which particles are found to be preferentially emitted with respect to a certain azimuthal angle and with back-to-back symmetry.

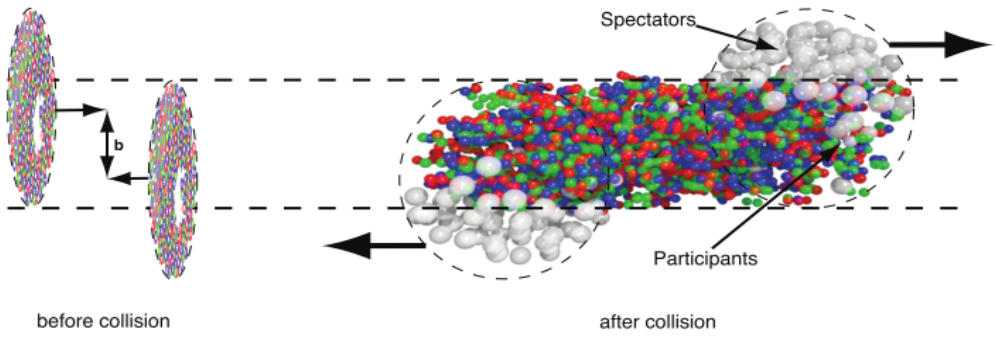

Figure 4.2: *Left: The two heavy-ions before collision with impact parameter b. Right: The spectators continue unaffected, while in the participant zone particle production takes place.*

The exploration of the transverse collective flow is the earliest predicted observable to probe heated and compressed nuclear matter [62]. The transverse flow is intimately connected to the pressure gradients. Therefore, it is sensitive to the equation of state (EoS) and might be used to search for abnormal matter states and phase transitions [63, 64, 65].

4.1.2 Time Evolution

In order to define more clearly the most relevant quantities for collective motion in heavy-ion collisions, let us consider the Fig. 4.3, where two nuclei are seen approaching each other for collision.

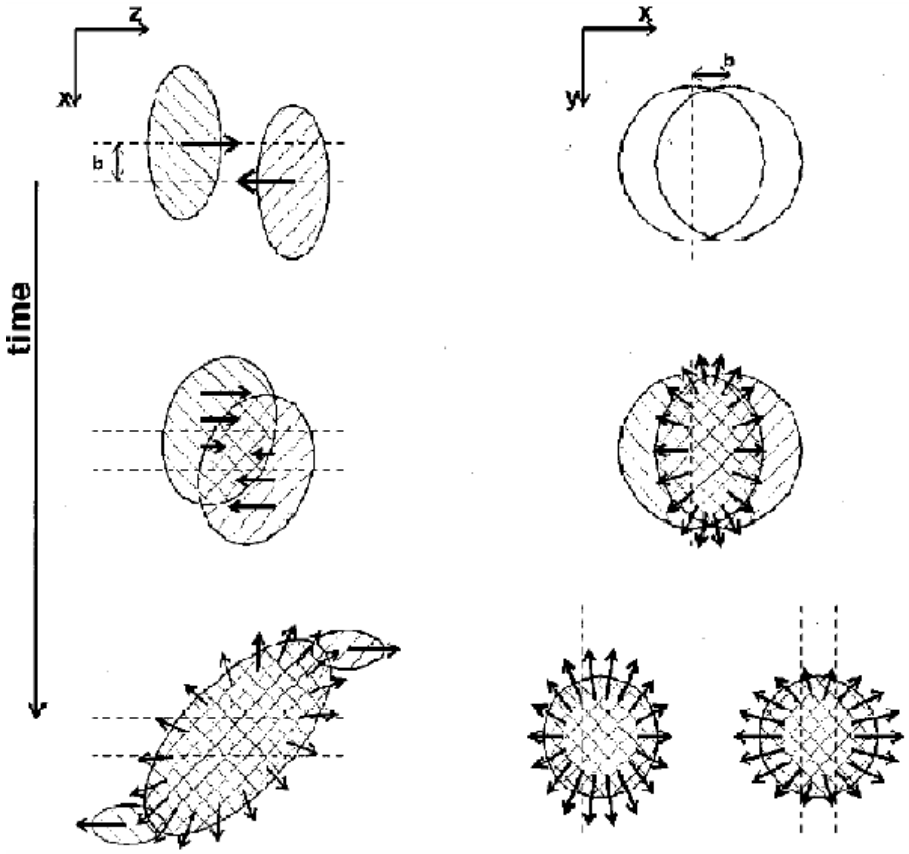

Figure 4.3: *Schematic view of the time evolution in a heavy-ion collision and the development of the collective velocity fields. Left, the time evolution of the reaction in the reaction plane. Right, a sketch of the transverse plane at midrapidity.*

Initial Phase

When the two matter distributions approach each other and start to overlap, the properties of the NN interaction in free space will be visible in the scattering process. Nucleons at the surfaces will reflect the Lorentz-force-like behavior of the NN interaction most directly. They will be deflected outward and hence show an enhancement in the reaction plane [66, 67, 68].

High-Density Phase

Once the matter distributions of the projectile and target overlap, the properties of the NN interaction are not well known. At incident beam energies that exceed the velocity of sound in nuclear matter at ground-state nuclear-matter density ($\beta_s = 0.2$), the nucleons cannot escape fast enough and a zone of high density is formed. Many-body effects that are present even at normal nuclear-matter densities can occur, as well as modifications of the properties of the constituents (medium effects) [69, 70], and eventually, at high energies, even the transition to QGP. For large systems and large enough cross sections, the overlap zone develops into a system characterized by an initial baryon number and energy density. Depending on its EoS, which relates the pressure to the density and temperature, the overlap zone may reach conditions that are described by an average density and temperature. This process of heating and compressing is intimately connected to the question of stopping, namely how much energy of the original longitudinal motion is transferred into internal degrees of freedom in the course of the reaction. Having stored part of the available energy in compression and thermal excitation, heavy-ion collisions produce unique conditions of nuclear matter that are not accessible otherwise. Under these conditions, new particle species can be created and their abundance and emission pattern can be used to

probe the global properties of their surroundings.

For finite impact parameters, the spectator nucleons never undergo a collision with nucleons of the collision partner. These nucleons experience only the (distorted) mean field of their parent nuclei and propagate with little deflection. They do, however, play a crucial role in diagnosing the properties of the central collision.

Expansion

The next stage in the reaction scenario is the relaxation of the energy density. The central system is undergoing expansion, thereby reducing its temperature and density. For symmetry reasons, the expansion is azimuthally symmetric for central collisions. For reactions with finite impact parameter, where an oriented velocity field might have survived the compression phase, the situation is much more complicated. The expansion now has a directed velocity field superimposed (Fig. 4.3). The system always expands into the direction of the largest gradients in density and temperature. Besides, in the transverse direction, the initial expansion is largest in the direction of the reaction plane. In longitudinal direction, the expansion scenario depends on the degree of stopping. For a high degree of stopping and given the fact that the nuclei are Lorentz contracted in this direction, the pressure gradient is largest along the beam direction; therefore, the system relaxes predominantly longitudinally [71]. For a transparent system, the rapidity distributions are longitudinally broadened because of the initial distribution. In the limit of very high incident energy, this figure predicts a complete decoupling of longitudinal and transverse expansion [72].

The speed of the expansion is given by the relaxation constants and introduces a time scale that has to be compared with the time scale imposed

by the velocity of the incident beam:

$$t = (R_p + R_t)/\gamma v_{beam}, \tag{4.6}$$

where R_p and R_t are the radii of the projectile and target nuclei, respectively. Depending on the speed of the expansion, hot matter may interact with cold spectator matter. Their interaction causes a distortion of the azimuthal angular distribution. For elastic collisions, this process is rescattering, and for inelastic collisions it leads to absorption. Provided the expansion is fast with respect to the longitudinal motion, nucleons participating in the expansion are absorbed preferentially in the reaction plane, where spectator material is present. This scenario is found at beam energies around 1A GeV. With increasing beam energies, the velocity of the spectators increases much faster than the time needed for the expansion of the compressed and heated central overlap system. Then the expansion can progress more and more freely into the reaction plane direction. This scenario is observed at incident energies above 2A GeV.

Freeze-Out

The reaction, and the development of collective signatures, stops at a point commonly referred to as freeze-out. At this point the densities are small enough that during a typical path length no further interaction will occur. The properties of the system at freeze-out are quite well known from the systematic study of particle ratios [73, 74]. Temperatures and baryon chemical potentials can be extracted signifying that, at incident beam energies beyond about 10A GeV, conditions are very close to the hypothetical phase boundary to the QGP. This makes the study of collective phenomena even more important, since it allows a systematic comparison between the situation at

lower beam energies, which is solely described by the properties of a hadron gas, and the situation and the situation in which a new phase of matter is possibly produced. Although many hadronic observables (e.g., particle ratios) lose memory of the initial conditions during the equilibration process, various signatures are expected to be visible from hadrons, especially in observables based on collective flow (since flow is built up over the full collision history). Because of its larger number of degrees of freedom, the QGP phase has a lower pressure than a purely hadronic phase. This reduces the speed of the expansion, the amount of sideflow [75, 76], and the elliptic flow [77]. For special initial conditions, the so-called softest point of the EoS should produce systems that are especially long-lived.

4.1.3 Excitation Function—Competition of Time Scales

With the available data spanning nearly four orders of magnitude in beam energy, it is a challenge to establish common features. From the discussion of the time evolution, it can be expected that the various phases contribute differently to the final observables. Several time scales need to be considered: (a) the passing time of the nuclei, t_{pass}, (b) the equilibration time of the overlap zone (fireball), t_{eq}, and (c) the expansion time, t_{ex}.

Whereas t_{pass} is directly related to the incident beam energy, the other two time scales depend on the properties of the nuclear matter under investigation. Equilibration is determined by the strength of the interaction of the constituents and the number of collisions among them. Over the incident energy range considered here, the initial constituents might even change from hadrons to quarks and gluons, so there is no a priori knowledge about this process. A similar statement holds for the expansion. This process is driven by the thermal pressure and the compressional energy. The energy contents

and the separation into a randomized (thermal) part and a potential energy part depend on the number of degrees of freedom in the system and its EoS. Detailed comparison to dynamical models is mandatory for interpreting the data.

The theoretical tools for describing flow are hydrodynamics or microscopic transport (cascade) models. In the transport models, flow depends on the opacity of the medium, be it partonic or hadronic. Hydrodynamics becomes applicable when the mean free path of the particles is much smaller than the system size, and allows for a description of the system in terms of macroscopic quantities. This gives a handle on the EoS of the flowing matter.

For the simplest perfect (minimum-viscosity) fluid, the following points should be emphasized:

• Hydrodynamics in the simplest case treats the substance as an ideal fluid [78].

• The pressure gradient that drives elliptic flow is self-quenching [79]. The pressure gradient drives the source shape in the direction of being closer to isotropic.

• Hadrons freeze-out of any produced QGP phase by coalescence [80]. In coalescence, particles form from comoving quarks that are close together in phase space (similar spatial and momentum coordinates).

• If a QGP phase exists during hydrodynamic expansion, one consequence is constituent quark scaling [81]. If elliptic flow develops at the quark level, the final-state elliptic flow for each particle type should scale with the number of constituent quarks. For example, the elliptic flow ratio for baryons (composed of 3 quarks of total transverse momentum 3p) to mesons (quark + antiquark, transverse momentum 2p) is simple the ratio of quarks. In this case, the ratio should be 3/2.

• Another feature seen in hydrodynamic elliptic flow is *mass ordering* [82]. In the range of $p_T \leq 1.5$ GeV/c, the flow is species (mass) dependent, with lighter particles developing elliptic flow at a smaller p_T. This is consistent with an ideal hadronic fluid, because the fluid cells evolve with a common velocity [83]. Heavy particles traveling at the same velocity as light particles necessarily have more momentum, $\vec{v} = \frac{\vec{p}}{E}$. The breakdown of mass ordering at higher p_T is a possible sign of QGP formation. It suggests that the fluid constituents are not hadrons.

• Elliptic flow as a function of p_T *saturates* at some p_T. Saturation means that the flow pattern flattens and doesnt have an explicit p_T dependence.

4.1.4 Directed Flow

Experimentally, the most direct evidence of flow comes from the observation of anisotropic flow, which is the anisotropy in particle momentum distributions correlated to the reaction plane. The azimuthal anisotropy in particle production is the clearest experimental signature of collective flow in heavy-ion collisions [84, 85, 86, 87, 88]. Rescattering within the interaction regions almond shaped spatial anisotropy will give rise to a momentum anisotropy that may be observed.

The momentum anisotropy is examined by performing a Fourier decomposition of the momentum space particle distribution in the x-y plane [89, 90, 91]. This gives us the following equation

$$\frac{dN}{d\phi} \propto 1 + 2\Sigma v_n \cos[n(\phi - \Psi)], \tag{4.7}$$

where N is the number of particles, v_1 is the first coefficient of the Fourier expansion of the azimuthal distribution of the emitted particles describing directed-in-plane flow, v_2 is the second Fourier coefficient of anisotropy known

as elliptic flow, and ϕ is the azimuth angle of the particle, and Ψ denotes the orientation of the reaction plane and incoming beam direction.

The directed flow measures the total amount of transverse flow; and has a definite direction, along the impact parameter. It is most pronounced in semi-central interactions around target and projectile rapidities where the spectators are deflected away from the beam axis due to a bounce-off from the compressed and heated matter in the overlap region. v_1 is defined by

$$v_1 = \langle \frac{p_x}{\sqrt{p_x^2 + p_y^2}} \rangle = \langle \cos\phi \rangle \tag{4.8}$$

x and y are the directions perpendicular to the beam with x in the event plane. The angular brackets denote an average over all considered particles from all events.

Three different interesting properties of the directed flow have been proposed.

1. The time scales probed by the directed flow are set by the crossing time of the Lorentz-contracted nuclei. Thus, it serves as keyhole to the initial, probably non-equilibrium, stage of the reaction [92].

2. The softening of the equation of state in a first order phase transition leads to a decreasing directed flow [93, 94, 95].

3. The space-momentum correlation of the emitted particles can be addressed experimentally via the v_1 rapidity distributions of nucleons and pions.

4.2 Elliptic Flow

The second coefficient of the Fourier expansion of the azimuthal distribution of the emitted particles (v_2) is the elliptic flow [96, 97, 98, 99, 100, 101, 102]. This type of flow is strongest around central rapidities in semi-peripheral collisions. It is driven by the anisotropy of the pressure gradients, due to

the geometric anisotropy of the initial overlapping region. Fig. 4.4 shows a schematic illustration of the conversion of coordinate-space anisotropy to anisotropy in momentum space. The left panel shows the nucleons of the two colliding nuclei with an ellipse outlining the approximate interaction region. The right panel shows a momentum-space representation of v_2. The average radius of each successive ring represents the p_T of the particles while the anisotropy of the ring represents the magnitude of v_2. The highest p_T particles (outer-ring) exhibit the strongest v_2 while the lowest p_T particles (inner-ring) exhibit a vanishingly small v_2 In macroscopic terms, the almond-shaped interaction region is initially compressed and then expands as the spectator and participant matter separates from each other. Particles inside the participant region will tend to move in the direction of the largest

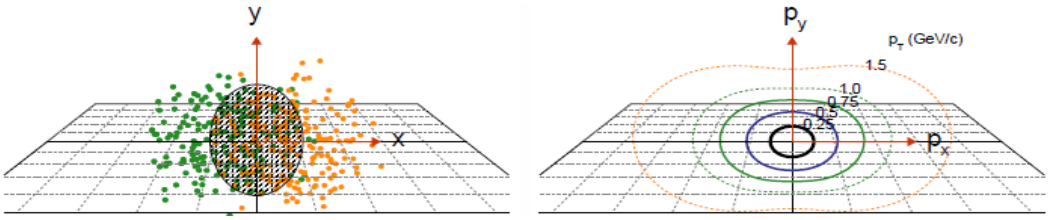

Figure 4.4: *Schematic illustrations of a* $\sqrt{s_{NN}}$ *= 200 GeV Au+Au collision with a 6 fm impact parameter.*

pressure gradient, that is, from an area of high pressure to an area of low pressure. Once the spectator matter is no longer present, the area of lowest pressure is anywhere outside the interaction region. Then it is a geometric argument; more particles will be preferentially emitted along the smaller axis. Therefore, it is a valuable tool to gain insight into the expanding stage of the fireball. v_2 [103] is defined by

$$v_2 = \langle \frac{p_x^2 - p_y^2}{p_x^2 + p_y^2} \rangle = \langle \cos 2\phi \rangle \tag{4.9}$$

There are two competing effects which lead to contributions with different signs to the integrated v_2 value. At low energies or early times there is the so called "squeeze-out" effect. The spectator matter blocks the emission in the impact parameter direction and therefore the flowing matter is "squeezed"-out perpendicularly to the reaction plane. This leads to negative elliptic flow values. The second effect is the so called in-plane flow. This type of flow becomes important at higher energies and/or later times. At higher bombarding energies ($E_{lab} \geq$ 10A GeV)the spectators leave the interaction zone quickly. The remaining hot and dense matter expands almost freely, where the surface is such that in-plane emission is preferred. Therefore the elliptic flow receives a positive contribution. Positive v_2 thus implies that more particles are emitted along the short axis of the overlap region.

As the spectator nucleons, in a heavy-ion collision, hinder the free emission from the interaction zone, this results in anisotropic azimuthal distributions of particles, velocities, momenta, or transverse energy, which are invariant under azimuthal rotation of 180°.

Let us now study the time evolution of the pressure gradients in connection with the elliptic flow development. The transverse pressure gradients for the first $10fm$ at E_{lab} = 40A GeV and the highest SPS energy are shown in Fig. 4.5. In both cases one observes large pressure gradients in the very early stage of the collision. For the lower energy the maximum is reached around t = $3fm$ and for the higher energy it is shifted to even earlier times. The difference between the pressure gradients in x- and y- direction is responsible for the v_2 development.

The Fig. 4.5 shows that the temporal evolution of elliptic flow for pions starts exactly after this maximum. In the top, dP/dx (full line), dP/dy (dotted line) and the difference between these two ΔP (dashed line) are

depicted; and the bottom shows the elliptic flow of pions (squares) versus time at mid-rapidity for mid-central collisions (b=7fm). The elliptic flow

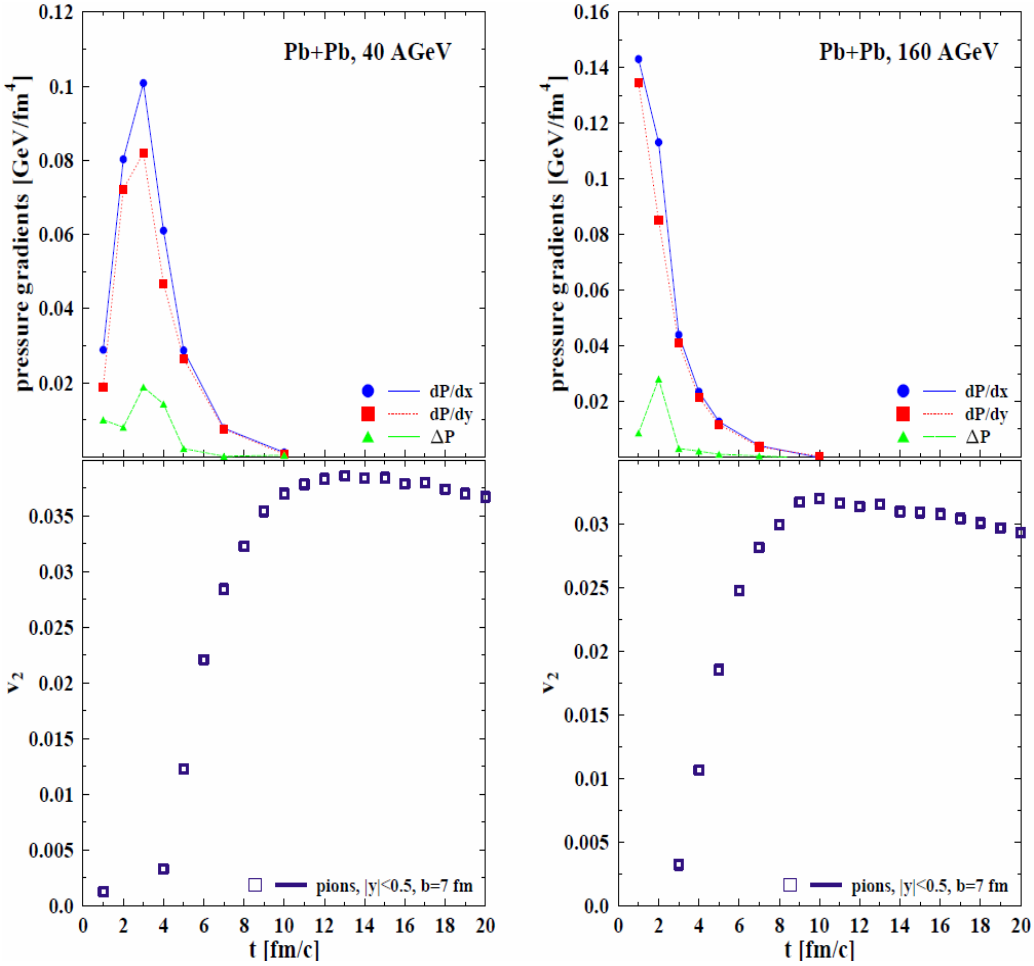

Figure 4.5: *UrQMD calculation for the time evolution of the pressure gradients and elliptic flow for Pb+Pb interactions at E_{lab} = 40 and 160 A GeV.*

increases during $\sim 6fm$ until it reaches almost its final value. After t = $10fm$ it decreases a little because of resonance decays. So, elliptic flow builds up in the early stage of the collision due to the difference of pressure gradients.

Now, the evolution of the almond shaped interaction volume is shown in

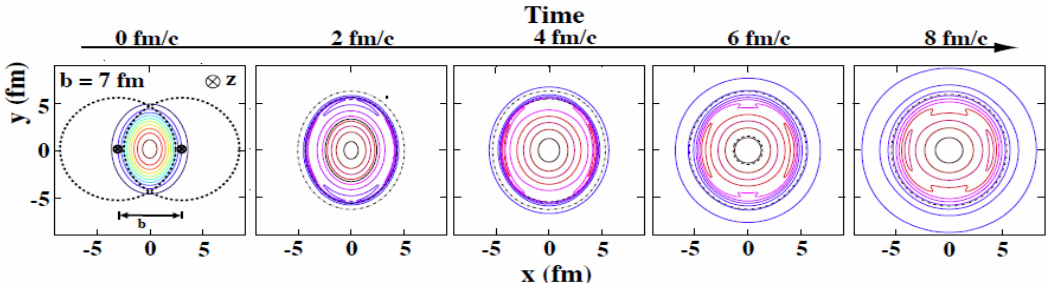

Figure 4.6: *The created initial transverse energy density profile and its time dependence in coordinate space for a non-central heavy-ion collision [104]. The z-axis is along the colliding beams, the x-axis is defined by the impact parameter.*

Fig. 4.6. The contours indicate the energy density profile and the plots from left to right show how the system evolves from an almond shaped transverse overlap region into an almost symmetric system. During this expansion, governed by the velocity of sound, the created hot and dense system cools down.

The ratio between elliptic flow and the spatial eccentricity of the overlap parametrizes the speed at which a perturbation is propagated through the system. According to ideal hydrodynamics the ratio v_2 is proportional to the initial spatial eccentricity,

$$v_2 \propto \varepsilon_s \tag{4.10}$$

The proportionality constant depends on the speed of sound c_s in the matter. The speed of sound depends on the EoS of the matter through

$$c_s^2 = \frac{dp}{d\varepsilon}, \tag{4.11}$$

where p is the pressure and ε the energy density. A softer EoS, with smaller c_s, produces smaller elliptic flow.

Fig. 4.7 shows the velocity of sound versus temperature for three different equations of state [105]. The dash-dotted line is the hadron resonance gas EoS, the red full line is a parametrization of the EoS which matches recent lattice calculations and the blue dashed line is an EoS which incorporates a first order phase transition. The arrows indicate the corresponding transition temperatures for the lattice inspired EoS and the EoS with a first order phase transition. The temperature dependence of the sound velocity clearly differs significantly between the different equations of state. Because the expansion of the system and the buildup of collective motion depend on the velocity of sound, it is expected that this difference will have a clear signature in the flow. The buildup of the flow for two different equations of state also

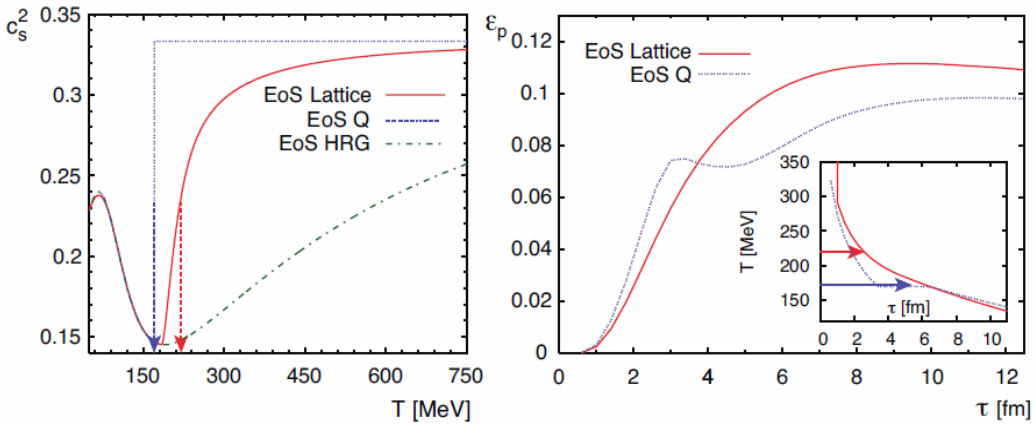

Figure 4.7: *Left: The velocity of sound squared versus temperature for three equations of state. Right: The anisotropy in momentum space for two equations of state used in hydrodynamic calculations.*

shown in Fig. 4.7. Due to the stronger expansion in the reaction plane the initial almond shape anisotropy in coordinate space vanishes, while the momentum space distribution changes in the opposite direction from being approximately azimuthally symmetric to having a preferred direction in the

reaction plane. The symmetry in momentum space can be quantified by:

$$\varepsilon_p = \frac{\langle T_{xx} - T_{yy} \rangle}{\langle T_{xx} - T_{yy} \rangle} \tag{4.12}$$

where T_{xx} and T_{yy} are the diagonal transverse components of the energy-momentum tensor and the brackets denote an averaging over the transverse plane. Fig. 4.7 shows that ε_p versus time starts at zero after which the anisotropy quickly develops and is indeed dependent on the EoS.

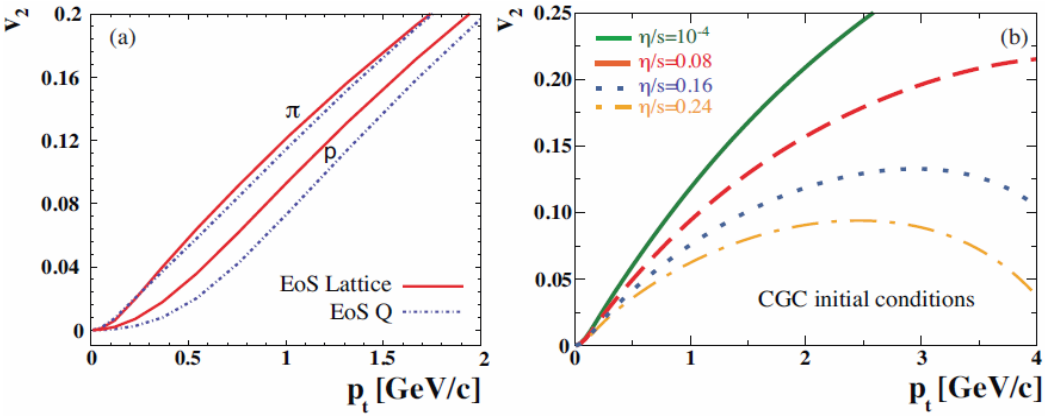

Figure 4.8: *Left: The EoS dependence of $v_2(p_T)$ for pions and protons. The full lines are for the lattice inspired EoS and the dashed lines for an EoS which incorporates a first order phase transition. Right: The dependence on η/s of $v_2(p_T)$s for charged particles [106].*

Although ε_p is not a direct observable, the observed EoS dependence of ε_p versus time is reflected in the experimental observable v_2, in particular when plotted as function of transverse momentum and particle mass. Fig. 4.8 shows p_T- differential elliptic flow for pions and protons after the transverse momentum spectra have been constrained. A clear mass dependence of v_2 at low transverse momentum is observed for both equations of state. The figure also clearly shows that the pion v_2 does not change much between the Lattice EoS and QCD EoS. On the other hand, the v_2 of protons does change

significantly because the heavier particles are more sensitive to the change in collective motion. Therefore measurements of $v_2(p_T)$ for various particle species provide an excellent constraint on the EoS in ideal hydrodynamics.

Recently, it was realized that small deviations from ideal hydrodynamics, in particular viscous corrections, already modify significantly the buildup of the elliptic flow [107]. The shear viscosity determines how good a fluid is, however, for relativistic fluids the more useful quantity is the shear viscosity over entropy ratio η/s. Known good fluids in nature have an η/s of the order of $\hbar/k_B$. In a strongly coupled $\mathbf{N} = 4$ supersymmetric Yang Mills Theory with a large number of colors ('t Hooft limit), η/s can be calculated using a gauge gravity duality [108]:

$$\frac{\eta}{s} = \frac{\hbar}{4\pi k_B}. \tag{4.13}$$

Kovtun, Son and Starinets conjectured, using the AdS/CFT correspondence, that this implies that all fluids have $\eta/s \geq \hbar/4\pi k_B$ (the KSS bound). We therefore call a fluid with $\eta/s = 1/4\pi$ (in natural units) a perfect fluid. The KSS bound raises the interesting question on how fundamental this value is in nature and if the QGP behaves like an almost perfect fluid. It is argued that the transition from hadrons to quarks and gluons occurs in the vicinity of the minimum in η/s, just as is the case for the phase transitions in helium, nitrogen, and water. An experimental measurement of the minimal value of η/s would thus pinpoint the location of the transition [109, 110].

Experimentally we might get an answer to the magnitude of η/s by measuring v_2 as shown in Fig. 4.8. The full line is close to ideal hydrodynamics ($\eta/s \sim 0$) while the three other lines correspond to η/s values of up to three times the KSS bound. Different magnitudes of η/s clearly lead to a dramatically different magnitude of v_2 and change its p_t dependence. However, the magnitude and p_t dependence of v_2 not only depend on η/s but also on the

EoS.

The magnitude of v_2 does not only depend on the medium properties of interest, but is also proportional to the initial spatial anisotropy of the collision region. This spatial anisotropy is characterized by the eccentricity defined by

$$\varepsilon_s = \langle \frac{y^2 - x^2}{y^2 + x^2} \rangle \tag{4.14}$$

where x and y are the spatial coordinates in the plane perpendicular to the collision axis. The angle brackets <> denote an average weighted by the initial density. Recent calculations have shown that the eccentricity obtained in different descriptions, in particular comparing a Glauber with a Color Glass Condensate (CGC) description, shows that ε_s varies by almost 25% at a given impact parameter [111]. The elliptic flow, obtained when using these different initial eccentricities is shown in Fig. 4.9. As expected, the different magnitude of the eccentricity propagates to the magnitude of the elliptic flow. As it is very difficult to measure the eccentricity independently, this leads to a large uncertainty in experimental determination of η/s. Thus, the elliptic

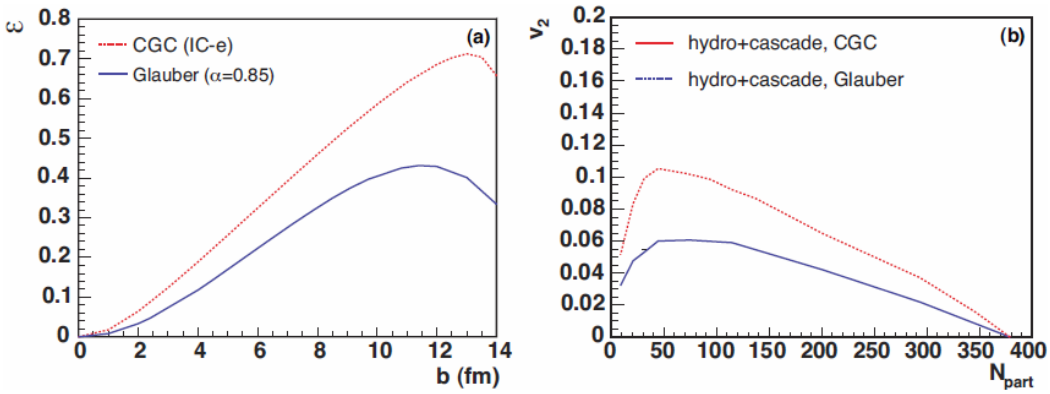

Figure 4.9: *Left: The eccentricity ϵ calculated in a color glass condensate (CGC) model and using a Glauber model. Right: The v_2 obtained using the CGC or Glauber initial eccentricity.*

flow depends on fundamental properties of the created matter, in particular the sound velocity and the shear viscosity, but also on the initial spatial eccentricity. Detailed measurements of elliptic flow as function of transverse momentum, particle mass and collision centrality provide an experimental handle on these properties.

4.2.1 Dependence of Elliptic Flow on centrality dependence

Elliptic flow depends on the event centrality: multiple scattering increases with centrality while the spatial eccentricity decreases. These two effects combined make elliptic flow low in central and in very peripheral collisions and maximum in mid-central collisions. Results of elliptic flow measurements as a function of centrality from the STAR experiment [112] are shown in Fig. 4.10, where indeed the described dependence is seen. At RHIC the dependence of v_2 on other parameters is also studied [113, 114, 115, 116, 117, 118, 119] The results are shown for four different analysis methods.

4.2.2 Dependence on transverse momentum and particle species dependence

The transverse momentum dependence of elliptic flow is shown in Fig. 4.11 for Au-Au colisions at 130 GeV. At low p_t, v_2 rises linearly and then levels off. The p_t dependence can be well described by hydrodynamics up to $p_t \approx 1GeV$, as can be seen in the figure. At higher p_t, the contribution from particles that are not correlated to the reaction plane grows, which results in a deviation from thermodynamic behaviour.

The particles that are not correlated to the reaction plane originate from

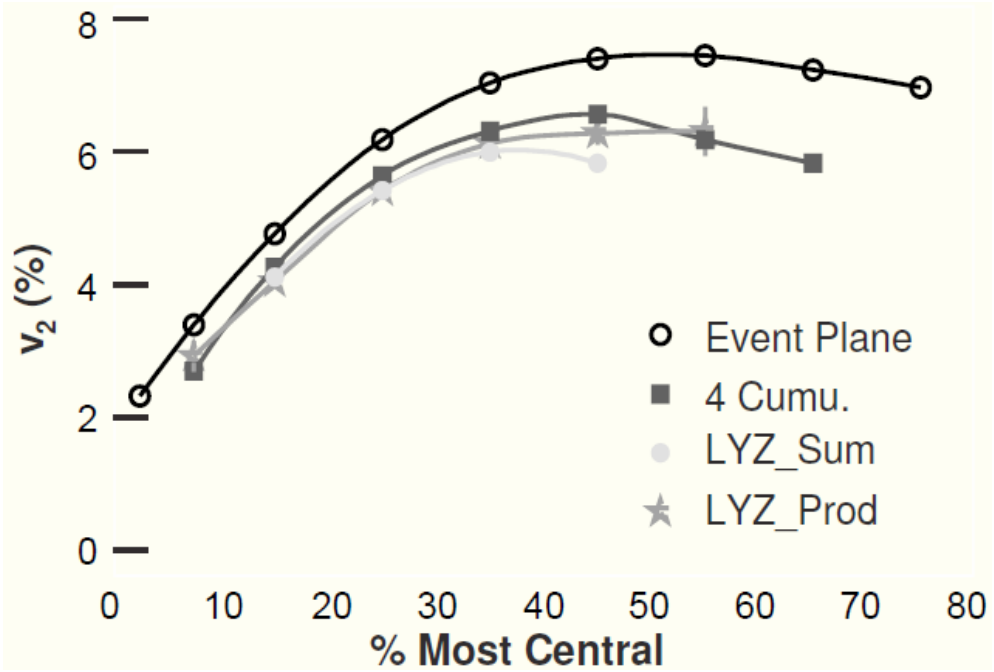

Figure 4.10: *Elliptic flow of charged hadrons as a function of the event centrality for Au-Au collisions at 200 GeV*

the initial hard scatterings in the collision and because their energy is high they do not participate in many rescatterings. They are thus not thermalised nor do they participate in the collective motion. However, an azimuthal anisotropy in particle production is seen also at high p_t [120]. Depending on their orientation with respect to the reaction plane the high p_t particles have to traverse more or less matter in which they lose energy bu medium induced gluon radiation. This path length dependence energy loss also creates an azimuthal anisotropy in the particle momenta. The transverse momentum dependence of v_2 for different particle species is sensitive to the equation of state. This is clearly illustrated in Fig. 4.12. The figure clearly shows that elliptic flow is ordered by the mass of the particles, as is predicted by ideal hydrodynamic calculations: $v_{2,baryon} < v_{2,meson}$. This mass ordering is caused

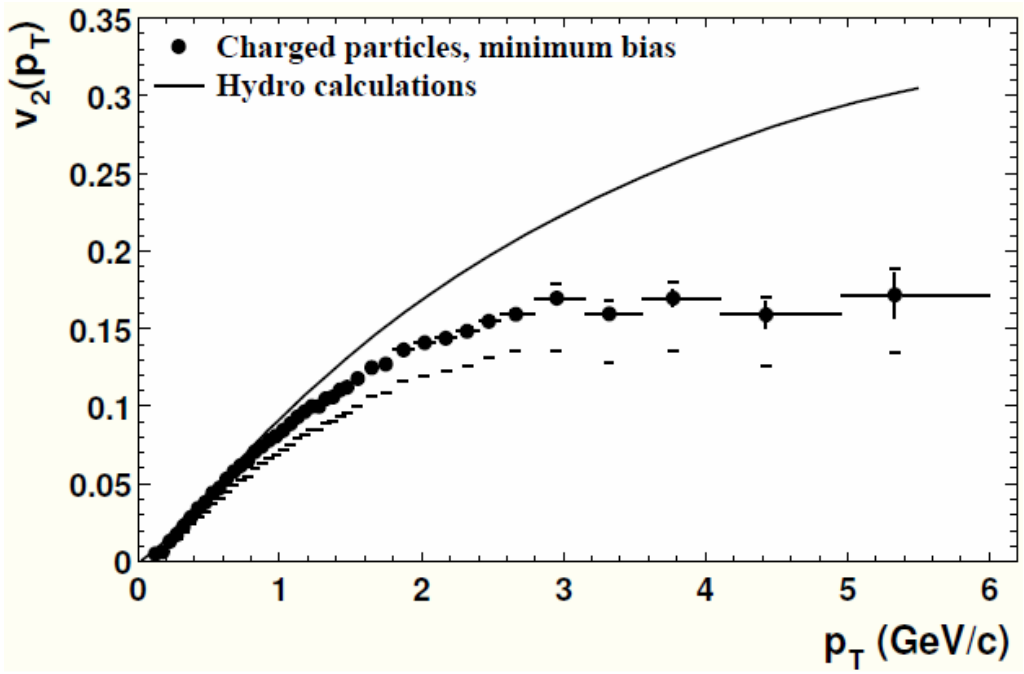

Figure 4.11: *Elliptic flow of charged hadrons as a function of p_T for Au-Au collisions at 130 GeV compared to a hydrodynamic calculation.*

by the presence of radial flow which boosts particles to higher momenta [121]. The momentum gain is larger for heavier particles resulting in a flattening of the transverse momentum spectra of heavy particles. This, in its turn, results in a decrease of v_2 at low p_t and a shift towards higher p_t of the linear rise of $v_2(p_t)$. The effect of the phase transition is more pronounced in the heavier protons because they are more influenced by the collective velocity which is sensitive to the equation of state. At intermediate p_t particle particle production by coalescence or recombination [122, 123] predicts that v_2 depends on the quark content of the particle [124],

$$v_{2,meson}(p_t) \approx 2v_{2,quark}(\frac{p_t}{2}), \tag{4.15}$$

$$v_{2,baryon}(p_t) \approx 3v_{2,quark}(\frac{p_t}{3}) \tag{4.16}$$

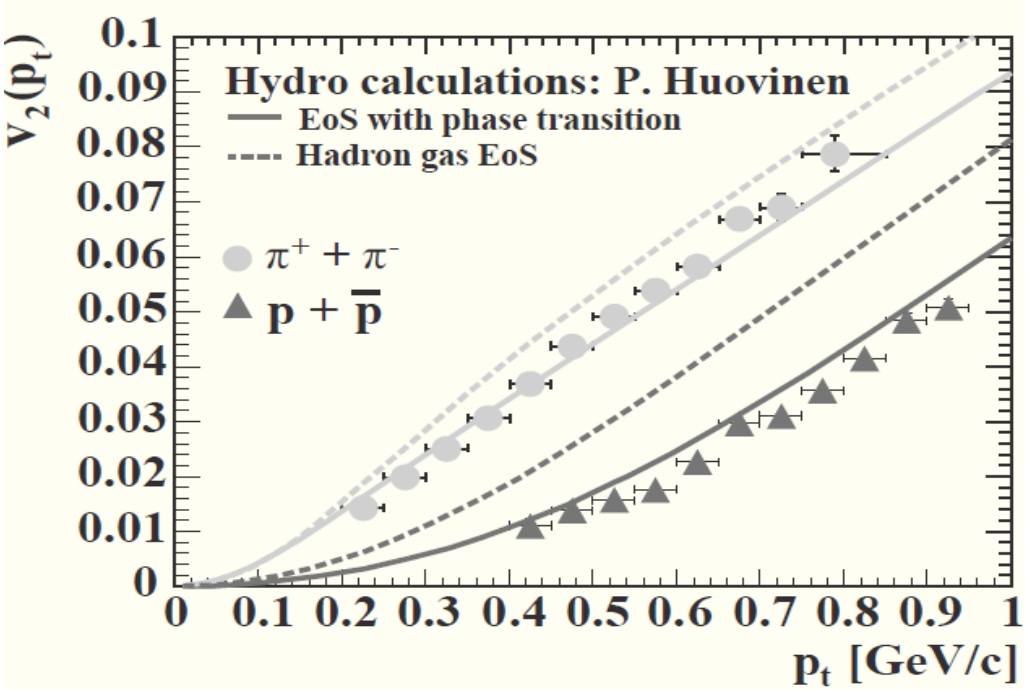

Figure 4.12: *Elliptic flow of pions and protons as a function of p_T for Au-Au collisions at 130 GeV together with two hydrodynamic calculation using different equations of state*

Coalescence depends on the quark degrees of freedom being dominant at hadronisation and results in $v_{2,baryon} > v_{2,meson}$. A scaling of v_2 with the number of constituent quarks versus a scaled p_t should result in all hadrons falling on a universal curve. Fig. 4.13 shows that this is approximately seen in the data which suggests that collectivity developed in the partonic stage of the collision. In the above two equations the assumption is made that all quarks have the same elliptic flow. This may not be the case, strange quarks may have a smaller v_2 than up and down quarks at high p_t because they lose less energy in the medium and at low p_t because of their mass. Such a difference between quarks results in a dependence of v_2 based on the strangeness content of a particle.

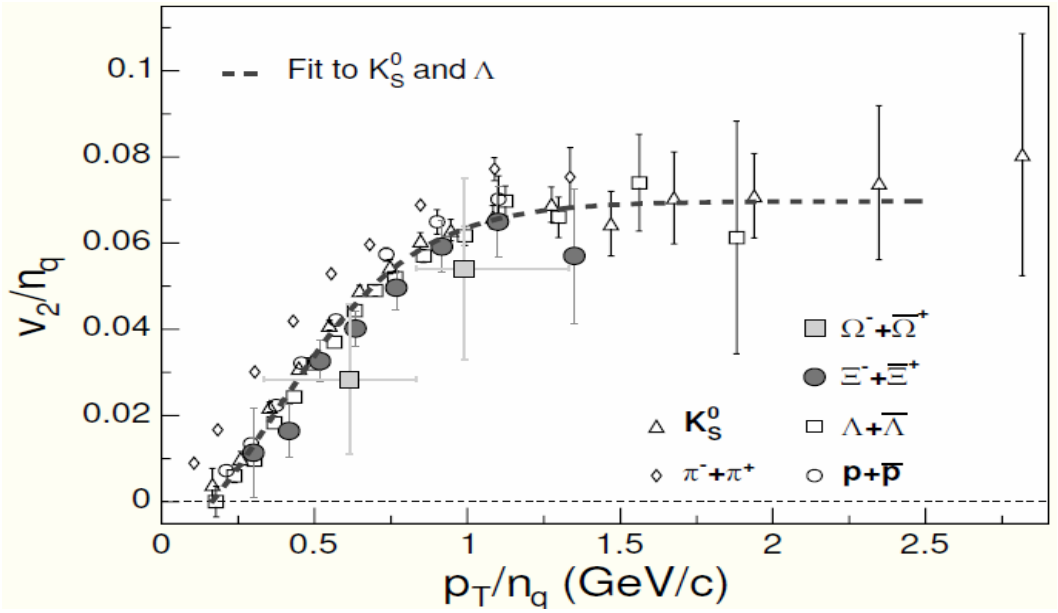

Figure 4.13: *v_2 as a function of p_T both rescaled by the number of quarks n_q for various particle species for Au-Au collisions at 200 GeV.*

4.2.3 Dependence on energy

Fig. 4.14 shows elliptic flow as a function of the centre of mass energy of the collision, $\sqrt{s_{NN}}$, from many different experiments [125]. At low centre of mass energies, below 100 MeV, the collision interaction is dominated by the attractive nuclear mean field. The two nuclei are attracted towards each other and form a rotating system which emits particles in the rotating plane, producing in-plane elliptic flow [126, 127]. At higher energies individual nucleon-nucleon collisions start to dominate, they produce a positive pressure which deflects the projectile and target fragments away from each other. Particles produced in the interaction region cannot escape in the reaction plane due to the presence of the spectator nucleons resulting in squeeze-out [128]. The spectators leave the interaction region after a time of the order $2R/\gamma$, where R is the nuclear radius and γ the Lorentz contraction factor.

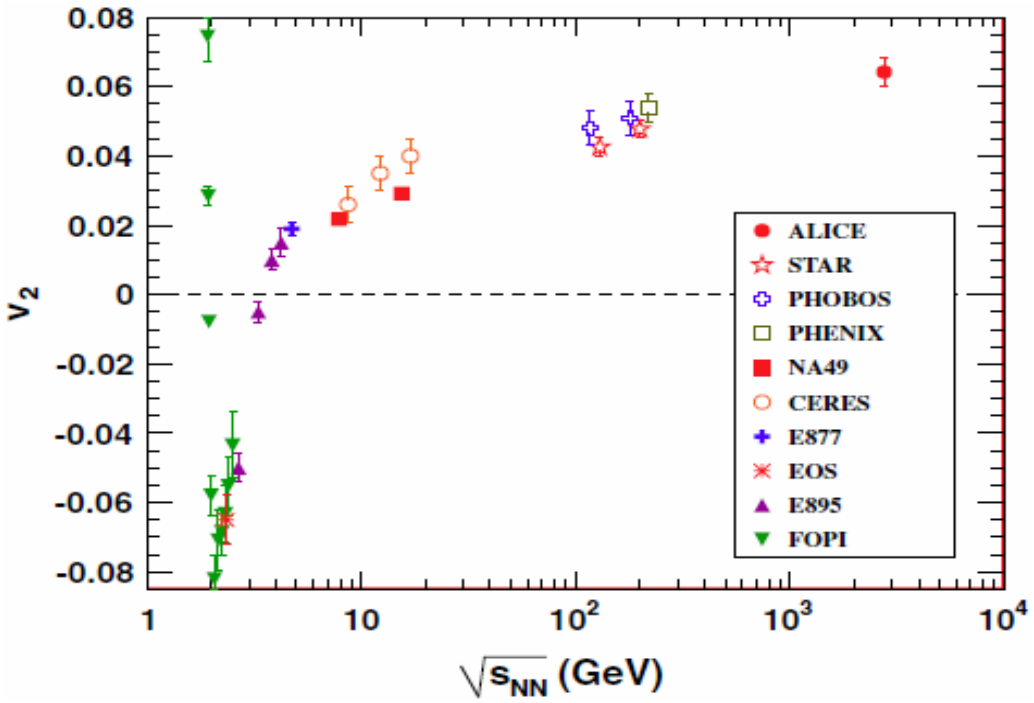

Figure 4.14: *Elliptic flow as a function of the centre of mass energy* $\sqrt{s_{NN}}$ *from many different experiments.*

When the spectators are no longer present, particles are free to move in any direction in the transverse plane. The pressure gradient which is largest in-plane pushes them in this direction producing in-plane elliptic flow. A transition from out of plane, $\langle\cos(2\phi)\rangle < 0$, to in-plane, $\langle\cos(2\phi)\rangle > 0$, occurs when the Lorentz contraction becomes significant. The in-plane elliptic flow increases with the centre of mass energy. At ultra-relativistic energies the nuclei are almost transparent and most of the energy stays in the longitudinal direction. The transverse momenta of produced particles are mostly of the order of a few hundred MeV while the longitudinal momenta are of the order of a few GeV. At such energies the transverse momentum dependence of

elliptic flow is roughly given by,

$$\frac{dv_2(p_t)}{dp_t} \approx \frac{v_2}{\langle pt \rangle}. \tag{4.17}$$

Between the STAR and ALICE experiments $v_2(p_t)$ does not increase, which means that the increase in v_2, of about 30%, is caused by an increase in the mean transverse momentum $\langle p_t \rangle$ of the produced particles. The mean p_t increases because the radial flow does increase with collision energy as a result of the higher initial energy density.

4.2.4 Dependence on eccentricity fluctuations

For spherical nuclei the colliding system is symmetric under reflections with respect to the reaction plane. However, due to fluctuations in the positions of individual nucleons, the distribution of particles in the reaction volume is not strictly symmetric on an event by event basis. Therefore the participant eccentricity is defined from the actual spatial distribution of the participants, the shifted coordinates in Fig. 4.15, and can be different from the geometrical overlap region.

Also the reaction plane from this participant distribution, the participant plane x_{PP}, deviates from the geometrical one, x_{RP}. The size of fluctuations in the geometry can be estimated from the Monte Carlo Glauber calculations. Due to these fluctuations in the spatial eccentricity for a fixed impact parameter, also the elliptic flow v_2 will fluctuate and is given by distribution rather than by a single value. These fluctuations will be most pronounced in very peripheral collisions as the interaction region is small. This has been studied in detail at RHIC [129].

4.3 Flow Methods

Anisotropic flow, which is an anisotropy in the particle production relative to the reaction plane, results in correlations among particles and can be studied by the analysis of these correlations. At the same time these correlations are affected by other effects that are not related to the orientation of the reaction plane. Such are commonly referred to as non-flow,and are due, for example, to resonance decays and jet production. Different methods used to measure anisotropic flow are affected by nonflow effects in different ways and are used in this analysis to evaluate the systematic uncertainty of the measurements.

4.3.1 Event Plane Method with TPC event plane

The event plane method [130] uses the anisotropic flow itself to determine the event plane, which can be done for each harmonic. In principle, the azimuthal distribution of particles through half the range, for $0 < \phi < \pi$, should be the same as the distribution for the other half, $-\pi < \phi < 0 (or \pi < \phi < 2\pi)$. An immediate consequence of this symmetry is that sine contributions will cancel out,

$$\Sigma \sin(\phi_i - \Psi_r) = 0 \tag{4.18}$$

The sum is over all particles. This result is also true for any higher harmonic. The individual terms can be weighted to generalize this condition. Transverse momentum is a typical quantity used for weights. The most general symmetry is:

$$\Sigma w_i \sin n(\phi i - \Psi r) = 0 \tag{4.19}$$

This symmetry can be exploited to estimate the reaction plane.

The second-harmonic flow vector, Q_2, of the event is constructed using the TPC tracks i in the event with their azimuthal angle, ϕ_i, according to

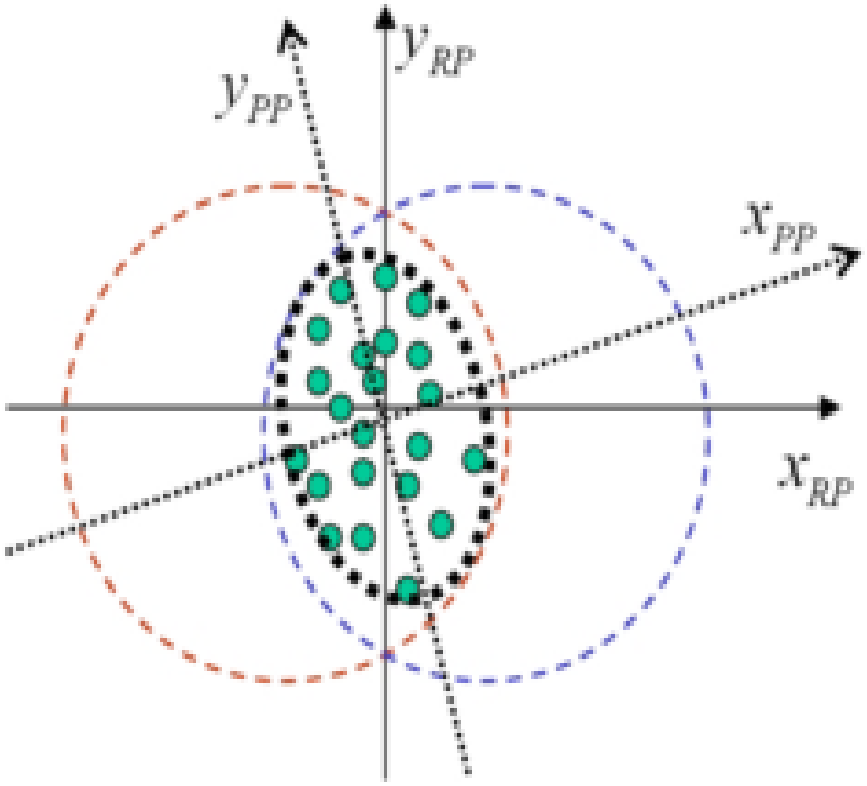

Figure 4.15: *Transverse view of a heavy-ion collision with the reaction plane x_{RP} oriented along the x-axis. Indicated are the participants in the overlap region that randomly define a particpant plane x_{PP} for each collision.*

Eqs. 4.20 and 4.21. To maximize the resolution of the flow effect, the weights w_i are set equal to p_T up to 2GeV/c:

$$Q_2 \cos(2\Psi_2) = Q_{2x} \sum_i w_i \cos(2\phi_i) \tag{4.20}$$

$$Q_2 \sin(2\Psi_2) = Q_{2y} \sum_i w_i \sin(2\phi_i) \tag{4.21}$$

Finally, the reaction plane can be determined:

$$\Psi_2 = (\tan^{-1} \frac{\sum_i w_i \sin 2\phi_i}{\sum_i w_i \cos 2\phi_i})/2 \tag{4.22}$$

Weights for even and odd harmonics are usually different. For a symmetric collision in which the projectile and target are the same, there is another geometric symmetry. The particle azimuthal emission pattern in the forward region (rapidity greater than center of mass rapidity), should be identical to the emission pattern in the backward region if the azimuthal angles of these particles are shifted by π. For odd harmonics, this produces a second symmetry condition, $\Sigma \cos n(\phi_i - \Psi_r) = 0$, making the preceding derivation invalid. By weighting the backward particles by a factor $(-1)^n$, the original symmetry is unaffected, and this new condition is no longer true. Thus, the backward particles in odd harmonics are weighted by an additional factor of (-1).

Elliptic flow is first calculated with respect to the event plane angle Ψ_2 as shown in eqn 4.23, which is called the observed v_2. However, tracks used for the v_2 calculation are excluded from the calculation of the flow vector to remove autocorrelation effects. Then the observed v_2 is corrected by the event plane resolution (the denominator in eqn. 4.24) to obtain v_2 relative to the event plane:

$$v_2^{obs} = \langle \cos 2(\phi - \Psi_2) \rangle \tag{4.23}$$

$$v_2 = \frac{v_2^{obs}}{\langle \cos(2(\Psi_2 - \Psi_r) \rangle} \tag{4.24}$$

The results are denoted as $v_2(TPC)$ here. Because the reaction plane is unknown,the denominator in eqn. 4.24 is still not calculable. As shown in eq. 4.25, we estimate the event plane resolution by the correlations between the azimuthal angles of two subset groups of tracks, called subevents A and B. In eqn. 4.25, C is a constant calculated from the known multiplicity dependence of the resolution.:

$$\langle \cos[2(\Psi_2 - \Psi_r)] \rangle = C \sqrt{\langle \cos[2(\Psi_2^A - \Psi_2^B)] \rangle} \tag{4.25}$$

In the case of low resolution (≤ 0.2), such as for the FTPC event plane, C approaches $\sqrt{2}$. The reaction plane azimuthal distribution should be isotropic in the laboratory frame. Thus, the event plane azimuthal distribution must be flat if the detectors have ideal acceptance. For the event plane reconstructed from TPC tracks, the ϕ weight method is an effective way to flatten the distribution.

4.3.2 Event Plane Method with FTPC event plane

The η gap between two FTPCs sitting at two sides of the collision in the forward regions can be used to reduce non-flow effects due to short-range correlations. Here are three steps: estimate the event plane with FTPC tracks, calculate v_2 with respect to the event plane, and obtain the real v_2 by correction to the real reaction plane. Eqs. 4.20-4.25 can be applied, except that: i) the sums in eqn. 4.20 and eqn. 4.21 go over FTPC tracks instead of TPC tracks, and ii) two subset groups of tracks are classified according to the sign of η. The tracks with $-4 < \eta < -2.5$ and $2.5 < \eta < 4$ are called East subevent and West subevent, respectively. Hence, the resolution in eqn. 4.25 is calculated by the correlation between the azimuthal angles Ψ_2^{east} and Ψ_2^{west}. The average in eqn. 4.23 runs over the TPC tracks as before. The result of this procedure is denoted as $v_2(FTPC)$.

Due to the serious loss of acceptance for FTPCs due to partially non-functioning readout electronics, the number of tracks detected by the best sector is about 6 times greater than for the worst one. The result is that the ϕ weight method is not enough to generate a flat event plane distribution. Thus, further small corrections are applied after ϕ weight corrections using the shift method [131]. Eqn. 4.26 shows the formula for the shift correction.

The averages in eqn. 4.26 are taken from a large sample of events.

$$\Psi^{'} = \Psi + \sum_{i} \frac{1}{n}(-\langle \sin(2n\Psi) \rangle) \cos(2n\Psi) + \langle \cos(2n\Psi) \rangle \sin(2n\Psi) \qquad (4.26)$$

4.3.3 Scalar Product Method

The Scalar Product Method [132] is applied to the v_2 measurement of charged hadrons and is similar to the Event Plane Method. It gives v_2 as:

$$v_2(p_T) = \frac{\langle Q_2 u^*_{2,i}(p_T) \rangle}{2\sqrt{\langle Q_2^A Q_2^{B*} \rangle}} \qquad (4.27)$$

where $u_{2,i} = \cos(2\phi_i) + i\sin(2\phi_i)$ is a unit vector of the ith particle, $Q_2 = \Sigma_k u_{2,k}$ is the flow vector with the sum running over all other particles k in the event. The superscript $*$ denotes the complex conjugate of a complex number. A and B denote the two subevents. In the case that Q_2 is normalized to a unit vector, eqn. 4.27 reduces to the Event Plane method. In the Scalar Product method, one can use a different (re-centering) technique [133] to correct for detector effects, which presents an alternative to the weighting and shifting procedures described above.

4.3.4 v_2 versus m_{inv} method

For v_2 of the identified particles K^0_s, ϕ, λ and Ξ, the v_2 versus m_{inv} method is used [134, 135]. Since v_2 is additive, one can write the total v_2^{Sig+Bg} as a sum of signal and background contributions weighted by their relative yields:

$$v_2^{Sig+Bg}(m_{inv}) = v_2^{Sig} \frac{Sig}{Sig+Bg}(m_{inv}) + v_2^{Bg}(m_{inv}) \frac{Bg}{Sig+Bg}(m_{inv}) \qquad (4.28)$$

This method involves the calculation of v_2^{Sig+Bg} as a function of m_{inv} and then fitting the distribution using eqn. 4.28 with measured relative yields and parameterizations of v_2^{Sig} and v_2^{Bg}. The $(Bg/Sig+Bg)(m_{inv})$ distribution

is the Bg divided by (Sig+Bg). The $(Sig/Sig+Bg)(m_{inv})$ distribution is simply calculated by $1-(Bg/Sig+Bg)(m_{inv})$. The term v_2^{Bg} is parameterized as a linear function in order to take care of the non- constant v_2^{Bg} value as a function of m_{inv}. The fit result v_2^{Sig} is the final observed v_2. This method works well because a set of data points is used in the fit over a wide m_{inv} mass region for Sig and Bg. Data points far from the mass peak constrain $v_2^{Bg}(m_{inv})$, since pure Bg is expected in this region. Under the peak, the $v_2^{Sig+Bg}(m_{inv})$ is dominated by the Sig distribution. Finally, the v_2 signal is extracted by the fitting method shown in eqn. 4.28.

4.4 "Flow" at recent RHIC Experiments

Recently, two important insights have been obtained from the experimental results on v_2 as a function of transverse momentum, p_T, in Au+Au collisions at the BNL Relativistic Heavy Ion Collider (RHIC). First, in the low p_T region, $p_T < 2GeV/c$, the hadron mass hierarchy predicted by ideal hydrodynamic calculations is observed for identified hadrons π, K , K_s^o, p, λ, and Ξ [136, 137, 138, 139, 140]. Even the ϕ and Ω, which are believed to have a reduced cross section for hadronic interactions [141, 142, 143, 144, 145, 146, 147, 148], are consistent with the mass ordering [149, 150]. Second, in the intermediate p_T region, $2 < p_T < 4GeV/c$, $v_2(p_T)$ follows a scaling depending on the number of constituent quarks within a given hadron,which can be explained via coalescence models [151]. Quark number scaling suggests that the system is in a partonic state and that the constituent quark degrees of freedom were relevant during the time v_2 was developed [152, 153, 154, 155].

The STAR Collaborations' first published article showed that elliptic flow at RHIC is unexpectedly large [156], comparable to predictions of ideal hy-

drodynamic calculations [157, 158]. This observation is among the evidence favoring the picture of a nearly perfect liquid [159]. With the assumption of thermalization, ideal hydrodynamic calculations predict that the v_2 divided by spatial eccentricity, ε_s, does not depend on the collision centrality [160]. However, recent RHIC v_2/ε data for charged hadrons $h^{\pm}$ and strangeness-containing hadrons K^o_s, ϕ, λ, and Ξ show a trend to increase as a function of the particle density scaled by the system-size), lacking the saturation indicated by ideal hydrodynamic calculations. This monotonic increase is a feature of a class of model descriptions that conform to the low-density limit. Whether the thermalization and ideal hydrodynamic limit are reached or not at RHIC is not conclusive. A transport model suggested in [161] is constructed to link the low-density limit to the ideal hydrodynamic limit. In the microscopic transport picture, the ideal hydrodynamic limit is reached when the mean free path is very small or the cross section is very large. With this transport model approach, the degree of thermalization and the ideal hydrodynamic limit can be addressed.

Chapter 5

Results and conclusion

5.1 Introduction

The development of the simulation and analysis framework for the CBM Experiment started at the end of 2003. The framework is completely ROOT based. The CBMRoot simulation framework [162] has been developed for feasibility studies and optimization of the detector layout. The modified HADES geometry interface used in this framework enables the user to select (on the fly) between the new ROOT Geometry Modeler and the Geant3 native geometry to describe the detectors. The simulation is based on the Virtual Monte Carlo concept, which was developed by the ALICE collaboration and allows to select different engines (Geant3, Geant4, Fluka)for the transport of tracks. Moreover the analysis is organized using the ROOT Task mechanism. The CBM experiment will collide heavy ions in the momentum range from 10A to 45A GeV ($Z/A = 0.5$) at 10 MHz interaction rate for rare probes. This means that tracking algorithms have to be not only efficient but also very fast in order to allow online event selection.

Now let us discuss some of the event generators and the GEANT software

package used for simulation studies.

5.1.1 The UrQMD event generator

The UrQMD code is the main part of the event generation in high energy simulation. It is designed to cover the best possibilities of microscopic transport theoretical calculations in the energy range between 100 MeV/A and 200 GeV/A. At (1-10 GeV) energies, all baryonic resonances up to an invariant mass of 2.25 GeV as well as mesonic resonances up to 1.95 GeV, as tabulated by the Particle Data Group, are taken into account. Now let us note some of its key features:

• UrQMD is a microscopic transport code providing a full hadronic simulation of the reaction dynamics based on elementary reactions. Particles are propagated for an optional time and may undergo collisions with other particles or change their direction due to interaction with external fields.

With the coupling of particles to the fields of the environment in-medium effects can be explored.

• Strong interactions are simulated. The included interaction cross sections are tuned to reproduce experimental data or are motivated from theory (e.g., detailed balance).

UrQMD also includes surface terms of the interacting volume. Electromagnetic fields are taken into account for particle propagation.

• Nucleons are modeled with Fermi motion.

• UrQMD is a cascade-like model: Apart from string excitation and string fragmentation a big part of the reaction dynamics is modeled via the excitation, propagation and decay of hadronic resonances.

The highly excited baryons have not been measured with high precision yet. In UrQMD the branching ratios for these cases are always inside the ex-

perimental limits [163], but tuned to measured production rates of secondary particles.

• UrQMD includes strange particles but no vector mesons and charmed particles, therefore we implement their multiplicities using the HSD model.

• UrQMD does not include any leptons. Neither semi-leptonic decays nor leptonic particles are implemented.

5.1.2 PLUTO

Pluto is also a Monte-Carlo event generator designed for hadronic interactions from Pion production threshold to intermediate energies of a few GeV per nucleon, as well as for studies of heavy ion reactions. The package is entirely based on ROOT, without the need of additional packages, and uses the embedded C++ interpreter of ROOT to control the event production. Vector mesons decaying into dileptons are embedded using the PLUTO generator which in particular provides correct decay kinematics of the hadronic and electromagnetic decays. The generation of events based on a single reaction chain and the storage of the resulting particle objects can be done with a few lines of a ROOT-macro. However, the complete control of the package can be taken over by the steering macro and user-defined models may be added without a recompilation of the framework. Multi-reaction cocktails can be facilitated as well using either mass-dependent or user-defined static branching ratios.

The included physics uses resonance production with mass-dependent Breit-Wigner sampling. The calculation of partial and total widths for resonances producing unstable particles is performed recursively in a coupled-channel approach The thermal model supports 2-component thermal distributions, longitudinal broadening, radial blast, direct and elliptic flow, and

impact-parameter sampled multiplicities.

5.1.3 GEANT and the simulation procedure

GEANT is one of the important particle transport Monte-Carlo engines. A Virtual Monte Carlo concept allows to perform simulations using different transport codes such as GEANT3, GEANT4, or Fluka without changing the user code.The Virtual Monte-Carlo (VMC) interface of ROOT (TGeoManager) can be used to interface different particle transport Monte-Carlo engines like Geant3 and Geant4 with ROOT. This allows to use the same analysis code and geometry definition with the different engines.

FairRoot delivers base classes which enable the users to construct their detectors and/or analysis tasks in a simple way. Moreover an interface for reading magnetic field maps is also implemented. The storage of all information collected by the different sensitive detectors is done on an event by event basis (an event means in this context one interaction between a beam ion and the target). All relevant objects are stored into binary ROOT files. An interface class (CbmMCPoint) is provided to define the structure of registered hits in a detector. All registered hits will be collected into dedicated lists, one list corresponding to one detector entity. The ROOT class TTree is used to organise the output data into a "ntuple like" data structure. For the related data analysis, the CbmRootManager provides methods to read this information.

The event reconstruction and analysis software is organised in so-called tasks. The CbmTask is an abstract class which can be used to create specialised algorithms inheriting from it. For each event, various tasks or reconstruction algorithms are created. Each task defines the relevant input data and parameters and creates its particular output data. The relevant input

data and parameters are retrieved from the input file and the output data objects are stored in the output file. The first step consists in the generation of the particles entering a detector. Those are composed from three dominant contributions which are: the nuclear collision particles, the π^+, K^- pairs coming from a D^0 decay (Thermal model) and the δ-electrons generated inside the target by the passage of beam particles in the target (noted as "beam particles"). The term "event" corresponds to one UrQMD collision in which may be embedded the D^0 decay particles. The thermal model and the UrQMD generators create different output files. The thermal model generates one file containing only signal particles. The UrQMD model is used to create two independent files: one containing only central collisions and one containing minimum bias collisions (any impact parameter). By doing so, it is easier to overlap collisions in order to simulate collision pile up. The signal pairs are embedded only in the central collisions (one pair per collision). The "beam particles" generator is generating ions (e.g., Au ions) which are then directly injected in the GEANT simulation. The interaction of the beam particles with the target generate the δ-electrons. Note that the δ-electrons are also saved in a separate file.

The generated particles are then processed by the GEANT3 simulation package to add the detector effects. GEANT3 allows simulating the behaviour of particles as they interact with the different detector elements and physical structures of the experiment. The output data type (MCPoints) provides the position, the type and the momentum of the particles impinging each detector.

The next step is to simulate the response of each sub-detector including its subsequent electronics (e.g., the number of firing pads, the detector inefficiencies, electronic noise, etc.). The detector response models use as input

the data stored in the MC Point object and provide the number of fired pads (pixels or strips), their pulse height and their position on the detector. The output data type is called Digi. Afterwards, specific algorithms for the reconstruction of the particle impact position (hits) are used. Once the hits are reconstructed, then the track reconstruction takes place; this consists of the track finding and the track fitting procedures. The former associates the hits to a track and the latter performs a fit of the tracks in order to extract the track parameters, e.g., the particle momentum. Finally, the tracks are used for the primary and secondary vertex reconstruction and then the physics analysis may take place.

5.2 Simulation and discussion

The data used for analysis is categorized into following parts:

1. Signal (J/ψ meson) data (1 K) at 10, 25 and 35A GeV.

2. Background particle data (1 K) at 10, 25 and 35A GeV.

3. Background and Signal (embedded) data.

The PLUTO event generator generates the signal particles such as J/ψ, low mass vector mesons as ρ, ω and ϕ and their decay into muon pairs. The background particles ($\pi^{\pm}$, $k^{\pm} \rightarrow \mu$ decays) in central $Au^{197} + Au^{197}$ collisions are generated by using the UrQMD generator. The signal particles are merged into the background particles for embedded events. For simulation, the STS detector of 8 stations and the standard geometry for MUCH have been used.

After getting the plots of pseudorapidity, azimuthal angle and pseudorapidity-azimuthal angle distribution from the simulation, these have been compared for the three energies. The plots show the azimuthal, pseudorapidity

and the azimuthal-pseudorapidity distribution of the embedded monte-carlo data for the 10A GeV, 25A GeV and 35A GeV energies.

We know that in heavy-ion collisions when the nuclei collide many particles are produced and are emitted from the collision zone. The more the energy of the colliding nuclei, the more the number of the particles produced and hence emitted. At lower energies, the colliding nuclei leave the collision zone less quickly compared to that of the higher energies; due to which the spectator matter blocks the emission of particles in the impact parameter direction, thus the emission of particles takes place in the transverse direction i.e., perpendicular to the beam direction. This gives rise to the elliptic flow and is true for non-central collisions with impact parameter non-zero. But for central collisions the emission of particles takes place symmetrically in the azimuthal plane and hence the elliptic flow coefficient is zero which represents the anisotropy of the particle emission with respect to the azimuthal plane. The theory also predicts the elliptic flow coefficient to be zero for central collisions.

From the azimuthal angle distribution plots of the three energies it is clearly seen that the number of entries is largest for 35A GeV energy while the number is least for 10A GeV. Now we know that the CBM detector accepts charged particles emitted at polar angles between 2.5° to 25° in the laboratory; this geometrical acceptance corresponds to a pseudorapidity window of $\Delta\eta = 2.31$ (η between 3.82 and 1.51) . From the $\eta - \phi$ distribution it is seen that among the three energies the number of entries within the CBM acceptance region is largest for 35 A GeV and the number is least for 10A GeV. Hence the loss is most in the 10A GeV case while it is least for 35 A GeV. Hence the detection efficiency for the CBM Experiment is more for 35A GeV compared to that of both 10A GeV and 25A GeV.

Now using the concept of azimuthal angle ϕ, the ϕ plots indirectly show the vanishing of elliptic flow coefficient. As for the simulation, central collisions (with impact parameter zero) have been considered, so the azimuthal plots of the three energies do not show much change in the number of emitted particles with the changing azimuthal angle. Therefore, there is almost an isotropic distribution of the particles. That means the particles are emitted symmetrically with respect to the azimuthal plane ; hence indirectly we may say that the elliptic flow coefficient is zero for the Au+Au central collisions considered here.

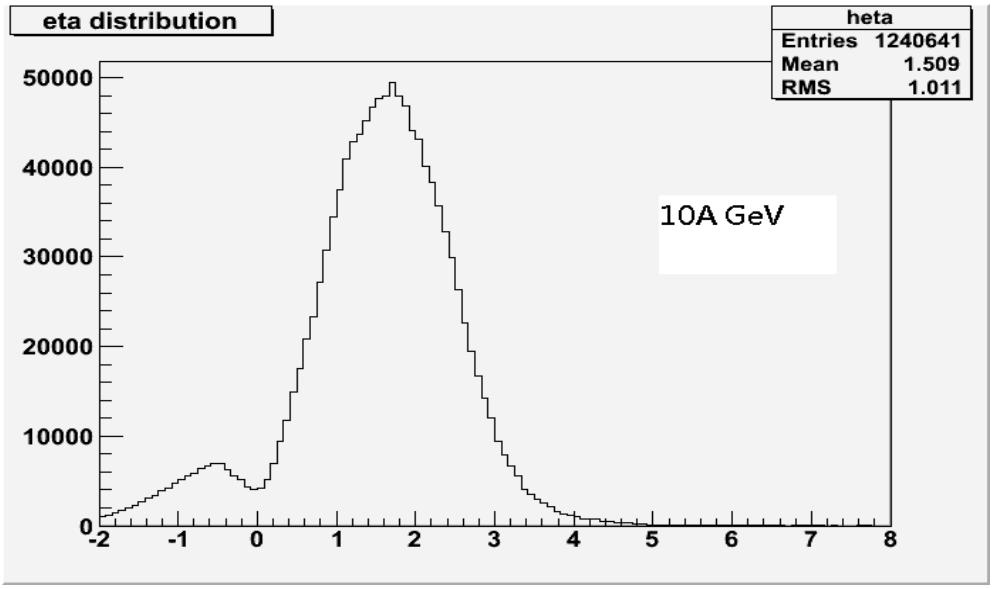

Figure 5.1: *The eta distribution of the simulated mc data for 10A GeV.*

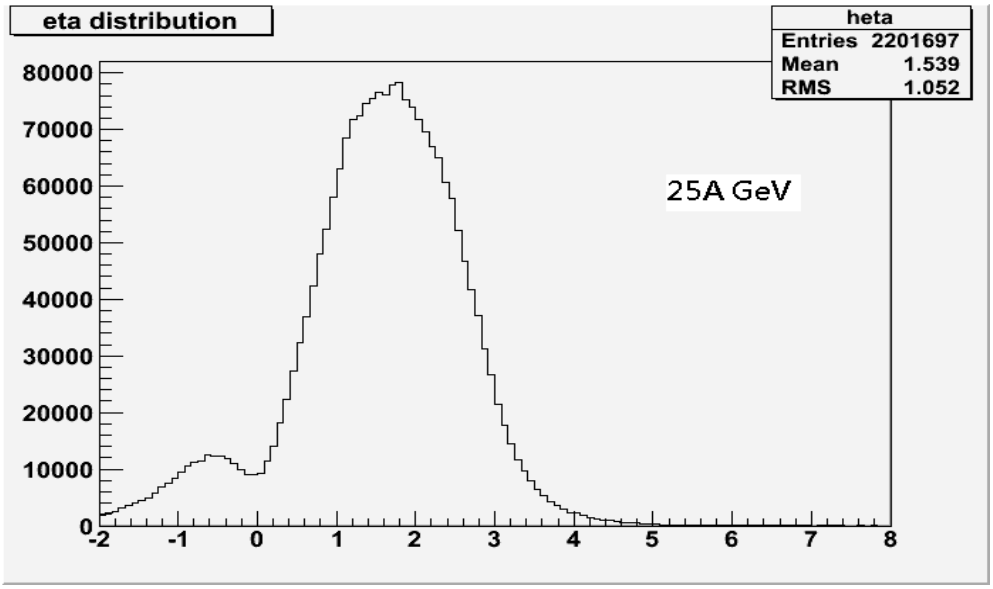

Figure 5.2: *The eta distribution of the mc data for 25A GeV.*

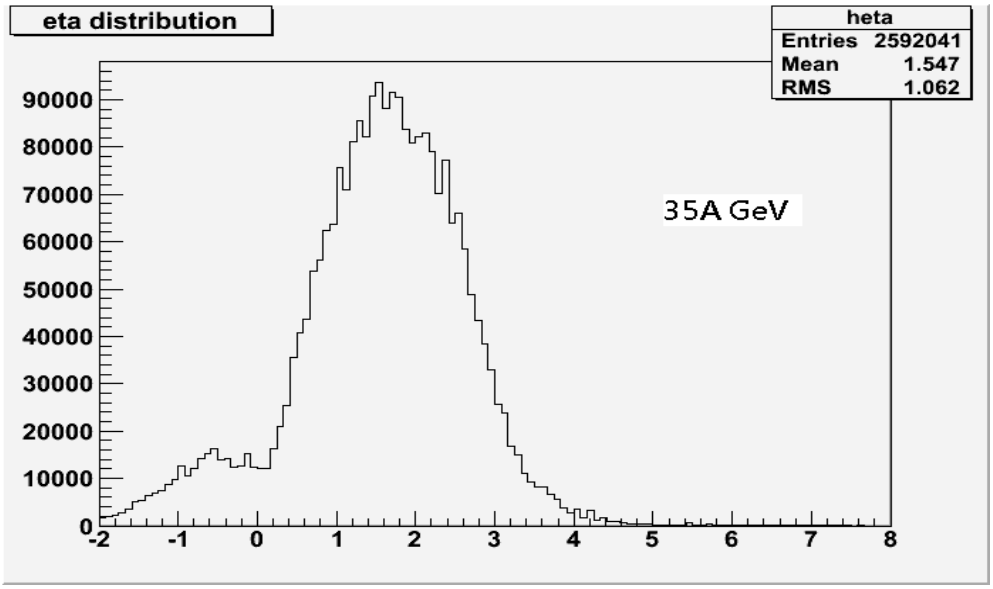

Figure 5.3: *The eta distribution of the mc data for 35A GeV.*

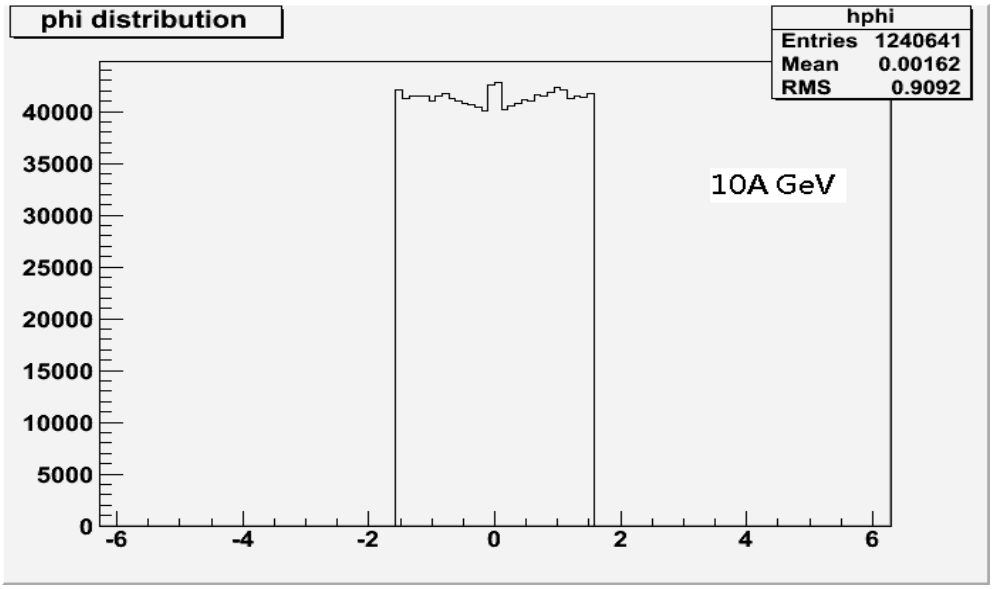

Figure 5.4: *The phi distribution for 10A GeV.*

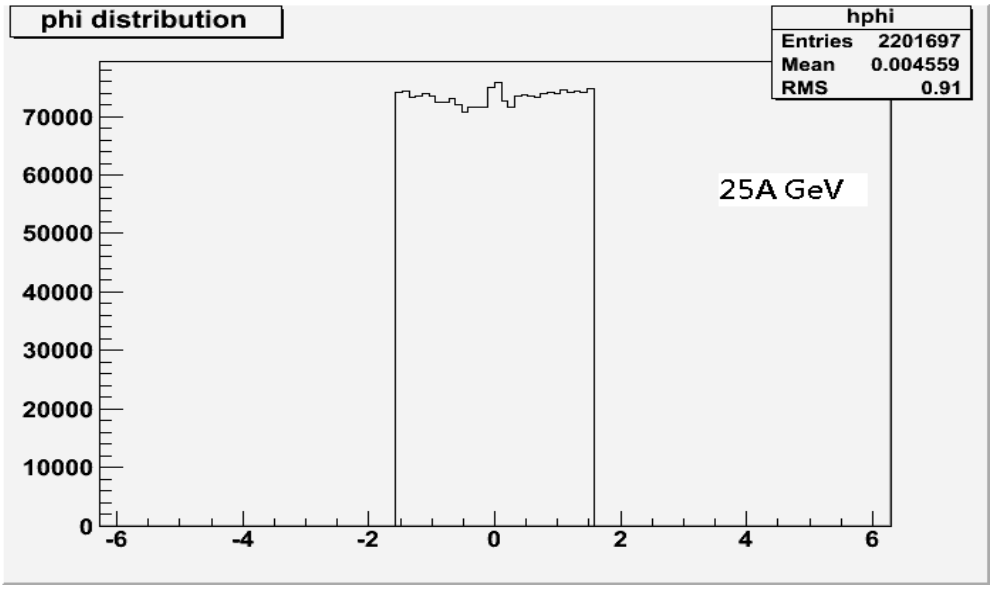

Figure 5.5: *The phi distribution for 25A GeV.*

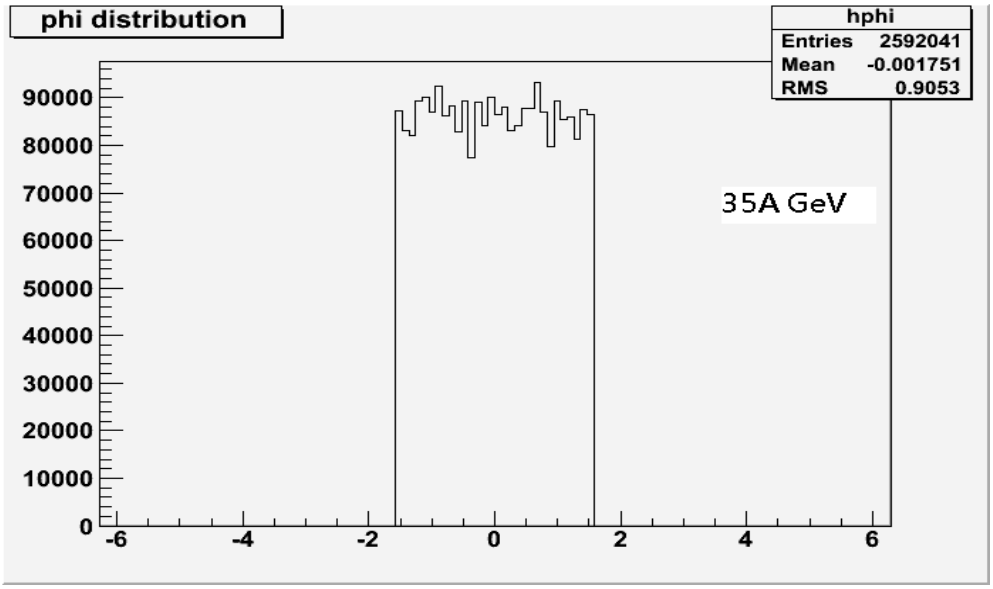

Figure 5.6: *The phi distribution for 35A GeV.*

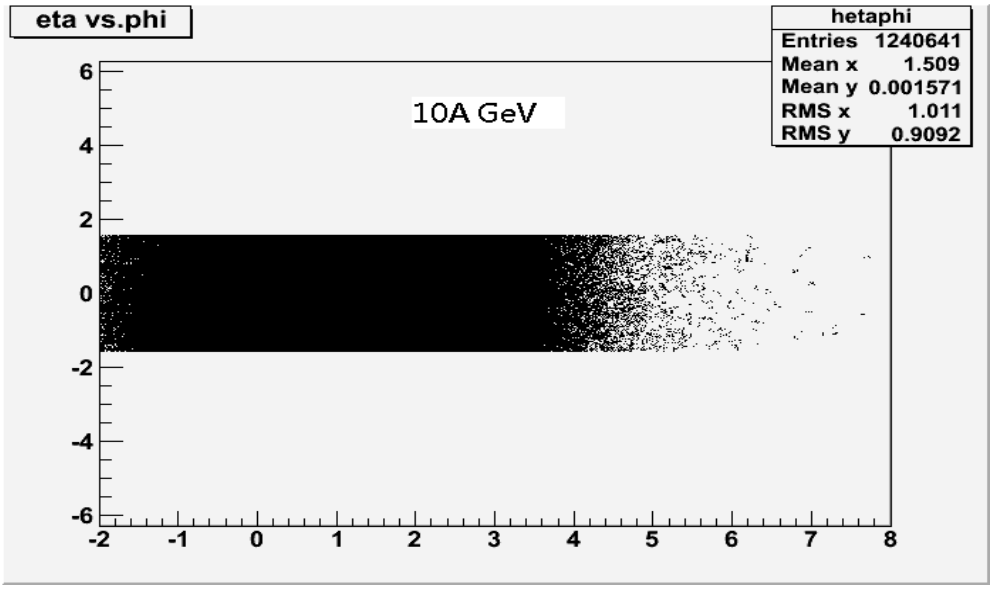

Figure 5.7: *The eta-phi distribution for 10A GeV.*

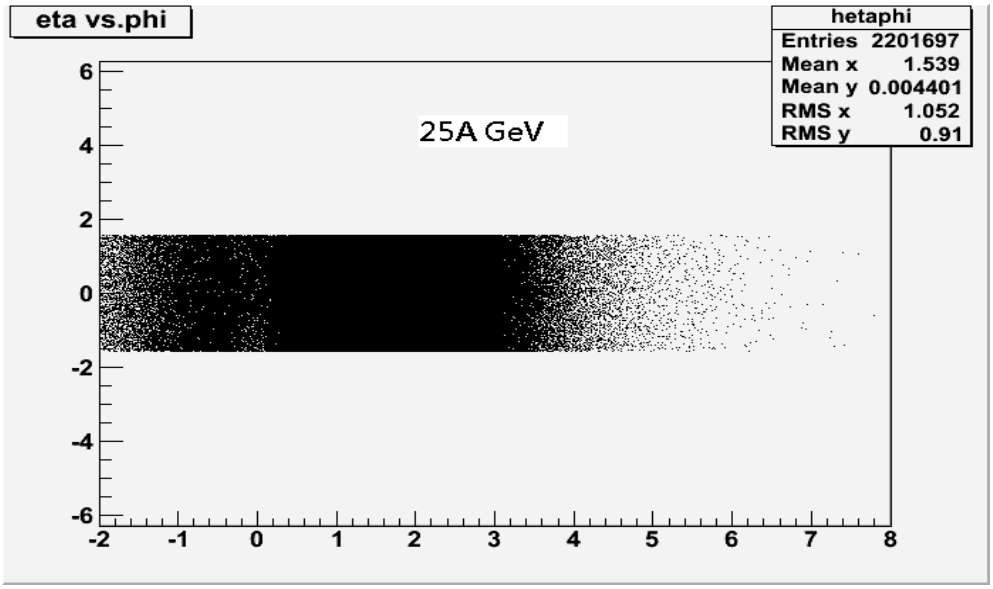

Figure 5.8: *The eta-phi distribution for 25A GeV.*

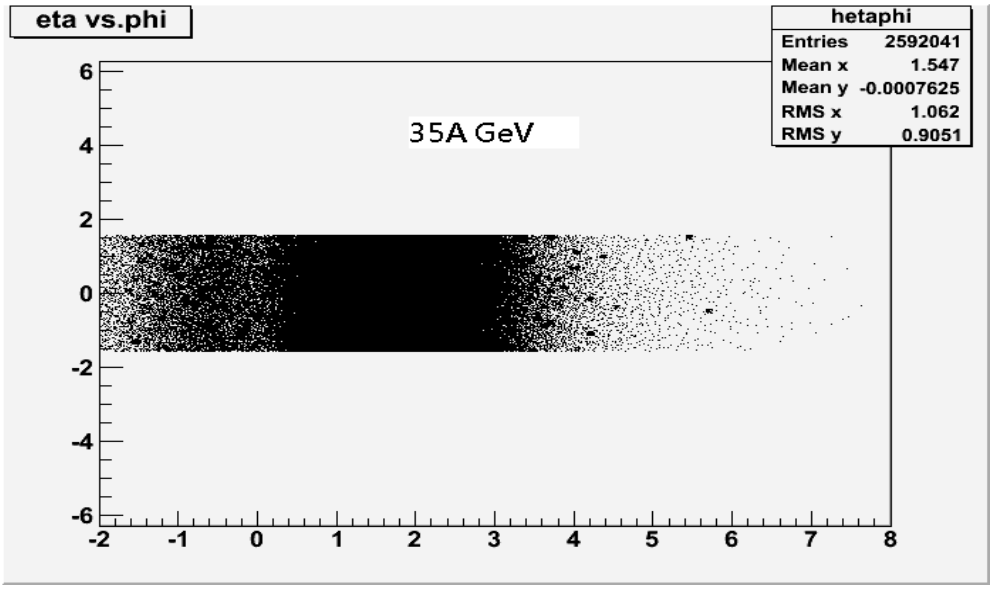

Figure 5.9: *The eta-phi distribution for 35A GeV.*

5.2.1 Conclusion

In August, 2012 the ALICE Collaboration published data about the elliptic flow of J/ψ at very high energies (2.76 TeV) [164] in which they showed that the elliptic flow coefficient of J/ψ tends to vanish for central collisions. They have compared their data with the STAR Experiments which also shows the vanishing of the elliptic flow coefficient in central collisions.

From the simulation studies, one can conclude that the number of entries is largest for 35A GeV energy while the number is least for 10A GeV, and the number of entries within the CBM acceptance region is largest for 35 A GeV and again the number is least for 10A GeV. Besides, the azimuthal plots of the three energies do not show much change in the number of emitted particles with the changing azimuthal angle. Therefore, there is almost an isotropic distribution of the particles; hence indirectly one can say that the elliptic flow coefficient is zero for the Au+Au central collisions considered here.

Bibliography

[1] D. H. Perkins, *Introduction to High Energy Physics*, 4th Ed. (2000).

[2] S. Gasiorowicz and P. Langacker, *Elementary Particle Physics*, Wiley (1966).

[3] F. Halzen and A. D. Martin, *Quarks and Leptons: An Introductory Course in Modern Particle Physics*, Wiley (1984).

[4] F. J. Yndurain, *Quantum Chromodynamics: An Introduction to the Theory of Quarks and Gluons*, Springer-Verlag (1983).

[5] W. Greiner, E. Stein, and S. Schram, *Quantum Chromodynamics*, Springer (2005).

[6] D. J. Griffiths, *Introduction to Elementary Particles*, John Wiley and Sons (1987).

[7] B. B. Back et al, Nucl. Phys. **A757**, 28 (2005).

[8] F. Karsch, Nucl. Phys. **A698**, 199c (2002).

[9] K. Rajagopal, Acta Phys. Polon. **B31**, [hep-ph/0009058] 3021 (2000).

[10] S. Salur, *Investigation of Hadronic Resonances with STAR*, Disseration Thesis, Yale (2006).

[11] C. Y. Wong, *Introduction to High Energy Heavy-Ion Collisions*, World Scientific, (1994).

[12] K. Higashijima, Phys. Rev. **D29**, 1228-1232 (1984).

[13] H. Pagels, Phys. Rev. **D19**, 3080-3090 (1979).

[14] K. Schweda, X. Zhu, M. Bleicher, S. L. Huang, H. Stocker, N. Xu, P. Zhuang, arXiv:nucl-ex/0610043 v1 **30**, Oct (2006).

[15] S. Soff, Phys. Lett **B471**, 8996 (1999).

[16] M. C. Abreu et al, Phys. Lett. **B**, 2836 (2000).

[17] J. Adams et al, Phys. Rev. **C68**, 044905 (2003).

[18] T. Wienold, N. Herrmann and J Wessels, Annu. Rev. Nucl. Part. Sci. **49**, 581-632 (1999).

[19] W. Reisdorf and H. G. Ritter, Annu. Rev. Nucl. Part. Sci., **47**, 663-709 (1997).

[20] P. Kolb, P. Huovinen, U. Heinz and H. Heiselberg, Phys. Lett. **B500**, 232-240 (2001).

[21] *Facility for Antiproton and Ion Research*, http://www.fair-center.de.

[22] *FAIR Conceptual Design Report*, Darmstadt (2001).

[23] *FAIR Baseline Technical Report*, ISBN 3-9811298-0-6, Darmstadt (2006).

[24] P. Senger, *The CBM experiment at FAIR*, presentation given at Gauhati University, Guwahati, India (March 4, 2011).

[25] J. Adams, et al, Phys. Rev. Lett. **93**, 252301 (2004).

[26] J. M. Heuser, et al, AIP Conf. Proc. **842**, 1073 (2006).

[27] J. M. Heuser, et al, Czech. J.Phys. **55**, 1649 (2005).

[28] J. M. Heuser, et al, Nucl. Instr. Meth. Phys. Res. **A568**, 258 (2006).

[29] I. Kisel, Nucl. Instrum. Meth. Phys. **A566**, 85 (2006).

[30] A. Lebedev, G. Ososkov, *LIT Track Propagation for CBM*, CBM note http://www.gsi.de/documents/DOC-2008-Dec-182-1.pdf (2008).

[31] W. Cassing, E. Bratkovskaya, A. Sibirtsev, Nucl. Phys. **A691**, 745 (2001).

[32] M. Deveaux, *Development of fast and radiation hard MAPS optimized for the CBM-vertex detector*, Ph.D Thesis, Strasbourg (2008).

[33] M. Deveaux et al, arxiv : 0906.1301 [nucl-ex].

[34] S. Lebedev, *Algorithms and Software for Event Reconstruction in the RICH, TRD and MUCH detectors of the CBM experiment*

[35] A. Andronic, Nucl. Instrum. Meth. **A563**, 349 (2006).

[36] A. Kozhevnikov et al, Nucl. Instr. and Meth. **A433**, (1999).

[37] D. Kresan and C. Hohne, CBM Progress Report (2008, 2009).

[38] A. Dubey et al, CBM Progress Report (2007, 2008).

[39] M. Al-Turany and F. Uhlig, PoS **ACAT08**, 048 (2008).

[40] D. Bertini et al, J. Phys. Conf. Ser. **119**, 032011 (2008)

[41] V. Friese, *The CBM experiment at FAIR*, PoS **CPOD07**, 056 (2007).

[42] P. Senger, PoS **CPOD2009**, 042 (2009)

[43] V. Friese, J. Phys. **G37**, 094025 (2010).

[44] R. Fruhwirth, Nucl. Instrum. Meth **A262**, 444-450 (1987).

[45] C. Amsler et al, Physics Letters **B667**, 1 (2008).

[46] S. A. Bass et al, Prog. Part. Nucl.Phys. **41**, 225-370 (1998).

[47] A. Fontana et al, *Track following in dense media and inhomogeneous magnetic fields*, PANDA Report PV/01-07 (2007).

[48] S. Gorbunov and I. Kisel, *An analytic formula for track extrapolation in an inhomogeneous magnetic field*, CBM-SOFT-note-2005-001 (2005).

[49] P. Fonte, A. Smirnitski, M.C.S. Williams, Nucl. Instr. & Meth. **A443**, 201 (2000).

[50] A. Akindinov, P. Fonte, P. Formenti, et al., IEEE Trans. Nucl. Sci. **48**, 1658 (2001).

[51] A. Akindinov, F. Anselmo, M. Basile, et al., Nucl. Instr. & Meth. **A456**, 16 (2000).

[52] M. Bogomilov, D. Dedovich, R. Dumps, et al., Nucl. Instr. & Meth. **A508**, 152 (2003).

[53] V. V. Parhomchuk et al., Nucl. Instrum. & Methods, **93**, 269 (1971).

[54] B. Santonico et al, Instrum. & Methods, **187**, 377 (1981).

[55] M. Kagarlis, http://www-hades.gsi.de/computing/pluto 859, 875.

[56] I. Frohlich et al, PoS **ACAT2007**, 076 (2007).

[57] L. Michela, Nucl. Instru. Meth. Phys. Rs. **A473**, 31-38 (2011).

[58] F. Karsch and E. Laermann, *Quark-Gluon Plasma 3*, Hwa and Wang, ed. (2003).

[59] T. Matsui and H. Saltz, Phys. Lett. **B178**, 416 (1986).

[60] J. Adams et al, Phys. Rev. **C72**, 014904 (2005).

[61] L. P. Csernai and D. Rohrich, Phys. Lett. **B458**, 454 (1999).

[62] H. Sorge, Phys. Rev. Lett. **82** 2048 (1999).

[63] J. Y. Ollitrault, Phys. Rev. **D46**, 229 (1992).

[64] W. Scheid, J. Hofmann and W. Greiner, *Proceedings, Lbl-3675*, 1-50 (1974).

[65] H. Stocker, J. A. Maruhn and W. Greiner, Z. Phys. **A290**, 297 (1979).

[66] J. Hofmann, H. Stocker, U. W. Heinz, W. Scheid and W. Greiner, Phys. Rev. Lett. **36**, 88 (1976).

[67] H. Stocker and W. Greiner, Phys. Rept. **137**, 277 (1986).

[68] B. Blattel et al, Phys. Rev. **C43**, 2728 (1991).

[69] C. M. Ko, G. Q. Li, J. Phys. **G22**, 1673 (1996).

[70] W. Cassing, E. L. Bratkovskaya, Phys. Rep. **308**, 65 (1999).

[71] L. D. Landau, Izv. Akad. Nauk, Ser . Fiz **17**, 51 (1953).

[72] J. D. Bjorken, Phys. Rev. **D27**, 140 (1983).

[73] P. B.Munzinger, J. Stachel, J. Wessels, N. Xu, Phys. Lett. **B344**, 43 (1995).

[74] P. B. Munzinger, J. Stachel, J. P. Wessels, N. Xu, Phys. Lett. **B365**, 1 (1996).

[75] D. H. Rischke, Nucl. Phys. **A610**, 88c (1996).

[76] C. M. Hung, E. Shuryak, Phys. Rev. **C57**, 1891 (1998).

[77] H. Sorge, Phys. Rev. Lett. **78**, 2309 (1997).

[78] E. M. Lifshitz and L. D. Landau, *Fluid Mechanics*, Pergamon Press (1959).

[79] H. Sorge, Phys. Rev. Lett. **78**, (12) : 2309-2312 (1997).

[80] A. Bialas, Phys. Lett. **B**, 442 : 449452 (1998).

[81] F. Wang, Nucl. Phys. **A**, 774 : 129139 (2006).

[82] Z. W. Lin and C. M. Ko, Phys. Rev. Lett. **89**, 202302 (2002).

[83] J. Cleymans, H. B. Geyer, and F. G. Scholtz, *Hadrons in Dense Matter and Hadrosynthesis*, Vol. 516 page 21 (1999).

[84] J. Y. Ollitrault, Phys. Rev. **D46**, 229 (1992).

[85] S. A. Voloshin, A. M. Poskanzer and R. Snellings, *Relativistic Heavy Ion Physics*, Vol. 1/23, Springer-Verlag (2010).

[86] U. W. Heinz, arXiv : 0901.4355 [nucl-th].

[87] P. Huovinen and P. V. Ruuskanen, Ann. Rev. Nucl. Part. Sci. **56**, 163 (2006).

[88] D. A. Teaney, arXiv : 0905.2433 [nucl-th].

[89] S. A. Voloshin and Y. Zhang, Phys. **C70**, 665 (1996).

[90] P. Sorensen, arXiv : 0905.0174 [nucl-ex].

[91] S. A. Voloshin, A. M. Poskanzer, and R. Snellings, arXiv : 0809.2949 [nucl-ex].

[92] P. F. Kolb, J. Sollfrank and U. W. Heinz, Phys. Rev. **C62**, 054909 (2000).

[93] D. H. Rischke, Y. Pursun, J. A. Maruhn, H. Stocker and W. Greiner, Heavy Ion Phys. **1**, 309 (1995).

[94] M. Bleicher and J. Aichelin, Phys. Lett. **B612**, 201 (2005).

[95] S. Soff, S. A. Bass, M. Bleicher, H. Stocker and W. Greiner, arXiv : nucl - th/0101047v1 22 Jan 2001.

[96] C. M. Hung and E. V. Shuryak, Phys. Rev. Lett. **75**.

[97] D. H. Rischke, Nucl. Phys. **A610**, 88C (1996).

[98] H. Heiselberg and A. M. Levy, Phys. Rev. **C59**, 2716 (1999).

[99] J. Brachmann et al., Phys. Rev. **C61**, 024909 (2000).

[100] J. Brachmann, A. Dumitru, H. Stocker and W. Greiner, Eur. Phys. J. **A8**, 549 (2000).

[101] B. Zhang, M. Gyulassy and C. M. Ko, Phys. Lett. **B455**, 45 (1999).

[102] M. Bleicher and H. Stocker, Phys. Lett. **B526**, 309 (2002).

[103] H. Appelshauser et al, Phys. Rev. Lett. **80**, 4136 (1998).

[104] P. F. Kolb, U. W. Heinz, In Hwa, R.C. (ed.) et al.: *Quark gluon plasma* 634-714.

[105] P. Huovinen, P. Petreczky, Nucl. Phys. **A837**, 26-53 (2010).

[106] M. Luzum, P. Romatschke, Phys. Rev. **C78**, 034915 (2008).

[107] D. Teaney, Phys. Rev. **C68**, 034913 (2003).

[108] P. Kovtun, D. T. Son, A. O. Starinets, Phys. Rev. Lett. **94**, 111601 (2005).

[109] L. P. Csernai, J. .I. Kapusta, L. D. McLerran, Phys. Rev. Lett. **97**, 152303 (2006).

[110] R. A. Lacey, N. N. Ajitanand, J. M. Alexander et al., Phys. Rev. Lett. **98**, 092301 (2007).

[111] T. Hirano, U. W. Heinz, D. Kharzeev et al, J. Phys. **G34**, S879-882 (2007).

[112] STAR collaboration, Centrality dependence of charged hadron and strange hadron elliptic flow from $\sqrt{s_{NN}}$ = 200 GeV Au + Au collisions, Phys. Rev. **C77**, 054901 (2008).

[113] STAR Collaboration, Azimuthal Anisotropy and Correlations in the Hard Scattering Regime at RHIC, Phys. Rev. Lett. **90(3)** 032301 (2003).

[114] R. Snellings, A. Poskanzer, and S. Voloshin, arXiv : 9904003 (1999).

[115] M. Gyulassy, I. Vitev, X.-N.Wang, and P. Huovinen, Phys. Lett. **B526**, 301-308 (2002).

[116] P. Huovinen, P. F. Kolb, U. Heinz, P. V. Ruuskanen, and S. A. Voloshin, Phys. Lett. **B503**, 58-64 (2001).

[117] STAR Collaboration, Multistrange Baryon Elliptic Flow in Au+Au Collisions at $\sqrt{s_{NN}} = 200$ GeV, Phys. Rev. Lett. **95**, 122301 (2005).

[118] R. S. Bhalerao and J. Y. Ollitrault, Phys. Lett. **B641**, 260-264 (2006).

[119] N. Borghini, P. M. Dinh, and J.Y. Ollitrault, arXiv : 111402 [hep-ph] (2001).

[120] X. N. Wang, Phys. Rev. **C63**, 054902 (2001).

[121] J. P. Blaizot, Nucl. Phys. **A698**, 360-371 (2002).

[122] V. Greco, C. M. Ko, and P. L'evai, Phys. Rev. Lett. **90**, 202302 (2003).

[123] R. J. Fries, B. Muller, C. Nonaka, and S. A. Bass, Phys. Rev. Lett. **90**, 202303 (2003).

[124] S. A. Voloshin, Nuclear Physics **A715**, 379c-388c (2003).

[125] ALICE collaboration, Elliptic Flow of Charged Particles in Pb-Pb Collisions at 2.76 TeV, Phys. Rev. Lett. **105**, 252302 (2010).

[126] M. B. Tsang et al, Phys. Lett. **B148**, 265-269 (1984).

[127] C. B. Chitwood et al, Phys. Rev. **C34**, 858-871 (1986).

[128] H. H. Gutbrod et al, Phys. Lett. **B216**, 267-271 (1989).

[129] X. l. Zhu, M. Bleicher and H. Stoecker, Phys. Rev. **C72**, 064911 (2005).

[130] A. M. Poskanzer and S. A. Voloshin, Phys. Rev. **C58**, 1671 (1998).

[131] J. Barrette et al, Phys. Rev. **C56**, 3254 (1997).

[132] C. Adler et al, Phys. Rev. **C66**, 034904 (2002).

[133] I. Selyuzhenkov and S. Voloshin, Phys. Rev. **C77**, 034904 (2008).

[134] B. I. Abelev et al, Phys. Rev. **C77**, 054901 (2008).

[135] N. Borghini and J. Y. Ollitrault, Phys. Rev. **C70**, 064905 (2004).

[136] J. Adams et al, Nucl. Phys. **A757**, 102 (2005).

[137] K. Adcox et al, Nucl. Phys. **A757**, 184 (2005).

[138] C. Adler et al, Phys. Rev. Lett. **87**, 182301 (2001).

[139] J. Adams et al, Phys. Rev. Lett. **92**, 052302 (2004).

[140] J. Adams et al, Phys. Rev. Lett. **95**, 122301 (2005).

[141] A. Shor, Phys. Rev. Lett. **54**, 1122 (1985).

[142] H. van Hecke, H. Sorge, and N. Xu, Phys. Rev. Lett. **81**, 5764 (1998).

[143] S. A. Bass, A. Dumitru, M. Bleicher, L. Bravina, E. Zabrodin, H. Stocker, and W. Greiner, Phys. Rev. **C60**, 021902(R) (1999).

[144] A. Dumitru, S. A. Bass, M. Bleicher, H. Stocker, and W. Greiner, Phys. Lett. **B460**, 411 (1999).

[145] S. A. Bass and A. Dumitru, Phys. Rev. **C61**, 064909 (2000).

[146] Y. Cheng, F. Liu, Z. Liu, K. Schweda, and N. Xu, Phys. Rev. **C68**, 034910 (2003).

[147] S. F. Biagi et al, Nucl. Phys. **B186**, 1 (1981).

[148] R. A. Muller, Phys. Lett. **B38**, 123 (1972).

[149] B. I. Abelev et al, Phys. Rev. Lett. **99**, 112301 (2007).

[150] S. Afanasiev et al, Phys. Rev. Lett. **99**, 052301 (2007).

[151] D. Molnar and S. A. Voloshin, Phys. Rev. Lett. **91**, 092301 (2003).

[152] C. Adler et al, Phys. Rev. Lett. **89**, 132301 (2002).

[153] C. Adler et al, Phys. Rev. Lett. **90**, 032301 (2003).

[154] S. S. Adler et al, (PHENIX Collaboration), ibid **91**, 182301 (2003).

[155] S. Esumi, Nucl. Phys. **A715**, 599C (2003).

[156] K. H. Ackermann et al, Phys. Rev. Lett. **86**, 402 (2001).

[157] P. Kolb, J. Sollfrank, and U. Heinz, Phys. Lett. **B459**, 667 (1999).

[158] D. Teaney and E. V. Shuryak, Phys. Rev. Lett. **83**, 4951 (1999).

[159] T. D. Lee, Nucl. Phys. **A750**, 1 (2005).

[160] S. A. Voloshin and A. M. Poskanzer, Phys. Lett. **B474**, 27 (2000).

[161] H. J. Drescher, A. Dumitru, C. Gombeaud, and J. Y. Ollitrault, Phys. Rev. **C76**, 024905 (2007).

[162] CbmRoot, http://cbmroot.gsi.de 875 (2006).

[163] S. Eidelman et al, Phys. Lett. **B592**, 1 (2004).

[164] L. Massacrier, Nucl. Phys. **A00**, 1 (2012).